V

Very-Long-Period Seismicity at Active Volcanoes: Source Mechanisms

Gregory P. Waite
Department of Geological and Mining Engineering and Sciences, Michigan Technological University, Houghton, MI, USA

Synonyms

Very low-frequency seismicity; VLP events; VLPs

Introduction

Deformation at active volcanoes spans a wide range of frequencies, from permanent changes up to cycles of 100s of Hz. Scattering and anelasticity attenuate the high-frequency signals rapidly, making their detection difficult. The dominant range of frequencies observed with seismological methods, between about 0.5 and 5 Hz, has been well recorded for many decades, beginning with analog recordings. Studies of discrete events and longer-duration tremor in this so-called long-period (LP) band have led to significant advances in understanding of volcanological processes, but studies of events with lower frequencies have only been possible since the use of instruments that can record them has become widespread.

Very-long-period (VLP) seismicity with frequencies below the LP band has been observed at nearly every type of active volcano, including those with activity limited to hydrothermal systems. As with LP seismicity, VLP seismicity includes both discrete events and tremor. Because VLP events involve source mechanisms that are different from those of earthquakes that occur along tectonic faults, they are referred to as VLP events, rather than VLP earthquakes. Studies of VLP events have only been possible since permanent and temporary networks of broadband seismic recording stations at active volcanoes began in the 1990s. In this comparatively short amount of time, detailed investigations of VLP events have led to great advances in understanding of the geometries of shallow magma conduits, how magma moves through these systems, and how magma and magmatic gases interact with host rocks. These interactions are manifested as deformations, which result in elastic wave propagation. When these processes have timescales of 10s of seconds to minutes, VLP seismicity can result. Because of their lower frequency nature, VLP seismicity typically represents somewhat different fluid processes than those responsible for LP events. This entry describes the observations and principal models for VLP events. It begins with a brief discussion of the instrumentation used to record VLP seismicity, with a

M. Beer et al. (eds.), *Encyclopedia of Earthquake Engineering*,
DOI 10.1007/978-3-642-35344-4

particular emphasis on the limitations and complications that can arise. A summary of VLP observations leads to a detailed section on modeling and interpretation.

Instrumentation

Observations of VLP events require broadband seismometers installed in quiet locations. The use of active force feedback technology in sensors allows for recordings at low frequencies without requiring an unreasonably large mass (▶ Principles of Broadband Seismometry). Broadband sensors in use on volcanoes have a flat response to a wide range of periods, or frequencies, typically from about 120 to 0.02 s period (0.0083–50 Hz), although the lower limit on many of these sensors is a 60 or 30 s period. These narrower band sensors are sometimes called intermediate band rather than broadband sensors. This distinction is important, as the band of the instruments used limits observations of VLP events. The lower bound of the VLP band varies therefore, depending on the capability of the recording systems.

Below the low-frequency corner of the broadband seismometer, the response typically falls off at 40 dB per decade, but strong signals with frequencies below the corner can be recovered. However, at these lower frequencies, the signals are more likely to include both ground rotation (tilt) and translation. The horizontal components of broadband seismometers are sensitive to tilt through changes in gravitational acceleration (Rodgers 1968). In fact, the broadband signal is more susceptible to tilt with increasing period so that tilt dominates translation at periods below the sensor corner if the seismometer experiences substantial rotation. Because VLP recordings are typically made in the near field, the influence of tilt at frequencies below the corner cannot be ignored. Because tilt does not affect the vertical component to a measurable degree, it can be used to help discriminate between translational and rotational motion. Recent studies have taken advantage of the tilt response to incorporate it into modeling of VLP band volcanic signals (Chouet and Dawson 2013; Maeda et al. 2011).

The tilt-dominated signals at frequencies below the instrument corner are in what is known as the ultra-long-period or ULP band (Johnson et al. 2009). Because of the importance of the instrument on the nature of the signal (i.e., rotation versus translation), the period that separates the VLP band from the ULP band might best be defined as the low corner of the seismometer used in the recording of the signals and therefore might vary from 30 to 120 s.

At the upper end of the VLP band from about 8 to 3 s period, the ubiquitous oceanic microseismic signal typically dominates. This signal, which is primarily due to interactions between ocean waves and the near-shore ocean floor, is observed everywhere on Earth but is particularly strong at ocean islands. Therefore the upper end of the observable VLP band is, in most cases, about 8 s.

Observations of VLP Seismicity

Unlike LP events, which typically have a long-duration, narrow-band coda of 10s of seconds that includes dozens of cycles, VLP events most often include only one cycle. Notable exceptions include events recorded at Mt. Erebus (Aster et al. 2008; Rowe et al. 1998) and Kilauea (Chouet and Dawson 2013; Chouet et al. 2010). VLP event locations are difficult to determine with respect to higher-frequency events, as discussed below. Where they have been determined, depths are usually within 1 km of the surface.

Although less common, VLP seismicity can also be found in the form of long-duration tremor. As with volcanic tremor in the LP band, VLP tremor signals may last for many minutes to days. Changes in tremor amplitude have been correlated with changes in surface activity (Kaneshima et al. 1996).

While some VLP seismicity can be clearly seen on broadband recordings, the amplitudes are typically much lower than those of any associated higher-frequency signal, including the

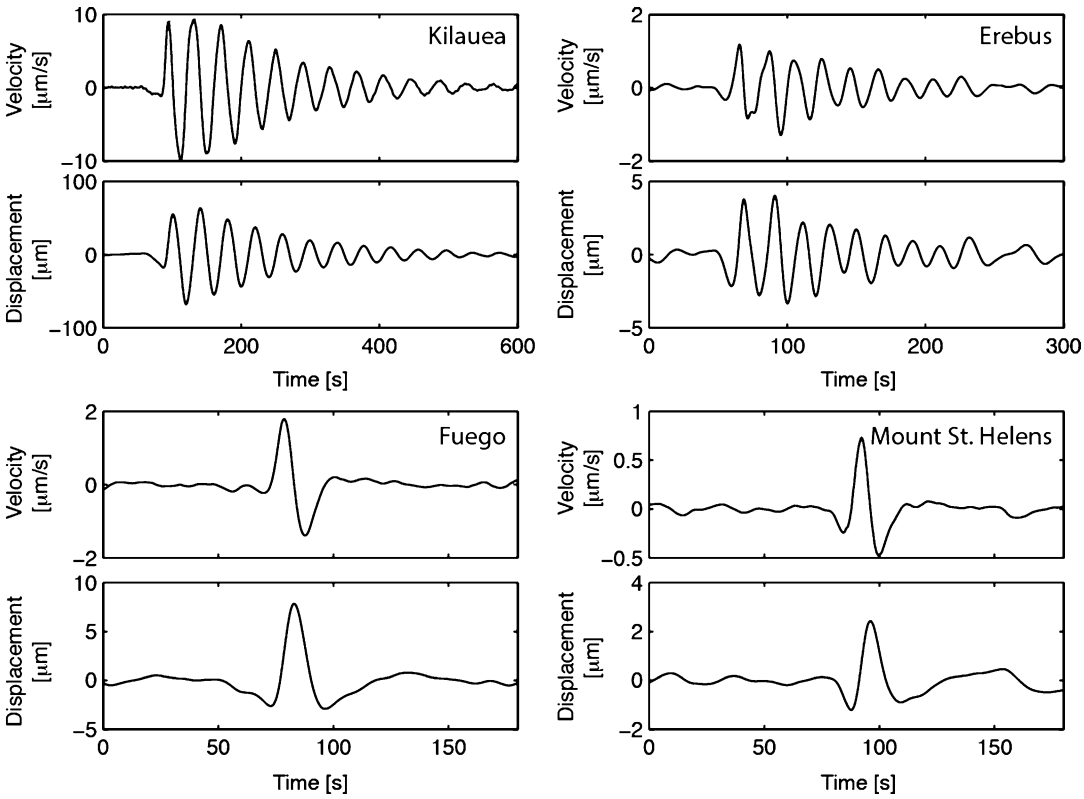

Very-Long-Period Seismicity at Active Volcanoes: Source Mechanisms, Fig. 1 Example VLP waveforms from four volcanoes with well-studied VLP seismicity. All data were band-pass filtered between 60 and 12 s period, except Erebus which was filtered from 30 to 15 s period

ocean microseism, so seismograms must be filtered before the VLPs are visible. Figure 1 shows examples of VLP events from four different volcanoes.

VLP events may be associated with phreatic eruptions (Kawakatsu et al. 2000), strombolian eruptions (Chouet et al. 2008), vulcanian eruptions (Chouet et al. 2005), passive effusion (Waite et al. 2008), or without any surface expression at all (Hill et al. 2002).

VLP events have been observed at volcanoes ranging from low-viscosity, low-silica systems such as Stromboli and Kilauea to intermediate composition systems such as Augustine and Popocatépetl and to more viscous, silica-rich systems, such as Mount St. Helens. Chouet and Matoza (2013) have compiled a list of studies published since 1992, to which the reader is referred for a comprehensive review.

Modeling

For typical earthquakes, the most basic type of information determined includes the time of occurrence, the location, and the size of the event. VLP events do not lend themselves to simple location and magnitude determinations, so other techniques have been developed. The key challenge involves the uncertainty in the first arrival time. Because VLP events do not have a clear, impulsive onset, the uncertainty in choosing the onset of the event may be many seconds. Since seismic waves propagate on the order of several km per second, this translates into an unacceptably large uncertainty in the location and time of the origin. Furthermore, the magnitudes determined for typical tectonic earthquakes are based on the assumption that seismicity is generated by shear on a near-planar fault.

In the case of volcanic VLP events, this is almost certainly never the case.

Fortunately, because of the low frequency of VLP events, the wavelengths are 10s to 100s of km, which simplifies the modeling of wave field propagation. The waveforms are not distorted by shallow heterogeneities between the source and recording station, although topography does have an important affect (Neuberg and Pointer 2000).

Particle Motion Methods

The simplest techniques for modeling the source location of VLP events use the mapped particle motions. Assuming that most of the motion is in the radial-vertical plane, seismic recordings made on stations surrounding the surface projection of a VLP source can be used to identify that point. This first-order approach can also be used to estimate the VLP event depth but is complicated by surface topography that can significantly distort the particle motion.

A method based on the assumption of radial particle motions, called radial semblance, involves solving for the model that minimizes particle motion out of the radial-vertical plane (Kawakatsu et al. 2000). The method requires that the seismic velocity of the medium is known, but the choice of velocity does not greatly affect the location. A more important potential problem with the method is that it assumes an isotropic source. Because VLP recordings are typically made in the near field, they can have significant components of motion out of the radial plane for source geometries such as dikes or sills.

Full-Waveform Modeling

Most studies of VLPs in recent years have employed full-waveform modeling, as long as enough seismic stations are available to constrain the source mechanism. In these studies, a point source is typically chosen, and the wave field is modeled using a finite-difference approximation approach. For VLP events, the long wavelengths simplify the modeling in two important ways. First, the structural model used for the wave field modeling can be fairly simple. Variations in the elastic parameters of rocks on the order of km can be ignored for stations within a few km of the source and wavelengths of 10s to 100s of km. This means the velocity-density structure can be assumed to be homogeneous. Choosing the wrong velocity will introduce some error in the source location but will not significantly alter the source mechanism.

The second way in which modeling of VLP data is simplified by the long wavelengths is that source finiteness can be ignored. In studies where the wavelength is on the order of the size of the source, for example, for a 100-m-long section of the conduit, the source dimensions affect the predicted waveforms at stations in the near field. However, the wavelength of VLP events is orders of magnitude larger than the source dimension, meaning a point source approximation is appropriate.

Moment Tensor Inversion

Waveform modeling approaches rely on source representation theory; that is, that there exists a set of equivalent forces that can represent those that caused the event ("▶ Long-Period Moment-Tensor Inversion: The Global CMT Project", and "▶ Non-Double-Couple Earthquakes"). In modeling of tectonic earthquakes, the representative forces can be described by the symmetric second-order moment tensor, which has six independent components (Fig. 2). The components of the moment tensor are nine force couples, which represent either dipole or shear couples. A purely isotropic source would involve volume change, but not shear, and could be represented by a tensor with nonzero values for the dipole components on the diagonal and a nonzero trace. The off-diagonal terms describe torque and are nonzero when there is shear. Tectonic earthquakes, which involve slip on a near-planar fault, can adequately be described with shear and no volume change (the trace of the tensor is zero as in Fig. 3). On the other hand, VLP events may involve volume changes and no shear. Figure 4 provides an example of a source commonly found in VLP inversions, that of a tensile crack, with a nonzero trace.

Advective net mass transfer gives rise to single forces in addition to the moment components. Single forces are insignificant in tectonic

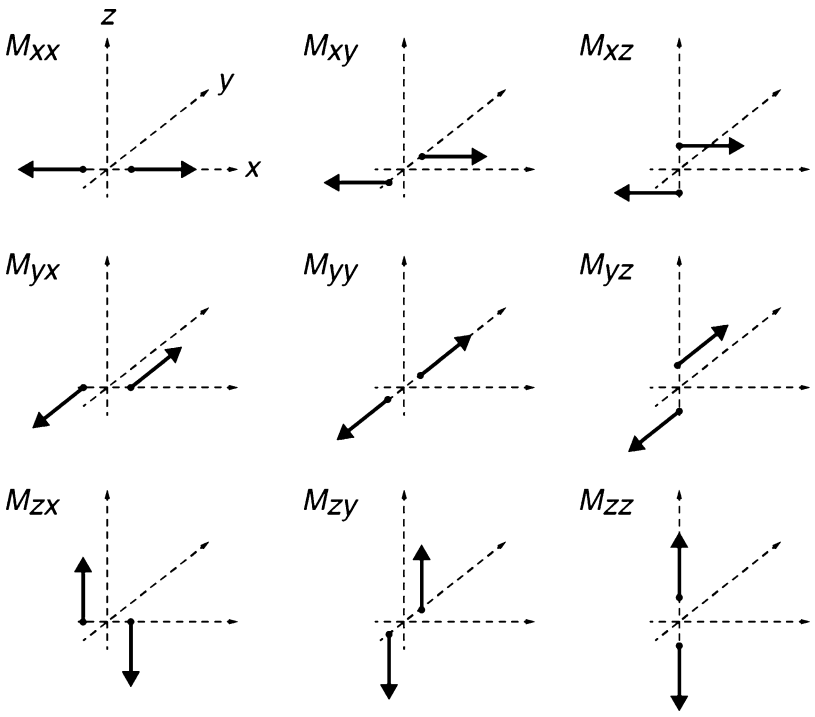

Very-Long-Period Seismicity at Active Volcanoes: Source Mechanisms, Fig. 2 Force couples representing the full moment tensor. Dipole components are on the diagonal. The off-diagonal components represent shearing force couples

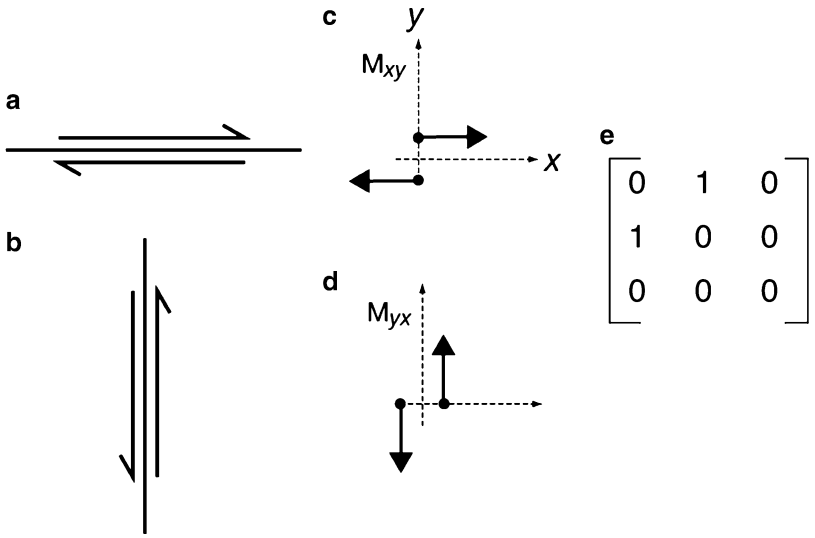

Very-Long-Period Seismicity at Active Volcanoes: Source Mechanisms, Fig. 3 Example of force couples representative of slip on a fault. For simplicity, the third dimension is not shown. For x and y in the horizontal plane, this would represent a vertical strike-slip fault. Right-lateral slip on the fault normal to the y direction, represented by (**a**), or left-lateral slip on the fault normal to the x direction, represented by (**b**), would both be represented by the pair of force couples shown in (**c**) and (**d**), which is why this is called a double-couple solution. The dimensionless symmetric moment tensor for this set of force couples is also shown in (**e**)

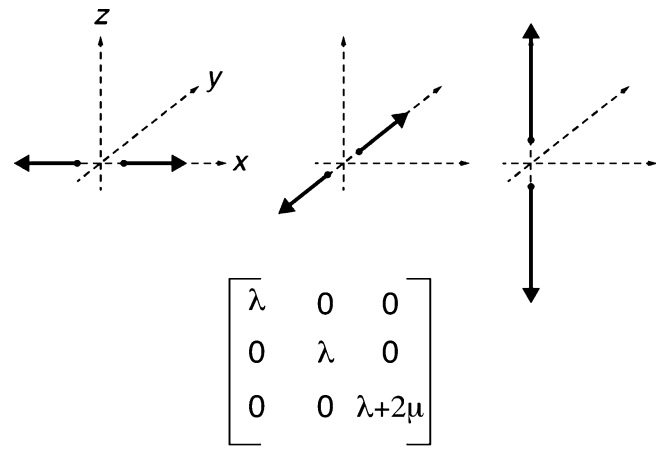

Very-Long-Period Seismicity at Active Volcanoes: Source Mechanisms,
Fig. 4 Example of force couples representative of opening of a tensile crack lying in the *x*-*y* plane and opening in the *z* direction. Note that this can be represented with positive dipole components

earthquake modeling but may become important for VLP events associated with eruption or transfer of a large mass of material. Large landslides and glacier movements can also produce signals that are well modeled with single force solutions. In these cases, as the mass accelerates along the surface of the Earth, the response is a single force in the direction opposite the motion of the mass movement. Later, when the mass begins to slow, the reaction force is parallel to the direction of the slide. Similarly, the reaction force to a volcanic eruption is opposite the direction of motion of the erupted mass. Single forces can arise within the Earth as well. If the center of mass of a magma volume accelerates, the force can be observed seismically as long as there is a means for it to couple to the solid earth. Specific models are addressed below.

In order to model the source mechanism, Green functions that describe the response at one location (the station) to an impulse at another (the source) are computed. The displacement field $u_n\left(\vec{r},t\right)$, generated by a source, may be written as:

$$u_n\left(\vec{r},t\right) = F_p(t) * G_{np}\left(\vec{r},t\right) + M_{pq}(t) * G_{np,q}\left(\vec{r},t\right), \quad p,q = x,y,z, \tag{1}$$

where $u_n\left(\vec{r},t\right)$ is the n-component of the displacement at time t and receiver position $\vec{r}$, $F_p(t)$ is the time history of the force applied in the p-direction, $M_{pq}(t)$ is the time history of the pq-component of the moment tensor, and $G_{np}\left(\vec{r},t\right)$ is the tensor of Green functions that relates the n-component of displacement at the receiver position, $\vec{r}$, with the p-component of impulsive force at the source position. Although it is not specified in Eq. 1, $G_{np}\left(\vec{r},t\right)$ depends on the source position as well. The q notation indicates spatial differentiation with respect to the q-coordinate, and the symbol * denotes convolution. Summation over repeated indices is implied.

With the matrix of Green functions, **G**, the linear inverse problem, $\mathbf{d} = \mathbf{Gm}$, is solved where **d** is the data vector and **m** is the model vector, which consists of moment tensor components and single forces. Each model parameter has a time history. In the most general case, the inversion is allowed to vary freely so that a new model vector is computed for each corresponding time in the data vector. An analogous approach is to compute the inversions in the frequency domain, so that one frequency at a time is solved for each moment component. Other approaches to solving the inverse problem have also been used.

Because the number of model and data parameters involved in the inversions is small, the process is computationally inexpensive. This approach does not require that the ratio of the moment components is constant throughout the source time history, but in most cases the resulting ratios are stable for most of the source time history of the event.

Although the inversion can be constrained in various ways, for example, to force the trace of

the tensor to be zero in the case of tectonic earthquakes, unconstrained inversions for VLP sources are preferred. VLP source inversions are typically dominated by the isotropic components, suggesting volume changes in conduits as the primary source of deformation. Single forces are included in inversions to account for advection-related forces. By repeating the inversion over a large volume of points (Green functions) in a grid, the preferred source centroid location is chosen as that with the lowest misfit to the data.

Typical VLP Source Models

The time history of the moment tensor and single forces representing the VLP source must be interpreted in terms of a physical model. Although the modeling assumes a point source, which represents the centroid location of moment and force, the characteristics of the moment and force components have implications for the orientation of the source components. If the ratios of the moment components are stable for the duration of the event, the eigenvectors and eigenvalues (principal components) can easily be obtained and compared with simplified geometries. Assuming the host rock surrounding the source can be represented with as a homogeneous elastic material with elastic Lamé parameters λ and μ and the volume change is ΔV, a tensile crack can be represented with dipole components having magnitudes equal to $\Delta V\lambda$ for the in-plane components and $\Delta V(\lambda + 2\ \mu)$ for the component that is normal to the crack plane. For igneous rocks, possibly at high temperatures given their proximity to magmatic fluids, values of λ and μ may vary over several orders of magnitude. The ratio between them, however, is limited; λ ranges from 1 to 2 times μ. The ratios of the eigenvalues of a tension crack are then between 1:1:2 and 1:1:3. For a pipe, the dipole components are $\Delta V\lambda$ for the component parallel to the pipe and $\Delta V(\lambda + \mu)$ for those perpendicular to it leading to ratios of 1:2:2 to 2:3:3. For a purely spherical source volume change, the components are equal.

In some cases the moment tensor looks very much like one of these end member physical models. In these cases, the source can be interpreted as volume change related to inflation and/or deflation of a portion of the conduit. In other cases, the interpretation is not straightforward but may involve a combination of sources. For example, for magma flowing from a sill into a dike, one would expect the total moment to be close to the combined volume decrease in the sill $-\Delta V\lambda[1{:}1{:}(1{+}2\ \mu/\lambda)]$ and increase in the dike, which might be $\Delta V\lambda[1{:}(1{+}2\ \mu/\lambda){:}1]$.

Single forces arise from net mass advection. Acceleration of the center of mass of a fluid will produce a reaction force in the Earth. The nature of the reaction force is related to the coupling, which can be separated into shearing and normal forces. Shearing forces along the conduit walls in a direction antiparallel to the flow direction couple as frictional forces. The efficiency of this mechanism is strongly related to the magma fluid viscosity. Normal forces couple to conduit geometrical features where there is a change in the shape or orientation of the conduit. Numerical and analog laboratory experiments demonstrate the efficacy of the coupling of single forces through this mechanism. A change in conduit geometry, for example, from a sill to a dike as above, can provide a location for the coupling of pressure changes resulting from mass movements to occur. It is important to recognize that steady flow, without acceleration, will not produce observable single forces.

VLP Events and Magma Type

VLP events have been identified and modeled at volcanoes with nearly all magma types. Styles of VLP event tend to be related to the fluid viscosity, which depends on magma composition and temperature. In general, low-silica magmas, such as basalts, have low viscosity, and high-silica magmas, such as rhyolite, have higher viscosity. In addition to the temperature, the presence of dissolved volatiles and the crystal content influence viscosity as well. Because of the importance of viscosity on interpreting the source mechanisms, the description of types of VLP sources is organized by fluid type.

VLP Events at Low-Viscosity Volcanoes

The nature of eruptions at low-viscosity volcanoes is linked to the movement of exsolved gas. Because gas bubbles can ascend buoyantly through the higher-density magma relatively easily, eruptions tend to be less explosive than at volcanoes with magmas that are capable of trapping bubbles under higher pressures. Typical eruptions include bursting of bubbles at the top of the magma column, although more explosive eruptions are possible.

Bubbles grow through diffusion of volatiles out of solution and through coalescence of smaller bubbles. Bubbles also grow as they ascend due to the lower magma pressures at shallow depths. Under favorable conditions bubbles can grow to a diameter as large as the conduit, and if the gas volume is large enough, the bubble will occupy an elongated region within the conduit. As this gas slug ascends, magma must descend around it through a relatively thin film. An abrupt acceleration of the center of mass occurs where the conduit changes shape, either by changing diameter or orientation. VLP seismicity can result from these accelerations, which produce the equivalent of single forces and moments.

A well-studied laboratory analog model involves the ascent of a gas slug in a cylindrical conduit that has an abrupt change from a smaller to larger diameter (James et al. 2006). The slug accelerates slowly as it ascends through the lower portion of the conduit due to the gradual decrease in pressure of the overlying fluid. When the slug enters the upper portion of the conduit, it expands and accelerates rapidly. The mass of the gas is low so that the acceleration of the slug does not impart a significant force, but the acceleration of the gas requires a downward acceleration of the fluid. The fluid is massive enough to produce an observable force which couples to the conduit at the point where it enlarges and, to a lesser degree, through the frictional forces along the conduit wall. This model provides context for interpreting VLP events in low-viscosity magmas where gas slug ascent is common.

VLP events from Mount Erebus, Etna, Kilauea, and Stromboli are among the best-studied examples from low-viscosity volcanoes. In each case, the migrations of gas slugs have been interpreted as the source of at least some of the VLP events. In most cases the VLP events are temporally linked to explosive eruptions. At Stromboli, for example, moment tensor inversions point to the inflation and deflation of crack-like portions of the conduit to accommodate the movement of gas slugs that lead to strombolian-style eruptions (Chouet et al. 2008). VLP events associated with eruptions for separate, closely spaced vents have distinct waveform characteristics, and the source mechanisms are consistent with changes in the conduit geometry leading to each of the vents.

At Kilauea, there are also multiple styles of VLP events, all of which are associated with differential motions of gas and magma. Again, the best coupling of the forces within the magma to the solid conduit occurs at places in the conduit where the geometry changes. One feature that emerges from the modeling is the transition from a near-horizontal crack to a pipe that leads to the surface (Chouet et al. 2010). This corner is at a depth of about 1 km below the surface, about two or three times deeper than the main VLP source centroid at Stromboli. At Erebus, similar types of eruptions are associated with the ascent of a gas slug from a position 400 hundred meters below and a several hundred meters to the northwest of the active lava lake (Aster et al. 2008).

VLP Events at High-Viscosity Volcanoes

In contrast to VLP seismicity at low-viscosity volcanoes, which tend to be associated with small-scale strombolian explosions, at higher-viscosity systems, VLP events are most commonly associated with more explosive vulcanian-style eruptions. These higher-viscosity volcanoes are typically andesitic and dacitic in composition, but less silicic magmas can have high viscosities in the shallow subsurface if their crystal content is high. These larger

eruptions may eject significant masses of rock, meaning the vertical reaction force is the dominant component of the VLP source mechanism (Ohminato et al. 2006).

In other cases, the source mechanisms of VLP events associated with vulcanian-style eruptions are dominated by crack-like mechanisms associated with changes in conduit geometry or shallow (1–2 km) magma reservoirs (Chouet et al. 2005). Inflation or deflation mechanisms are not likely to involve gas slugs in these cases, since the magmas are too viscous to allow slug ascent. Instead, deflation may follow the explosion and be related to the eruption of material from the conduit. Reinflation of the conduit can be the result of a combination of the influx of new magma and pressurization associated with rapid gas exsolution (Nishimura 2004).

VLP events in silicic systems may also be associated with the passive extrusion of magma, as in the case of Mount St. Helens (Waite et al. 2008). The VLP events were the result of unsteady flow as the magma moved from a vertical to horizontal portion of the conduit just below the surface. The mechanism included inflation and deflation of cracks and also nearly horizontal single forces. The single forces were associated with acceleration and deceleration of magma as it moved through this portion of the conduit.

VLP Events at Hydrothermal Systems

Hydrothermal cracks, filled with water, steam, or a combination of nonmagmatic fluids, may also be the source of VLP events. Unsteady flow of pressurized hydrothermal fluids through cracks (Nakamichi et al. 2009; Ohminato 2006) can produce VLP events that are very similar to those produced in magmatic systems. The low viscosity of water and steam relative to magma inhibits measureable flow-related frictional single forces, so mechanisms tend to be dominated by volume changes in cracks. At Aso volcano, nearly continuous VLP tremor is attributed to resonance in a horizontal crack (Kaneshima et al. 1996).

Long-Duration VLPs and VLP Tremor

VLP events tend to have short duration with respect to the period, having only one or two cycles. However, VLP events may have long durations indicative of a resonant source mechanism (Chouet et al. 2010; Kumagai et al. 2003; Rowe et al. 1998). Nearly continuous VLP tremor, with intermittent higher amplitudes, was recorded at Usu, but unlike Kilauea and Erebus, this signal was not associated with any observable surface activity (Yamamoto et al. 2002). In these low-viscosity systems, the ringing of the signal may be attributed to the oscillations of pressure waves, which are induced by the initial mass advection-related mechanism. At Usu, it was most likely related to unsteady flow of magma through a constricted portion of the conduit. Although VLP tremor is uncommon, it can be useful for constraining the extent of magma conduit components, as resonant properties of the signal depend on both the fluid and host rock properties and the size and shape of the resonator.

Relationship Between VLP Events and Gas Emissions

At Erebus, Kilauea, and Stromboli, VLP events are temporally linked to visual observations of explosions; the correlation is consistent with models for the VLP that involve ascent of a gas slug through the conduit to the surface. In a few cases, VLP events have been recorded coincident with high-resolution gas emission measurements. These cases provide a means for quantitative estimates of the relationship between outgassing and VLP events. At Asama (Kazahaya et al. 2011) and for certain types of VLP events at Fuego (Waite et al. 2013), the VLP event amplitudes correlate with the mass of SO_2 measured for each discrete gas emission (Fig. 5). The correlation is less clear at Etna but is present under certain conditions (Zuccarello et al. 2013). These correlations demonstrate the influence of unsteady gas flow on deformation in the shallow conduit. They can be used to infer the role of gases for VLP events even when quantitative measurements are not available.

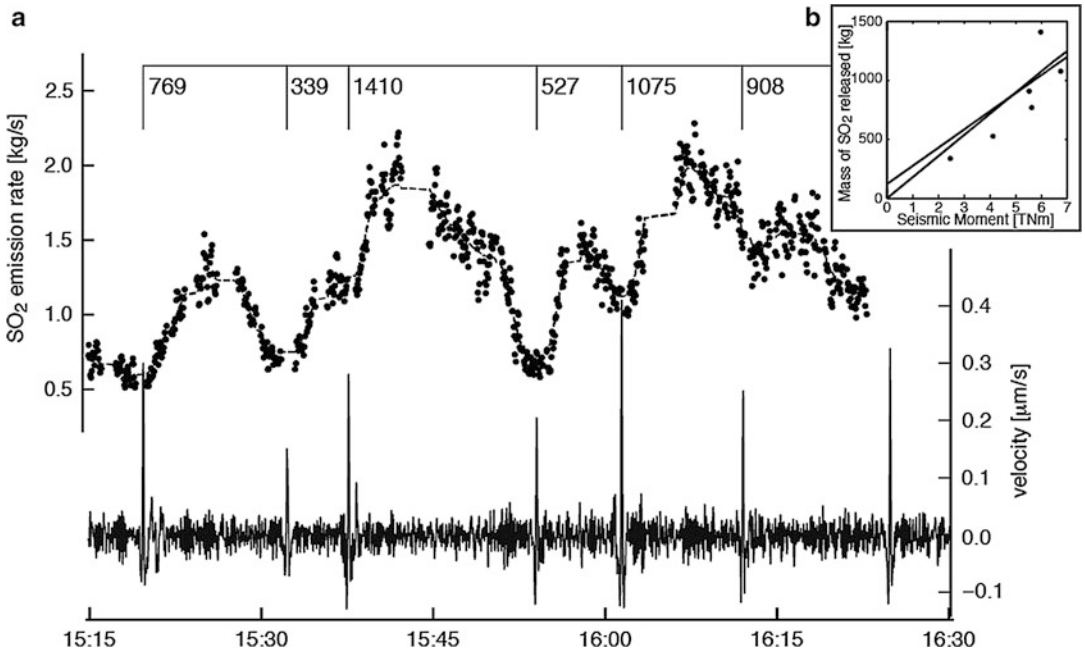

Very-Long-Period Seismicity at Active Volcanoes: Source Mechanisms, Fig. 5 (**a**) Temporal correlation between VLP events (*solid line*) and SO_2 emission rate (*dots*) plotted for about 90 min on 15 January 2008 from Fuego. Masses computed for each of the six events are listed above the SO_2 data. The *dashed line* is a weighted 50-point moving average of the SO_2 emission data. The linear regressions of SO_2 mass against seismic moment (**b**) show a positive correlation.

Summary

Very-long-period seismicity is usually the result of fluid transport processes in magmatic or hydrothermal systems. VLP events are most often related to inflation and deflation of elements of a conduit system, such as dikes, sills, and pipes; they tend to be dominated by isotropic elements of the moment tensor. Forces associated with mass advection can give rise to single force source components which are not found in models for typical earthquake sources. VLP events have been found in nearly every type of volcano yet they are not ubiquitous. If fluid flow is steady, there will not be large pressure fluctuations necessary to cause VLP seismicity. While their existence has only been known since the early 1990s, interpretations of VLP events have led to a far greater understanding of geometry and dynamics of fluids in shallow magmatic and hydrothermal systems.

References

Aster R, Zandomeneghi D, Mah S, McNamara S, Henderson DB, Knox H, Jones K (2008) Moment tensor inversion of very long period seismic signals from Strombolian eruptions of Erebus Volcano. J Volcanol Geotherm Res 177(3):635–647. doi:10.1016/j.jvolgeores.2008.08.013

Chouet B, Dawson P (2013) Very long period conduit oscillations induced by rockfalls at Kilauea Volcano, Hawaii. J Geophys Res Solid Earth 118(10):5352–5371. doi:10.1002/jgrb.50376

Chouet BA, Matoza RS (2013) A multi-decadal view of seismic methods for detecting precursors of magma movement and eruption. J Volcanol Geotherm Res 252:108–175. doi:10.1016/j.jvolgeores.2012.11.013

Chouet B, Dawson P, Arciniega-Ceballos A (2005) Source mechanism of Vulcanian degassing at Popocatépetl Volcano, Mexico, determined from waveform inversions of very long period signals. J Geophys Res 110:B07301. doi:10.1029/2004JB003524

Chouet B, Dawson P, Martini M (2008) Shallow-conduit dynamics at Stromboli Volcano, Italy, imaged from waveform inversions. Geol Soc Lond Spec Publ 307(1):57–84. doi:10.1144/SP307.5

Chouet BA, Dawson PB, James MR, Lane SJ (2010) Seismic source mechanism of degassing bursts at Kilauea Volcano, Hawaii: results from waveform inversion in the 10–50 s band. J Geophys Res 115(B9). doi:10.1029/2009jb006661

Hill DP, Dawson PB, Johnston MJS, Pitt AM, Biasi GP, Smith K (2002) Very-long-period volcanic earthquakes beneath Mammoth Mountain, California. Geophys Res Lett 29(10):1370. doi:10.1029/2002GL014833

James MR, Lane SJ, Chouet BA (2006) Gas slug ascent through changes in conduit diameter: laboratory insights into a volcano-seismic source process in low-viscosity magmas. J Geophys Res 111:B05201. doi:10.1029/2005JB003718.

Johnson JB, Sanderson R, Lyons J, Escobar-Wolf R, Waite G, Lees JM (2009) Dissection of a composite volcanic earthquake at Santiaguito, Guatemala. Geophys Res Lett 36(16). doi:10.1029/2009gl039370

Kaneshima S, Kawakatsu H, Matsubayashi H, Oikawa J, Takeo M, Iidaka T, Yamasato H (1996) Mechanism of phreatic eruptions at Aso volcano inferred from near-field broadband seismic observations. Science 273(5275):642–645. doi:10.1126/science.273.5275.643

Kawakatsu H, Kaneshima S, Matsubayashi H, Ohminato T, Sudo Y, Tsutsui T, Legrand D (2000) Aso94: Aso seismic observation with broadband instruments. J Volcanol Geotherm Res 101(1–2):129–154

Kazahaya R, Mori T, Takeo M, Ohminato T, Urabe T, Maeda Y (2011) Relation between single very-long-period pulses and volcanic gas emissions at Mt. Asama, Japan. Geophys Res Lett 38:L11307. doi:10.1029/2011GL047555

Kumagai H, Miyakawa K, Negishi H, Inoue H, Obara K, Suetsugu D (2003) Magmatic dike resonances inferred from very-long-period seismic signals. Science 299(5615):2058–2061. doi:10.1126/science.1081195

Maeda Y, Takeo M, Ohminato T (2011) A waveform inversion including tilt: method and simple tests. Geophys J Int 184(2):907–918. doi:10.1111/j.1365-246X.2010.04892.x

Nakamichi H, Kumagai H, Nakano M, Okubo M, Kimata F, Ito Y, Obara K (2009) Source mechanism of a very-long-period event at Mt. Ontake, central Japan: response of a hydrothermal system to magma intrusion beneath the summit. J Volcanol Geotherm Res 187(3–4):167–177. doi:10.1016/j.jvolgeores.2009.09.006

Neuberg J, Pointer T (2000) Effects of volcano topography on seismic broad band waveforms. Geophys J Int 143(1):239–248

Nishimura T (2004) Pressure recovery in magma due to bubble growth. Geophys Res Lett 31(12):L12613. doi:10.1029/2004gl019810

Ohminato T (2006) Characteristics and source modeling of broadband seismic signals associated with the hydrothermal system at Satsuma–Iwojima volcano, Japan. J Volcanol Geotherm Res 158(3–4):467–490. doi:10.1016/j.jvolgeores.2006.08.004

Ohminato T, Takeo M, Kumagai H, Yamashima T, Oikawa J, Koyama E, Urabe T (2006) Vulcanian eruptions with dominant single force components observed during the Asama 2004 volcanic activity in Japan. Earth Planets Space 58:583–593

Rodgers PW (1968) The response of the horizontal pendulum seismometer to Rayleigh an Love waves, tilt, and free oscillations of the Earth. Bull Seism Soc Am 58:1384–1406

Rowe CA, Aster RC, Kyle RR, Schlue JW, Dibble RR (1998) Broadband recording of Strombolian explosions and associated very-long-period seismic signals on Mount Erebus volcano, Ross Island, Antarctica. Geophys Res Lett 25(13):2297–2300

Waite GP, Chouet BA, Dawson PB (2008) Eruption dynamics at Mount St. Helens imaged from broadband seismic waveforms: interaction of the shallow magmatic and hydrothermal systems. J Geophys Res 113(B2):B02305. doi:10.1029/2007jb005259

Waite GP, Lyons JJ, Nadeau PA (2013) Variability in eruption style and associated very-long-period earthquakes at Fuego volcano, Guatemala. J Geophys Res 118(4):1526–1533. doi:10.1002/jgrb.50075

Yamamoto M, Kawakatsu H, Yomogida K, Koyama J (2002) Long period (12 sec) volcanic tremor observed at Usu 2000 eruption: seismological detection of a deep magma plumbing system. Geophys Res Lett 29(9):1329. doi:10.1029/2001GL013996

Zuccarello L, Burton MR, Saccorotti G, Bean CJ, Patanè D (2013) The coupling between very long period seismic events, volcanic tremor, and degassing rates at Mount Etna volcano. J Geophys Res 118(9):4910–4921. doi:10.1002/jgrb.50363

Vibration-Based Damage Identification: The Z24 Bridge Benchmark

Edwin Reynders and Guido De Roeck
Department of Civil Engineering, KU Leuven, Leuven, Belgium

Synonyms

Ambient vibration testing; Data normalization; Progressive damage testing; Structural health monitoring; System identification

Introduction

Structural health monitoring (SHM) relies on the repeated observation of features that are each sensitive to a certain type of structural damage. Among the many possible features, dynamic characteristics, in particular natural frequencies, are often selected as they depend on the global and the local stiffness of the structure of interest as well as its boundary conditions.

Monitoring the evolution of the features over time allows, in principle, to detect structural damage. In practice, however, this needs to be applied with care because of two reasons. Firstly, many features cannot be measured directly, but they have to be estimated from measured data using system identification techniques. Modal characteristics, for instance, can be estimated from vibration response data such as accelerations or strains, but this introduces estimation errors (Reynders et al. (2008); Reynders 2012). Secondly, nearly all features are not only sensitive to structural damage but also to changes in temperature, relative humidity, wind speed, operational loading, etc. This means that both the accuracy of the estimated features and the environmental and operational influences should be accounted for.

This entry presents a case study, where a full-sized structure has been monitored for almost a year before introducing realistic damage in a controlled way. The aim of the long-term continuous monitoring test was to quantify the environmental variability of the bridge dynamics, while the aim of the subsequent short-term progressive damage test was to investigate experimentally whether realistic damage has a measurable influence on the bridge's dynamic behavior. The combination of a long-term continuous monitoring test with realistic short-term progressive damage tests resulted in a unique data set that has aided many researchers in benchmarking new methods for system identification, operational modal analysis, damage identification, and structural health monitoring (Maeck and De Roeck 2003; Reynders and De Roeck 2009). In the next sections, the bridge and the performed tests are first described in more detail. Subsequently, the identified modal characteristics are presented as well as their evolution during the monitoring period. Finally, results on structural health monitoring and damage identification are presented.

Description of the Structure and the Dynamic Tests

The Z24 bridge was located in the canton Bern near Solothurn, Switzerland. It was part of the road connection between the villages of Koppigen and Utzenstorf, overpassing the A1 highway between Bern and Zürich. It was a classical post-tensioned concrete two-cell box-girder bridge with a main span of 30 m and two side spans of 14 m (Fig. 1). The bridge was built as a freestanding frame with the approaches backfilled later. Both abutments consisted of triple concrete columns connected with concrete hinges to the girder. Both intermediate supports were concrete piers clamped into the girder. An extension of the bridge girder at the approaches provided a sliding slab. All supports were rotated with respect to the longitudinal axis, which yielded a skew bridge. The bridge, which dated from 1963, was demolished at the end of 1998, because a new railway adjacent to the highway required a new bridge with a larger side span.

To monitor the bridge dynamics over a 1-year time span, 16 accelerations were measured on the bridge at different points and in different directions. Every hour, a sequence of 65,536 acceleration samples, taken at the 16 sensors, was collected and stored to a hard disk after compression. The construction works at the new bridge that replaced the Z24 caused damage to one accelerometer. Although the type of accelerometer was specially designed for long-term use, some showed a considerable drift and a few of them failed during operation. Since the aim of the long-term monitoring test was to quantify the environmental variability of the bridge dynamics, all environmental variables that were considered of possible importance for the bridge dynamics have been monitored. Sensors to measure air temperature, air humidity, rain true or false, wind speed, and wind direction were installed at

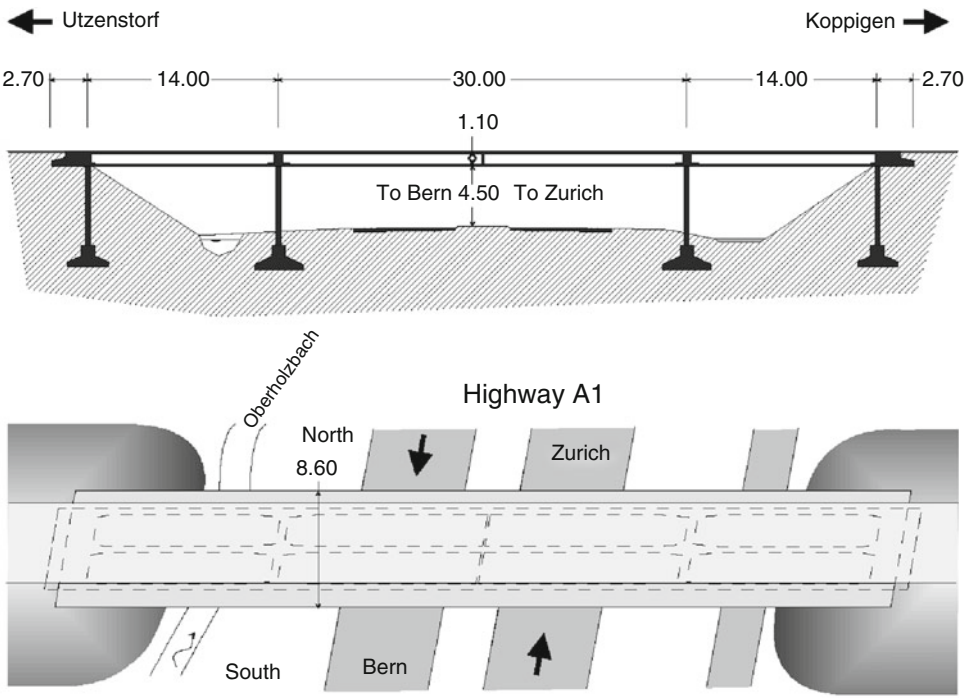

Vibration-Based Damage Identification: The Z24 Bridge Benchmark, Fig. 1 Front view (*top*) and top view (*bottom*) of the Z24 bridge (Reproduced with permission from: J. Maeck and G. De Roeck. Description of Z24 benchmark. *Mechanical Systems and Signal Processing*, 17(1):127–131, 2003)

the bridge, resulting in five sensors for the atmospheric conditions. A sensor consisting of two inductive loops was installed to detect the presence of vehicles on the bridge. Since temperature was known to have a key influence on the dynamics of civil engineering structures, the bridge's thermal state was monitored in detail. At the middle of the three spans, the temperature was measured at eight positions on the girder. The girder was a continuous beam with the intermediate piers clamped into it, and therefore the angular deflection of the girder at these piers and the elongation of the middle span were also measured. The soil temperature near each of the concrete columns at the approaches was monitored, as well as that near the north, central, and south parts of the intermediate piers (12 sensors in total). Finally, the temperature of the pavement was also measured at the middle of the three spans, since the drilling of the access holes for the installation of the temperature sensors on the girder revealed that the asphalt cover had a thickness of 16–18 cm instead of the 5 cm as indicated on the blueprints.

In order for the subsequent progressive damage tests to be significant, it was made sure that they were relevant for the safety of the bridge and that the simulated damage occurred frequently, a condition that was checked in the literature and by questioning Swiss bridge owners. Since the A1 highway was never closed to traffic, some damage scenarios that meet these criteria could not be applied without reducing the safety of the traffic, which was considered of paramount importance. The traffic on the Z24 bridge was diverted to the A36 highway. Table 1 gives a complete overview of all progressive damage tests that were performed. Some of them are illustrated in Fig. 2. Before and after each applied damage scenario, the bridge was subjected to a forced and an ambient operational vibration test. With a measurement grid consisting of a regular 3×45 grid on top of the bridge deck and a 2×8 grid on each of the two pillars,

291 degrees of freedom have been measured: all displacements on the pillars and mainly vertical and lateral displacements on the bridge deck. Because the number of degrees of freedom to be measured exceeded the number of available accelerometers and acquisition channels, the data were collected in nine setups using five reference channels. The forced excitation was applied by two vertical shakers, placed on the bridge deck. A 1-kN shaker was placed on the middle span and a 0.5-kN shaker was placed at the Koppigen side span. The shaker input signals were generated using an inverse fast Fourier transform (FFT) algorithm, resulting in a fairly flat force spectrum between 3 and 30 Hz. After scenario 8, a drop weight test was also performed, using a device that allowed to drop a mass of up to 120 kg from a height of up to 1 m in a controlled way (Reynders et al. 2010). The applied shaker and drop weight forces were periodic with eight periods. A total of 65,536 samples were collected at a sampling rate of 100 Hz, using an antialiasing filter with a 30-Hz cutoff frequency.

Vibration-Based Damage Identification: The Z24 Bridge Benchmark, Table 1 Chronological overview of applied damage scenarios, indicating on which date a specific scenario was fully realized (Reproduced with permission from: E. Reynders, G. Wursten, and G. De Roeck. Output-only structural health monitoring in changing environmental conditions by means of nonlinear system identification. *Structural Health Monitoring*, 13(1):82–93, 2014)

Date (1998)	Scenario
4 August	Undamaged condition
9 August	Installation of pier settlement system
10 August	Lowering of pier, 20 mm
12 August	Lowering of pier, 40 mm
17 August	Lowering of pier, 80 mm
18 August	Lowering of pier, 95 mm
19 August	Lifting of pier, tilt of foundation
20 August	New reference condition
25 August	Spalling of concrete at soffit, 12 m^2
26 August	Spalling of concrete at soffit, 24 m^2
27 August	Landslide of 1 m at abutment
31 August	Failure of concrete hinge
2 September	Failure of 2 anchor heads
3 September	Failure of 4 anchor heads
7 September	Rupture of 2 out of 16 tendons
8 September	Rupture of 4 out of 16 tendons
9 September	Rupture of 6 out of 16 tendons

Identification of Modal Characteristics

The ambient, shaker, and drop weight data from scenario 8 of the progressive damage test have been employed as benchmark data for system identification methods for operational modal analysis. Peeters and Ventura (2003) compare the modal parameter estimates obtained by seven different research teams in the framework of this benchmark. In addition, new modal parameter estimation techniques have been validated on the benchmark data. The best reported result was obtained by applying a subspace identification algorithm (Reynders and De Roeck 2008) and a maximum likelihood algorithm

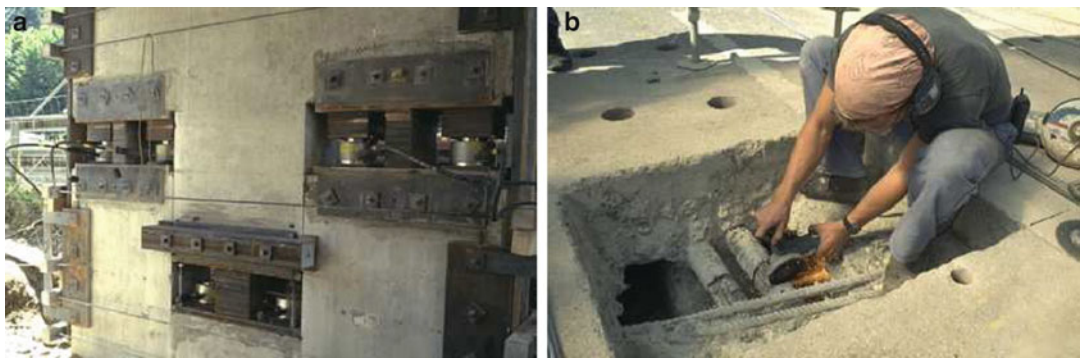

Vibration-Based Damage Identification: The Z24 Bridge Benchmark, Fig. 2 Settlement system used for damage scenarios 3–6 (**a**) and cutting of tendons for scenarios 15–17 (**b**)

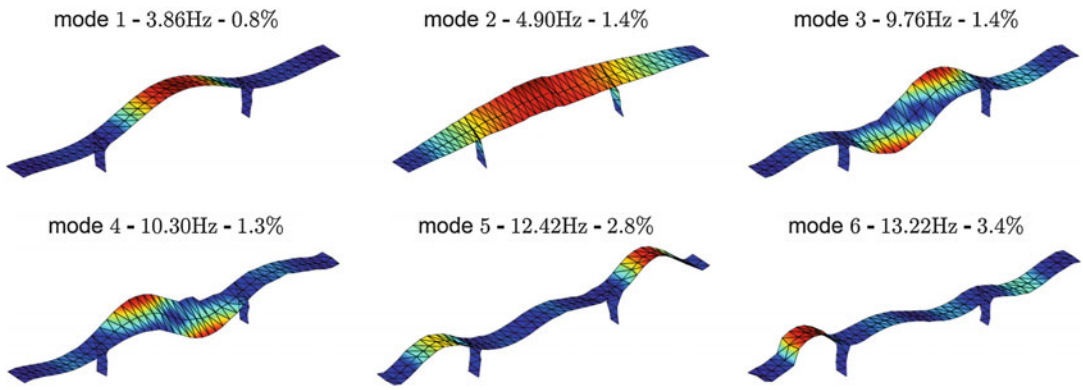

Vibration-Based Damage Identification: The Z24 Bridge Benchmark, Fig. 3 Natural frequencies, damping ratios, and mode shapes of the Z24 for damage scenario 8, identified with reference-based stochastic subspace identification (Reproduced with permission from: E. Reynders et al. Fully automated (operational) modal analysis, Mechanical Systems and Signal Processing, 29:228–250, 2012)

(Parloo, Guillaume, and Cauberghe 2003) to the shaker data. In this way, 10 modes could be determined.

From the ambient vibration data, 6 modes can be determined with good quality (see Fig. 3). These modes are also predominantly present in the long-term monitoring data. Modes 1, 5, and 6 are vertical bending modes, while mode 2 is a lateral mode. Modes 3 and 4 are modes that show combined bending and torsion, which is caused by the skewness of the pillars with respect to the bridge deck. They have close natural frequencies and their mode shapes look similar, but in fact they show a low degree of correlation.

Peeters and De Roeck (2001) also identified the modal characteristics of the first four modes (see Fig. 3) for each of the 5,652 sets of hourly acceleration data, recorded during the continuous monitoring test. For these data, detailed mode shapes are not available due to the small number of accelerometers employed during the monitoring period. The evolution of the natural frequencies over time is plotted in Fig. 4. It can be noted in this figure that the monitoring system failed (was not active) during short periods of time.

Of all environmental variables that had been recorded, the temperature was found to have the largest influence on the modal characteristics. A plot of the natural frequencies as a static function of the temperature of the surface asphalt layer (Fig. 4) reveals the high influence of the temperature on the bridge dynamics, as well as its nonlinear nature. The most probable explanation lies in the large temperature dependency of the Young's modulus of the asphalt layer (Peeters and De Roeck 2001).

Structural Health Monitoring by Natural Frequency Tracking

As was observed in Fig. 4, the natural frequency variations due to regular environmental and operational variability may mask the influence of even severe damage completely. Therefore, when performing damage detection by monitoring natural frequencies, it is necessary to filter out the regular environmental variability.

This can be achieved by system identification. In this approach, a mathematical model that describes the relationship between regular environmental variations and variations in natural frequencies is fitted to training data that have been collected on the undamaged structure. Afterwards, in the monitoring phase, the mathematical model is employed for predicting the natural frequencies. When the differences between these predicted values and the observed ones grow large, the structure behaves differently as during the training phase. These differences are then most probably caused by damage,

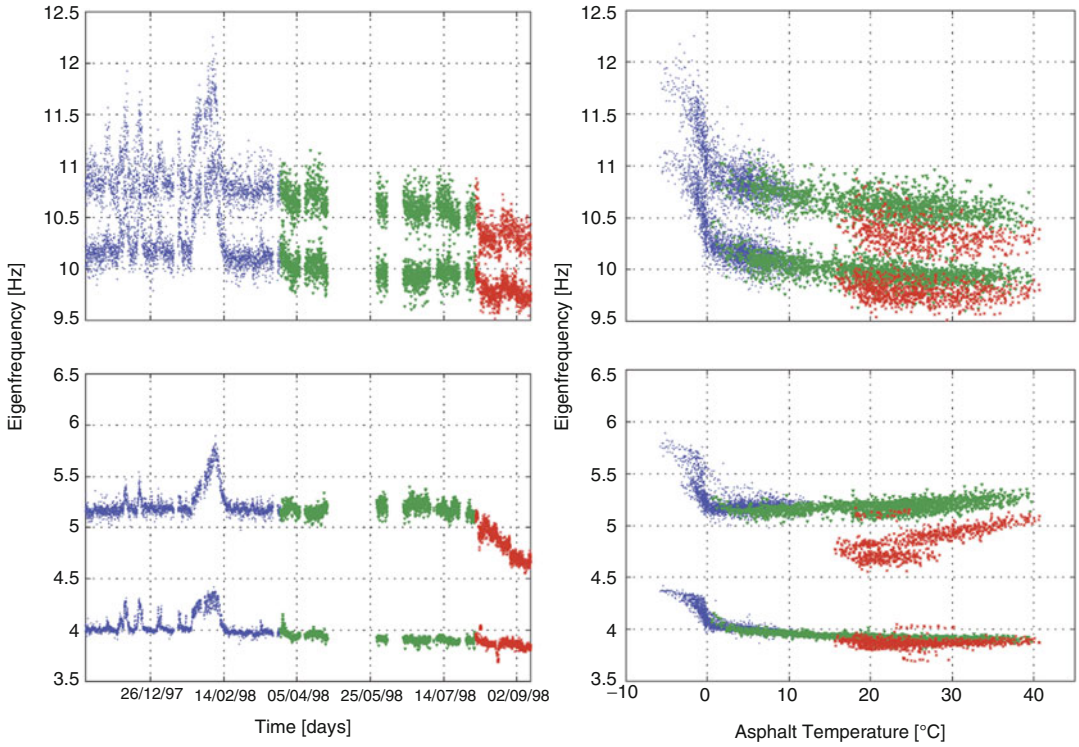

Vibration-Based Damage Identification: The Z24 Bridge Benchmark, Fig. 4 Natural frequencies of the Z24 bridge: evolution as a function of time (*left*) and as a function of the temperature of the asphalt layer. *Blue dots*, training data (3,000 training samples); *green triangles*, monitoring data in undamaged condition; *red crosses*, monitoring data in damaged condition (Reproduced with permission from: E. Reynders, G. Wursten, and G. De Roeck. Output-only structural health monitoring in changing environmental conditions by means of nonlinear system identification. *Structural Health Monitoring*, 13(1):82–93, 2014)

because the regular environmental variations are accounted for by the model.

Several system identification techniques have been proposed in this context (Xia et al. 2012). One of the most promising approaches is based on improved kernel principal component analysis or kPCA (Reynders et al. 2014). This approach has the advantages of (1) identifying a very general nonlinear model in a computationally cheap and robust way and (2) being output only, i.e., not requiring the measurement of the environmental and operational quantities that cause the regular variations in the modal characteristics. Figure 5 illustrates that kPCA can effectively predict the onset of damage (installation of the pier settlement system, see Table 1) by natural frequency monitoring. The predictions are better when more training data samples are used, because in this way, the nonlinear model covers a larger portion of the regular environmental and operational variations of the natural frequencies. Alternative approaches that do need the environmental data as inputs also perform well on the present data set (see, e.g., Spiridonakos and Chatzi 2014), since a large amount of environmental variables was measured.

Damage Localization and Quantification

Modal characteristics cannot only be used for monitoring and damage detection but also for damage localization and quantification. The progressive damage test data from the Z24 bridge have served as benchmark data in this context, and Reynders and De Roeck (2009) present a

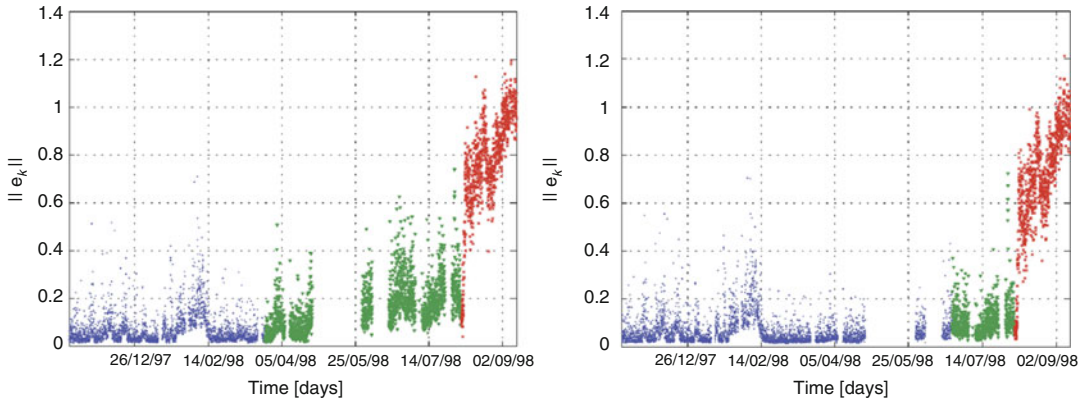

Vibration-Based Damage Identification: The Z24 Bridge Benchmark, Fig. 5 Evolution of the misfit of a nonlinear output-only model that predicts the evolution of the first four natural frequencies of the Z24 bridge. *Left*: misfit of a model trained with 3,000 data samples. *Right*: misfit of a model trained with 4,000 data samples. *Blue dots*, training data; *green triangles*, monitoring data in undamaged condition; *red crosses*, monitoring data in damaged condition (Reproduced with permission from: E. Reynders, G. Wursten, and G. De Roeck. Output-only structural health monitoring in changing environmental conditions by means of nonlinear system identification. *Structural Health Monitoring*, 13(1):82–93, 2014)

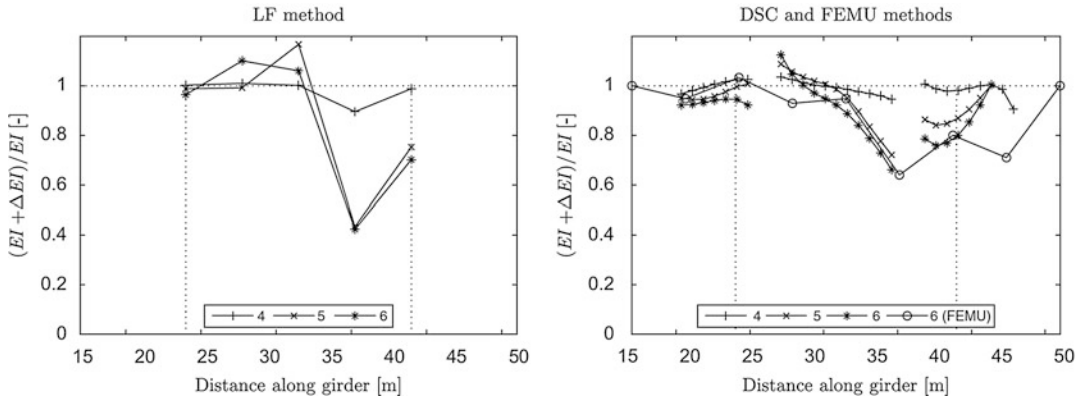

Vibration-Based Damage Identification: The Z24 Bridge Benchmark, Fig. 6 Relative difference in bending stiffness of the Z24 bridge deck between damage scenarios 4–6 and damage scenario 2. *Left*, local flexibility (LF) method; *right*, direct stiffness calculation (DSC) and finite element model updating (FEMU) (Reproduced with permission from: E. Reynders and G. De Roeck. A local flexibility method for vibration-based damage localization and quantification. *Journal of Sound and Vibration*, 329(12):2367–2383, 2010)

literature review of the benchmark results reported up to 2009.

Two major approaches for damage localization and quantification can be discriminated: model based and non-model based, also called parametric and nonparametric, respectively. Parametric methods are based on a (finite element) model of the structure, some parameters of which are adjusted using vibration measurements, by minimizing the difference between the modal characteristics computed with the model and the ones that are identified from measurements. Nonparametric methods do not need a detailed model of the structure, but most of them are based on ad hoc damage indicators with a rather limited range of application; exceptions are the damage-locating vector method of Bernal (2002) and the local flexibility method of Reynders and De Roeck (2010).

For the Z24 bridge, the linear bending and torsion stiffness of the bridge deck have been most often employed for damage localization and quantification. The pier settlement of the bridge (damage scenarios 3–6 from Table 1) is the damage case that has the largest influence on these quantities. Figure 6 shows the estimated ratio between the bending stiffness in damaged and undamaged condition, as obtained from three different damage identification methods: one non-parametric (Reynders and De Roeck 2010) and two parametric methods (Maeck et al. 2001; Teughels and De Roeck 2004). All three methods yield qualitatively similar results: a large reduction in bending stiffness around the settled pier, which is in agreement with observed crack patterns in the bridge deck. Quantitative differences are probably related to the fact that the three methods use different assumptions and strategies to aggregate the local damage over a certain zone of the structure.

Summary

Structural health monitoring (SHM) relies on the repeated observation of features that are each sensitive to a certain type of structural damage. Among the many possible features, dynamic characteristics, in particular natural frequencies, are often selected as they depend on the global and the local stiffness of the structure of interest as well as its boundary conditions. This entry presents a case study, where a full-sized structure has been monitored for almost a year before introducing realistic damage in a controlled way. The combination of a long-term continuous monitoring test with realistic short-term progressive damage tests resulted in a unique data set that has aided many researchers in benchmarking new methods for system identification, operational modal analysis, damage identification, and structural health monitoring. The bridge and the performed tests are first described in detail. Subsequently, the identified modal characteristics are presented along with their evolution during the monitoring period. Finally, recent results on structural health monitoring and damage identification, obtained with the Z24 data, are presented.

Cross-References

- ▶ Advances in Online Structural Identification
- ▶ Ambient Vibration Testing of Cultural Heritage Structures
- ▶ Operational Modal Analysis in Civil Engineering: An Overview
- ▶ Post-Earthquake Diagnosis of Partially Instrumented Building Structures
- ▶ Seismic Behavior of Ancient Monuments: From Collapse Observation to Permanent Monitoring
- ▶ Stochastic Structural Identification from Vibrational and Environmental Data
- ▶ System and Damage Identification of Civil Structures

References

Bernal D (2002) Load vectors for damage localization. ASCE J Eng Mech 128(1):7–14

Maeck J, De Roeck G (2003) Description of Z24 benchmark. Mech Syst Signal Process 17(1):127–131

Maeck J, Peeters B, De Roeck G (2001) Damage identification on the Z24-bridge using vibration monitoring. Smart Mater Struct 10(3):512–517

Parloo E, Guillaume P, Cauberghe B (2003) Maximum likelihood identification of non-stationary operational data. J Sound Vib 268(5):971–991

Peeters B, De Roeck G (2001) One-year monitoring of the Z24-bridge: environmental effects versus damage events. Earthq Eng Struct Dyn 30(2):149–171

Peeters B, Ventura C (2003) Comparative study of modal analysis techniques for bridge dynamic characteristics. Mech Syst Signal Process 17(5):965–988

Reynders E (2012) System identification methods for (operational) modal analysis: review and comparison. Arch Comput Meth Eng 19(1):51–124

Reynders E, De Roeck G (2008) Reference-based combined deterministic-stochastic subspace identification for experimental and operational modal analysis. Mech Syst Signal Process 22(3):617–637

Reynders E, De Roeck G (2009) Continuous vibration monitoring and progressive damage testing on the Z24 bridge. In: Boller C, Chang FK, Fujino Y (eds) Encyclopedia of structural health monitoring. Wiley, New York, pp 2149–2158

Reynders E, De Roeck G (2010) A local flexibility method for vibration-based damage localization and quantification. J Sound Vib 329(12):2367–2383

Reynders E, Pintelon R, De Roeck G (2008) Uncertainty bounds on modal parameters obtained from Stochastic Subspace Identification. Mech Syst Signal Process 22(4):948–969

Reynders E, Degrauwe D, De Roeck G, Magalhaes F, Caetano E (2010) Combined experimental-operational modal testing of footbridges. ASCE J Eng Mech 136(6):687–696

Reynders E, Wursten G, De Roeck G (2014) Output-only structural health monitoring in changing environmental conditions by means of nonlinear system identification. Structural Health Monitoring 13(1):82–93

Spiridonakos M, Chatzi E (2014) Polynomial chaos expansion models for SHM under environmental variability. In: Cunha Á, Caetano E, Ribeiro P, Müller G (eds) Proceedings of the 9th international conference on structural dynamics, EURODYN 2014, Porto, pp 2393–2398, June–July 2014

Teughels A, De Roeck G (2004) Structural damage identification of the highway bridge Z24 by FE model updating. J Sound Vib 278(3):589–610

Xia Y, Chen B, Weng S, Ni Y-Q, Xu Y-L (2012) Temperature effect on vibration properties of civil structures: a literature review and case studies. J Civ Struct Heal Monit 2(1):29–46

Vibrations of Beams for Seismic Response Estimation

Vittorio Gusella and Federico Cluni
Department of Civil and Environmental Engineering, University of Perugia, Perugia, Italy

Introduction

The last decades have seen a growing interest for design and construction of tall buildings. In order to accurately estimate the dynamic response to environmental loads of such complex constructions, structural models are usually characterized by a large number of degrees of freedom; as a consequence, structural optimization algorithms, used to reduce the cost and the energy required to construct such buildings while maintaining appropriate safety levels, might be time consuming and even not feasible given the large dimension of the problem. As far as the global response is concerned, it is of interest to develop reduced models that are capable of giving approximate optimal solutions by significantly reducing the computation time. Therefore, a reduced model based on a Timoshenko beam will be presented in this paper which can be used to estimate the response of tall buildings subjected to environmental loads, such those induced by earthquakes.

Flexural Beam Models

In the present section, the main beam models are recalled, focusing mainly on the Timoshenko model, which is able to describe the flexural behavior of the beam taking into account, besides the flexural stiffness and inertia due to deflections, also the shear deformability and the rotational inertia. Nevertheless, before introducing the Timoshenko beam model, the two models that can considered to be the ones on which it is based, the Euler-Bernoulli and the simple shear models, will be briefly recalled.

The Cartesian reference system consists of the principal axes of the section, x and y, and the axis of the beam (the line where centroids of the sections lie), z. The beam is loaded with a distributed load q(z), acting in the direction y, and a distributed moment m(z) whose axis is in x direction (see Fig. 1). The analysis is limited to the plane y-z, and the only displacements of interest are those in y direction, the deflection v(z). In the following, since the dependence on z is obvious, it will be dropped.

In what follows, the balance equations, which relate the loads q and m to the bending moment M and shear force V, will be used:

$$\frac{dM}{dz} = V - m \tag{1}$$

$$\frac{dV}{dz} = -q \tag{2}$$

The Euler-Bernoulli Beam

It is assumed that the deflection of the beam is due to the moment only, and therefore this behavior is known as "pure bending." The constitutive equation which relate the bending moment M to the slope of deflection curve is

$$M = EI\frac{d\theta}{dz} \quad \text{with} \quad \theta = -\frac{dv}{dz} \tag{3}$$

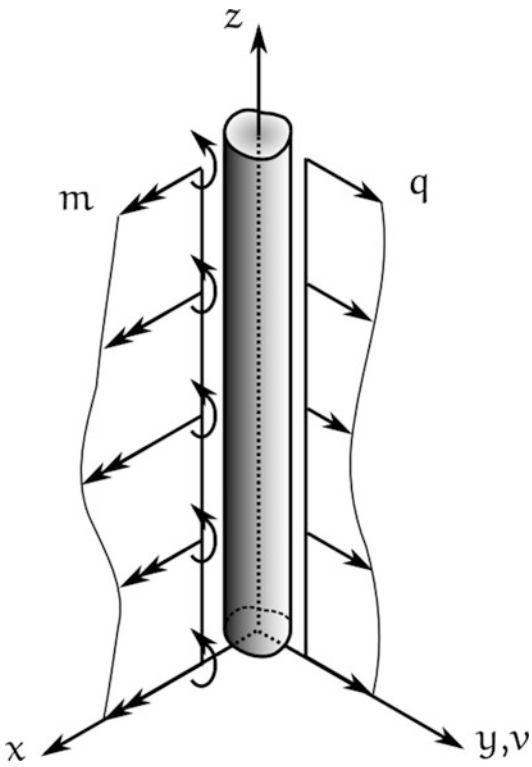

Vibrations of Beams for Seismic Response Estimation, Fig. 1 Reference system of the beam model

where EI is the bending stiffness, the product of the Elastic (Young's) modulus, E, and the second moment of area (or moment of inertia) for rotation around x, I. The previous relation takes into account the fact that the sections of the beam remain plane in the deformed configuration and normal to the axis.

Using Eqs. 3 and 1, the following equation is obtained:

$$\mathrm{EI}\frac{\mathrm{d}^2\theta}{\mathrm{dz}^2} = \mathrm{V} - \mathrm{m} \Rightarrow -\mathrm{EI}\frac{\mathrm{d}^3 v}{\mathrm{dz}^3} = \mathrm{V} - \mathrm{m}$$

Assuming $\mathrm{m} = 0$, differentiating again, and using Eq. 2, the Euler-Bernoulli equation for the beam is obtained:

$$\frac{\mathrm{d}^4 v}{\mathrm{dz}^4} = \frac{\mathrm{q}}{\mathrm{EI}}$$

Moreover, the following are also valid:

$$\mathrm{M} = -\mathrm{EI}\frac{\mathrm{d}^2 v}{\mathrm{dz}^2}$$
$$\mathrm{V} = -\mathrm{EI}\frac{\mathrm{d}^3 v}{\mathrm{dz}^3}$$

The Euler-Bernoulli model can be extended to the dynamic case using the D'Alembert principle and adding to the external load q the load equivalent to inertia forces associated with deflections, q_i:

$$\mathrm{q}_i = -\rho\mathrm{A}\frac{\partial^2 v}{\partial \mathrm{t}^2}$$

where ρ is the density of mass and A is the area of the section. Assuming ρ and A constant along the axis, the equation that rules the problem is

$$\mathrm{EI}\frac{\partial^4 v}{\partial \mathrm{z}^4} + \rho\mathrm{A}\frac{\partial^2 v}{\partial \mathrm{t}^2} = \mathrm{q}$$

The free motion equation is

$$\frac{\partial^4 v}{\partial \mathrm{z}^4} + \frac{\rho\mathrm{A}}{\mathrm{EI}}\frac{\partial^2 v}{\partial \mathrm{t}^2} = 0$$

with solution that can be written through separation of variables as

$$v(\mathrm{z},\mathrm{t}) = \tilde{v}(\mathrm{z})\cos(\omega\mathrm{t} + \phi) \tag{4}$$

where

$$\tilde{v}(\mathrm{z}) = \mathrm{D}_1\cos(\mathrm{kz}) + \mathrm{D}_2\sin(\mathrm{kz}) + \mathrm{D}_3\cosh(\mathrm{kz}) + \mathrm{D}_4\sinh(\mathrm{kz})$$

and

$$\mathrm{k} = \sqrt[4]{\frac{\omega^2\rho\mathrm{A}}{\mathrm{EI}}}$$

The parameters D_1, D_2, D_3, and D_4 can be obtained using the boundary conditions and determining ω to avoid the trivial solution. For example, in the case of cantilever beam clamped at $\mathrm{z} = 0$ and free at $\mathrm{z} = \mathrm{L}$, the following boundary conditions hold

$$v(0,t) = 0, \quad \theta(0,t) = 0, \quad M(L,t) = 0, \quad V(L,t) = 0$$

and the values of ω are given by the following

$$\cos\sqrt[4]{\frac{\omega^2 \rho A}{EI}}L \cosh\sqrt[4]{\frac{\omega^2 \rho A}{EI}}L + 1 = 0$$

which has solutions

$$\omega_j = (a_j L)^2 \frac{1}{L^2}\sqrt{\frac{EI}{\rho A}}$$

with

$$a_1 L = 1.875, \quad a_2 L = 4.694, \quad a_3 L = 7.855,$$
$$a_j L \approx a_3 L + (j-3)2\pi \quad \text{for } j = 4, 5, \ldots$$

The Simple Shear Beam

The simple shear beam model is based on the assumption that the beam undergoes only shear deformation. In this case, the constitutive equation which relates V to the slope of deflection curve is

$$V = GK\gamma \quad \text{with} \quad \gamma = \frac{dv}{dz} \tag{5}$$

where GK is the shear stiffness, the product of the tangential modulus, G, and shear area K. Moreover, the shear area is related to A by means of a *shear factor* κ, K = κA, which depends on the shape of the section and is determined by means of energetic equivalence.

Using the preceding and Eq. 2, the following equation is obtained:

$$\frac{d^2 v}{dz^2} = -\frac{q}{GK}$$

In dynamics, by means of D'Alembert principle, the following equation of motion is obtained:

$$GK\frac{\partial^2 v}{\partial z^2} - \rho A\frac{\partial^2 v}{\partial t^2} = -q$$

and in free motion

$$\frac{\partial^2 v}{\partial z^2} - \frac{\rho}{G\kappa}\frac{\partial^2 v}{\partial t^2} = 0$$

Adopting the separation of variables Eq. 4, the following expression for deflection is obtained:

$$\tilde{v}(z) = D_1 \cos(kz) + D_2 \sin(kz)$$

and

$$k = \sqrt{\frac{\omega^2 \rho}{G\kappa}}$$

The parameters D_1, D_2 can be obtained using the boundary conditions and determining ω to avoid the trivial solution. For example, in the case of cantilever beam clamped at z = 0 and free at z = L, the boundary conditions are

$$v(0,t) = 0, \quad V(L,t) = 0$$

and therefore

$$\omega_j = (2j-1)\frac{\pi}{2L}\sqrt{\frac{G\kappa}{\rho}} \quad \text{for } j = 1, 2, \ldots$$

The Timoshenko Beam Model

In the Timoshenko beam model (Timoshenko 1921, 1922), it is assumed that the slope of the deflection curve is the sum of those due to bending moment and those given by shear deformation, each one assumed to act alone

$$\frac{dv}{dz} = \gamma - \theta \tag{6}$$

The first part of both Eqs. 3 and 5 is unchanged, while the second parts are modified according to Eq. 6, and therefore

$$V = GK\gamma = GK\left(\frac{dv}{dz} + \theta\right), \quad M = EI\frac{d\theta}{dz}$$

Assuming EI and GK constant along the axis, the following equations are obtained:

$$\begin{cases} GK\left(\frac{d^2v}{dz^2}+\frac{d\theta}{dz}\right)=-q \\ EI\frac{d^2\theta}{dz^2}-GK\left(\frac{dv}{dz}+\theta\right)=-m \end{cases}$$

In dynamics the D'Alembert principle is used again. Moreover, in the Timoshenko beam model, the inertial forces associated to rotations θ are also taken into account

$$m_i=-\rho I\frac{\partial^2\theta}{\partial t^2}$$

and the equations of motion are therefore

$$\begin{cases} GK\left(\frac{\partial^2v}{\partial z^2}+\frac{\partial\theta}{\partial z}\right)-\rho A\frac{\partial^2v}{\partial t^2}=-q \\ EI\frac{\partial^2\theta}{\partial z^2}-GK\left(\frac{\partial v}{\partial z}+\theta\right)-\rho I\frac{\partial^2\theta}{\partial t^2}=-m \end{cases} \quad (7)$$

In free motion the following equations hold:

$$\begin{cases} GK\left(\frac{\partial^2v}{\partial z^2}+\frac{\partial\theta}{\partial z}\right)-\rho A\frac{\partial^2v}{\partial t^2}=0 \\ EI\frac{\partial^2\theta}{\partial z^2}-GK\left(\frac{\partial v}{\partial z}+\theta\right)-\rho I\frac{\partial^2\theta}{\partial t^2}=0 \end{cases}$$

and considering that

$$\theta=\gamma-\frac{\partial v}{\partial z}\Rightarrow\frac{\partial\theta}{\partial z}=\frac{\partial\gamma}{\partial z}-\frac{\partial^2v}{\partial z^2}=\frac{1}{GK}\frac{\partial V}{\partial z}-\frac{\partial^2v}{\partial z^2}=-\frac{\rho}{G\kappa}\frac{\partial^2v}{\partial t^2}-\frac{\partial^2v}{\partial z^2}$$

the following equation can be obtained:

$$EI\frac{\partial^4v}{\partial z^4}+\rho A\frac{\partial^2v}{\partial t^2}-\rho I\left(1+\frac{E}{G\kappa}\right)\frac{\partial^4v}{\partial z^2\partial t^2}+\frac{\rho^2I}{G\kappa}\frac{\partial^4v}{\partial t^4}=0$$

The solution is given by

$$v(z,t)=\tilde{v}(z)\cos(\omega t+\phi)$$

where

$$\tilde{v}(z)=\begin{cases} D_1\cos(k_1z)+D_2\sin(k_1z)+D_3\cos h(k_2z)+D_4\sin h(k_2z) & \omega<\omega_c \\ D_1\cos(k_1z)+D_2\sin(k_1z)+D_3\cos(k_2z)+D_4\sin(k_2z) & \omega>\omega_c \end{cases} \quad (8)$$

where ω_c is a cut-off frequency given by

$$\omega_c=\frac{G\kappa A}{\rho I}$$

As usual, ω is found by imposing the suitable boundary conditions.

It can be interesting to plot the values of ω in terms of variation of slenderness $\lambda = L/r$ where $r=\sqrt{I/A}$, as in Fig. 2 (the values have

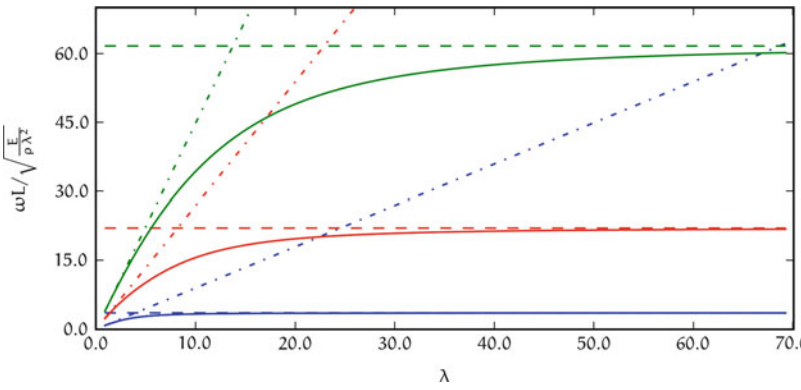

Vibrations of Beams for Seismic Response Estimation, Fig. 2 Pulsations of the first (*blue*), second (*red*), and third (*green*) mode of cantilever beam with $\kappa = 0.85$ and $E/G = 2.6$: (—) Timoshenko beam model, (— —) Euler-Bernoulli beam model, (— · —) simple shear model

been obtained assuming $\kappa = 0.85$ and $E/G = 2.6$). It can be noted that as λ increases, the values ω of the Euler-Bernoulli model are achieved

$$\frac{\omega_j L}{\sqrt{\frac{E}{\rho\lambda^2}}} = (a_j L)^2$$

while as λ decreases the values of the simple shear model are recovered

$$\frac{\omega_j L}{\sqrt{\frac{E}{\rho\lambda^2}}} = (2j-1)\frac{\pi}{2}\sqrt{\frac{G}{E}\kappa}\cdot\lambda$$

It is worth noting that the convergence to the Euler-Bernoulli or simple shear beam tends to slow down as mode number increases. For intermediate values of slenderness, the natural frequencies ω depend on both the bending stiffness EI and the shear stiffness GK.

Example The case of a cantilever beam with the following characteristics:

$A = 0.120\ \text{mm}^2$,	$I = 1.60 \cdot 10^{-3}\ \text{mm}^4$	$K = 0.102\,\text{mm}^2$
$E = 30,000\ \text{N/mm}^2$,	$G = 11,538\ \text{N/mm}^2$	
$\rho = 2,500\,\text{kg/m}^3$	$L = 2.0\,\text{m}$	$\omega_c = 542.43\ \text{rad/s}$

is considered in what follows.

The first 12 modal shapes are shown in Fig. 3, and the parameters of Eq. 8 are shown in Tables 1 and 2. In the tables also the phase velocity, defined as the ratio between the angular frequency, ω, and the wavenumber, k_1, is reported: as well known, the phase velocity is unbounded for the Euler-Bernoulli beam, while in the case of Timoshenko beam the two different families of waves present when $\omega > \omega_c$, with wavenumbers k_1 and k_2, tend to the following values (Hagedorn and DasGupta 2007):

$$\lim_{j\to+\infty}\frac{\omega_j}{k_1} = \sqrt{\frac{G\kappa}{\rho}} = 62.63\ \text{rad/s}$$

$$\lim_{j\to+\infty}\frac{\omega_j}{k_2} = \sqrt{\frac{E}{\rho}} = 109.54\ \text{rad/s}$$

where j is the mode number.

Deterministic Excitation-Response Relations

The unit impulse applied at the section $z = z_o$ at the instant $t = t_o$ is considered:

$$f(z,t) = \delta(z - z_o)\delta(t - t_o)$$

Assuming that prior of the unit impulse application the beam is at rest with zero displacement, the response can be expressed by (Robson et al. 1971; Crandal 1979; Lin 1967; Elishakoff 1988)

$$v(z,t) = h(z, t - t_o; z_o)$$

where $h(z, t - t_o; z_o)$ is the *impulse response function* or *Green's function*. A $f(z, t)$ arbitrary space-time action can be regarded as a superposition of unit impulses at the time τ in generic section $0 \le \xi \le L$

$$f(z,t) = \int_{-\infty}^{+\infty} d\tau \int_0^L f(\xi, t-\tau)\delta(z-\xi)\delta(\tau)d\xi$$

If the impulse response function is known, then the response at the time t in the generic section $0 \le \xi \le L$ can be obtained by the following convolution integral or superposition integral:

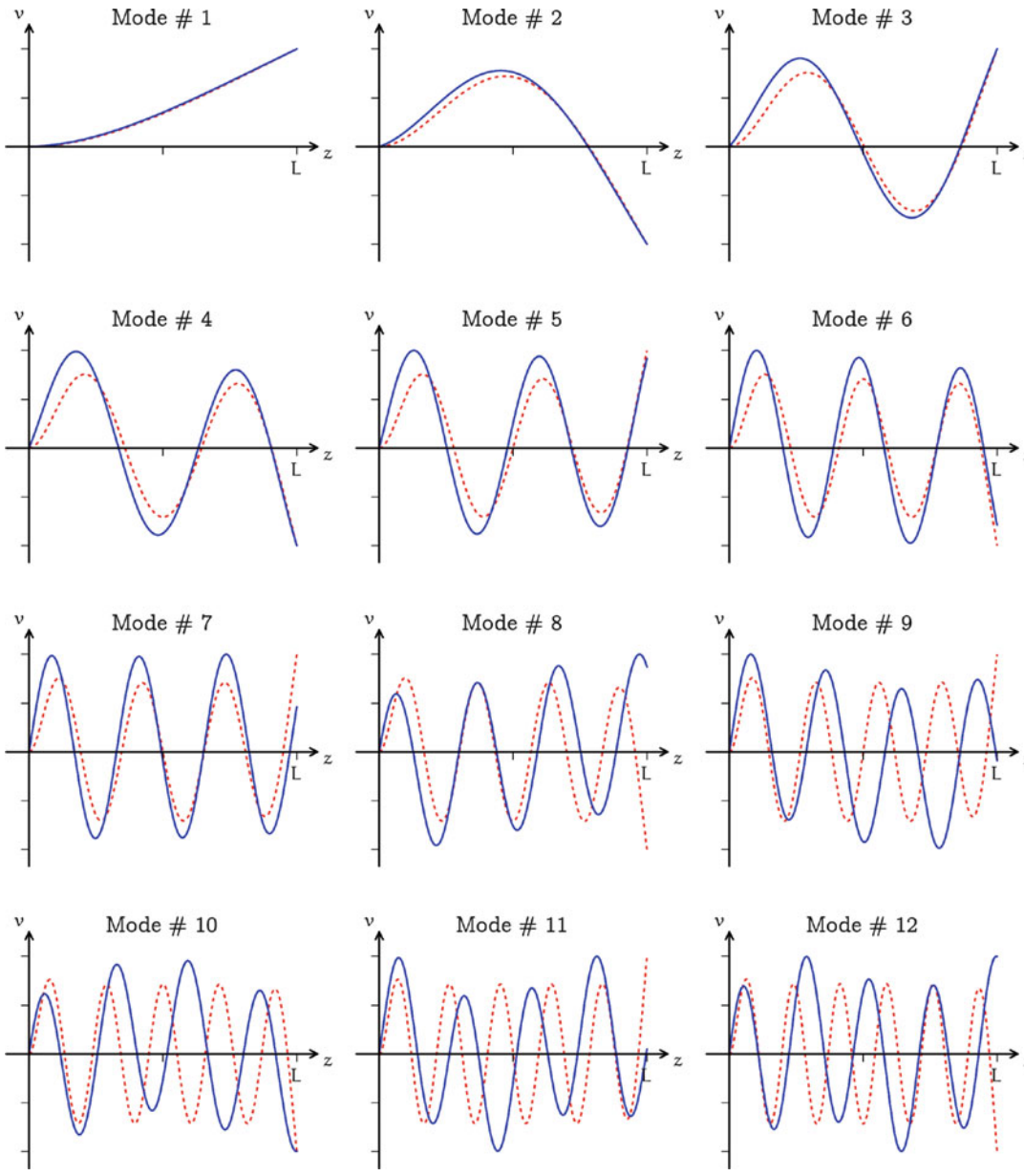

Vibrations of Beams for Seismic Response Estimation, Fig. 3 First 12 modal shapes of the Euler-Bernoulli beam (*dashed red*) and Timoshenko beam (*solid blue*)

$$v(z,t) = \int_{-\infty}^{+\infty} d\tau \int_{0}^{L} f(\xi, t-\tau) h(z,\tau;\xi) d\xi$$

The unit complex sinusoidal action with the fixed frequency ω applied at the section $z = z_o$ is

$$f(z,t) = \delta(z - z_o) e^{i\omega t}$$

Given the *complex frequency response function* $H(z, \omega; z_o)$, the response is given by

$$v(z,t) = H(z,\omega;z_o) e^{i\omega t}$$

Vibrations of Beams for Seismic Response Estimation, Table 1 Parameters of first 12 modes of Euler-Bernoulli beam

#	ω	k_1	k_2	D_1	D_2	D_3	D_4	ω/k_1
1	11.12	0.94	0.94	−5.00e-01	3.67e-01	5.00e-01	−3.67e-01	11.86
2	69.68	2.35	2.35	5.00e-01	−5.09e-01	−5.00e-01	5.09e-01	29.69
3	195.09	3.93	3.93	−5.00e-01	5.00e-01	5.00e-01	−5.00e-01	49.68
4	382.29	5.50	5.50	5.00e-01	−5.00e-01	−5.00e-01	5.00e-01	69.54
5	631.91	7.07	7.07	−5.00e-01	5.00e-01	5.00e-01	−5.00e-01	89.40
6	943.90	8.64	8.64	5.00e-01	−5.00e-01	−5.00e-01	5.00e-01	109.26
7	1318.23	10.21	10.21	−5.00e-01	5.00e-01	5.00e-01	−5.00e-01	129.11
8	1754.87	11.78	11.78	5.04e-01	−5.00e-01	−5.00e-01	5.00e-01	148.96
9	2253.79	13.35	13.35	−5.04e-01	5.00e-01	5.00e-01	−5.00e-01	168.80
10	2814.93	14.92	14.91	5.07e-01	−5.00e-01	−5.00e-01	5.00e-01	188.64
11	3438.27	16.49	16.48	−5.08e-01	5.01e-01	4.99e-01	−4.99e-01	208.47
12	4123.74	18.06	18.05	5.12e-01	−5.01e-01	−5.00e-01	5.00e-01	228.29

Vibrations of Beams for Seismic Response Estimation, Table 2 Parameters of first 12 modes of Timoshenko beam

#	ω	k_1	k_2	D_1	D_2	D_3	D_4	ω/k_1	ω/k_2
1	10.79	0.93	0.91	−4.97e-01	3.77e-01	4.97e-01	−3.60e-01	11.55	
2	58.20	2.28	2.01	4.59e-01	−6.12e-01	−4.59e-01	4.76e-01	25.56	–
3	138.73	3.79	2.80	−3.92e-01	7.10e-01	3.92e-01	−3.89e-01	36.63	–
4	230.57	5.27	3.13	3.02e-01	−8.39e-01	−3.02e-01	3.04e-01	43.75	–
5	328.14	6.76	3.05	−2.01e-01	8.86e-01	2.01e-01	−1.99e-01	48.52	–
6	426.14	8.24	2.53	−1.14e-01	9.27e-01	1.14e-01	−1.16e-01	51.74	–
7	520.37	9.65	1.20	−5.98e-02	9.30e-01	5.98e-02	−3.96e-02	53.95	–
8	568.55	10.37	1.36	2.13e-01	7.69e-01	−2.13e-01	3.14e-02	54.84	417.59
9	620.33	11.14	2.44	−1.73e-01	8.02e-01	1.73e-01	4.98e-02	55.66	254.07
10	654.90	11.66	3.00	−2.04e-01	−7.63e-01	2.04e-01	−5.23e-02	56.15	218.09
11	726.85	12.75	4.02	−2.34e-01	7.24e-01	2.34e-01	5.37e-02	57.01	180.80
12	762.49	13.29	4.48	1.72e-01	8.02e-01	−1.72e-01	5.99e-02	57.38	170.13

Let F (z, ω) be the Fourier transform of the action f (z, t) which is assumed to be an integrable function, so that

$$F(z,\omega) = \int_{-\infty}^{+\infty} f(z,t)e^{-i\omega t}dt$$

and

$$f(z,t) = \frac{1}{2\pi}\int_{-\infty}^{+\infty} F(z,\omega)e^{+i\omega t}d\omega$$

The complex frequency response function is the Fourier transform of the impulse response function

$$H(z,\omega;z_o) = \int_{-\infty}^{+\infty} h(z,\tau;z_o)e^{-i\omega\tau}d\tau$$

$$h(z,\tau;z_o) = \frac{1}{2\pi}\int_{-\infty}^{+\infty} H(z,\omega,z_o)e^{i\omega\tau}d\omega$$

Introduced the Fourier transform of the response

$$V(z,\omega) = \int_{-\infty}^{+\infty} v(z,t)e^{-i\omega t}dt$$

and

V

$$v(z,t) = \frac{1}{2\pi}\int_{-\infty}^{+\infty} V(z,\omega)e^{+i\omega t}d\omega$$

the excitation-response relation for Fourier transform is

$$V(z,\omega) = \int_0^L H(z,\omega;\xi)F(\xi,\omega)d\xi$$

so that

$$v(z,t) = \frac{1}{2\pi}\int_{-\infty}^{+\infty} e^{i\omega t}d\omega \int_0^L H(z,\omega;\xi)d\xi \int_{-\infty}^{+\infty} f(\xi,\tau)e^{-i\omega\tau}d\tau$$

and

$$V(z,\omega) = \int_{-\infty}^{+\infty} e^{-i\omega\tau}d\omega \int_0^L h(z,\tau;\xi)d\xi \frac{1}{2\pi} \int_{-\infty}^{+\infty} F(\xi,\omega)e^{+i\omega\tau}d\omega$$

Statistical Characteristics of the Excitation

Let f(z, t) be a random space-time processes. In order to describe this processes, it is introduced the *ensemble average* or *expected value*

$$E[f(z,t)] = m_f(z,t)$$

the *space-time correlation*

$$E[f(z_1,t_1)f(z_2,t_2)] = R_f(z_1,z_2,t_1,t_2)$$

and the *space-time covariance*

$$E[(f(z_1,t_1) - m_f(z_1,t_1))\ (f(z_2,t_2) - m_f(z_2,t_2))] = \Gamma_f(z_1,z_2,t_1,t_2)$$

It is assumed that the previous characteristics are sufficient to describe the excitation.

Considering the case of weak stationary process, the mean is independent on t, and the space-time correlation depends on $\tau = t_2 - t_1$ so that

$$E[f(z,t)] = m_f(z)$$
$$E[f(z_1,t)f(z_2,t+\tau)] = R_f(z_1,z_2,\tau)$$
$$E[(f(z_1,t) - m_f(z_1))(f(z_2,t+\tau) - m_f(z_2))] = = \Gamma_f(z_1,z_2,\ \tau) = R_f(z_1,z_2,\tau) - m_f(z_1)m_f(z_2)$$

If $z_1 = z_2 = z$, the *autocovariance function* is obtained

$$\Gamma_f(z,\tau) = R_f(z,\tau) - m_f^2(z)$$

that for $\tau = 0$ reduces to the *variance*

$$\sigma_f^2(x) = E\left[f^2(z)\right] - m_f^2(z)$$

where $R_f(z,\tau)|_{\tau=0} = E\left[f^2(z)\right]$ is the *mean-square value*.

Let $S_f(z_1, z_2, \omega)$ be the *space-time cross-spectral density function*; this function is connected to the cross-correlation function by the *Wiener-Khintchine relations*:

$$S_f(z_1,z_2,\omega) = \frac{1}{2\pi}\int_{-\infty}^{+\infty} R_f(z_1,z_2,\tau)e^{-i\omega\tau}d\tau$$
$$R_f(z_1,z_2,\tau) = \int_{-\infty}^{+\infty} S_f(z_1,z_2,\omega)e^{i\omega\tau}d\omega$$

If $z_1 = z_2 = z$ and $\tau = 0$, the mean-square value can be expressed by the cross-spectral density function

$$E\left[f^2(z)\right] = \int_{-\infty}^{+\infty} S_f(z,\ z,\ \omega)d\omega$$

and for excitation with zero mean

$$\sigma_f^2(x) = \int_{-\infty}^{+\infty} S_f(z,z,\omega)d\omega$$

It is worth noting that earthquake-induced base accelerations are samples of non-stationary random process. Anyway, there is an interval,

called *strong motion phase*, where the base accelerations can be considered samples of stationary random process. The length of strong motion phase is T_S. It is commonly assumed that, if T_S is much greater than the period of the elementary oscillator, both the base accelerations and the response can be considered samples of stationary random process with zero mean.

Statistical Characteristics of the Response

The statistical characteristics of the response can be obtained from corresponding characteristics of the excitation by taking the averages of the previously introduced relations. The expected value of the response can be obtained by equation

$$E[v(z,t)] = E\left[\int_{-\infty}^{+\infty} d\tau \int_{0}^{L} f(\xi, t-\tau)h(z,\tau,\xi)d\xi\right]$$

and interchanging the integral operators and mean operator, the following equation is obtained:

$$E[v(z,t)] = \int_{-\infty}^{+\infty} d\tau \int_{0}^{L} E[f(\xi, t-\tau)]h(z,\tau;\xi)d\xi$$

where E[f(z, t)] is the mean of the excitation. If the excitation is a stationary processes, its mean value is constant, $E[f(z,t)] = m_f(z)$, and also the mean value of the response is constant, $E[v(z,t)] = m_v(z)$, where

$$m_v(z) = \int_{-\infty}^{+\infty} d\tau \int_{0}^{L} m_f(\xi)h(z,\tau;\xi)d\xi$$

If in addition $m_f(z) = 0$, as for the seismic excitation, then $m_v(z) = 0$.

The space-time correlation function of the response is obtained by average of the product of $v(z_1, t)$ and $v(z_2, t + \tau)$, which are given by the impulse response function

$$E[v(z_1,t), v(z_2,t+\tau)] = E\left[\int_{-\infty}^{+\infty} d\theta_1 \int_{0}^{L} f(\xi_1, t-\theta_1)h(z_1,\theta_1;\xi_1)d\xi_1 \times \int_{-\infty}^{+\infty} d\theta_2 \int_{0}^{L} f(\xi_2, t+\tau-\theta_2)h(z_2,\theta_2;\xi_2)d\xi_2\right]$$

and interchanging the integral operators and mean operator

$$E[v(z_1,t)v(z_2,t+\tau)] = \int_{-\infty}^{+\infty} d\theta_1 \int_{-\infty}^{+\infty} d\theta_2 \int_{0}^{L} d\xi_1 \times \int_{0}^{L} E[f(\xi_1, t-\theta_1)f(\xi_2, t+\tau-\theta_2)]h(z_1,\theta_1;\xi_1)h(z_2,\theta_2;\xi_2)d\xi_2$$

If the excitation is stationary, then its space-time correlation is independent of t and so is the response space-time correlation

$$R_v(z_1,z_2,\tau) = \int_{-\infty}^{+\infty} d\theta_1 \int_{-\infty}^{+\infty} d\theta_2 \int_{0}^{L} d\xi_1 \times \int_{0}^{L} R_f(\xi_1,\xi_2,\tau+\theta_1-\theta_2)h(z_1,\theta_1;\xi_1)h(z_2,\theta_2;\xi_2)d\xi_2$$

Applying the Wiener-Khintchine relations, the space-time cross-spectral density of the response can be obtained by the following:

$$S_v(z_1, z_2, \omega) = \int_0^L d\xi_1 \int_0^L d\xi_2 \int_{-\infty}^{+\infty} h(z_1, \theta_1; \xi_1) d\theta_1 \int_{-\infty}^{+\infty} h(z_2, \theta_2; \xi_2) d\theta_2 \times \frac{1}{2\pi} \int_{-\infty}^{+\infty} R_f[\xi_1, \xi_2, \tau + \theta_1 - \theta_2] e^{-i\omega\tau} d\tau$$

Introducing in the previous integrals the unity products $e^{-i\omega\theta_1} e^{i\omega\theta_1}$ and $e^{-i\omega\theta_2} e^{i\omega\theta_2}$, by the frequency response function

$$H(z_1, -\omega; \xi_1) = \int_{-\infty}^{+\infty} h(z_1, \theta_1; \xi_1) e^{i\omega\theta_1} d\theta_1$$

$$H(z_2, \omega; \xi_2) = \int_{-\infty}^{+\infty} h(z_2, \theta_1; \xi_2) e^{-i\omega\theta_2} d\theta_2$$

and introducing the space-time cross-spectral density of the excitation,

$$S_f(\xi_1, \xi_2, \omega) = \frac{1}{2\pi} \int_{-\infty}^{+\infty} R_f[\xi_1, \xi_2, \tau + \theta_1 - \theta_2] e^{-i\omega(\tau + \theta_1 - \theta_2)} d(\tau + \theta_1 - \theta_2)$$

the following expression to determine $S_v(z_1, z_2, \omega)$ is obtained:

$$S_v(z_1, z_2, \omega) = \int_0^L \int_0^L H(z_1, -\omega, \xi_1) S_f[\xi_1, \xi_2, \omega] H(z_2, \omega, \xi_2) d\xi_1 d\xi_2$$

Natural Modes and Frequencies

The dynamic proprieties of the systems can be described in terms of *natural modes*, $\tilde{v}$, and corresponding *natural frequencies*, ω. In what follows, the natural modes will be expressed in terms of both deflection, $v_j(z) = \tilde{v}(z)$, and rotation, $\theta_j(z)$, where j is the mode number. Once the natural modes have been found, the equations of motion Eq. 7 can be reduced to

$$m_j \frac{d^2 g_j}{dt^2} + k_j g_j = f_j$$

where m_j, k_j, and f_j are, respectively, the generalized mass, stiffness, and force corresponding to mode j, given by

$$\begin{cases} m_j = \int_0^L \left(\rho A v_j^2 + \rho I \theta_j^2 \right) dz \\ k_j = \int_0^L \left(-EI \left(\frac{d\theta_j}{dz} \right)^2 + GK \left(\frac{d\gamma_j}{dz} \right)^2 \right) dz, \quad \text{with} \quad k_j = \omega_j^2 m_j \\ f_j = \int_0^L (q v_j + m \theta_j) dz \end{cases} \tag{9}$$

and g_j is the jth principal coordinate. In the preceding, the following orthogonality properties of the modes have been used (Bishop and Price 1977):

$$\begin{cases} \int_0^L (\rho A v_j v_k + \rho I \theta_j \theta_k) dz = a_{kj} \delta_{kj} \\ \int_0^L \left(-EI \frac{d\theta_j}{dz} \frac{d\theta_k}{dz} + GK \frac{d\gamma_j}{dz} \frac{d\gamma_k}{dz} \right) dz = a_{kj} \omega_k^2 \delta_{kj}, \quad \text{with} \quad \delta_{kj} = \begin{cases} 1 & \text{if} \quad k = j \\ 0 & \text{if} \quad k \neq j \end{cases} \end{cases}$$

Once the g_j are known, the values of displacements are given by

$$v(z,t) = \sum_{j=1}^{\infty} v_j(z) g_j(t), \quad \theta(z,t) = \sum_{j=1}^{\infty} \theta_j(z) g_j(t)$$

If a modal damping ν_j is assumed, the equations of motion are

$$m_j \frac{d^2 g_j}{dt^2} + 2\nu_j \sqrt{k_j m_j} \frac{dg_j}{dt} + k_j g_j = f_j$$

that can also be written as

$$\frac{d^2 g_j}{dt^2} + 2\nu_j \omega_j \frac{dg_j}{dt} + \omega_j^2 g_j = \frac{1}{m_j} f_j$$

Let $h_j(t)$ be the single degree of freedom unit impulse response function. With initial conditions $g_i = 0$ and $dg_j/dt = 0$, and assuming distributed load $q = \delta(z - z_0)\,\delta(t)$ and distributed moments $m = 0$, the solution is

$$g_j(t; z_0) = h_j(t) v_j(z_0)$$

where

$$h_j(t) = \begin{cases} 0 & t \le 0 \\ \dfrac{1}{m\omega_j \sqrt{1-\nu_j^2}} e^{-\nu_j \omega_j t} \sin\left(\omega_j \sqrt{1-\nu_j^2}\, t\right) & t > 0 \end{cases}$$

so that

$$h(z,t;z_0) = \sum_{j=1}^{\infty} v_j(z) v_j(z_0) h_j(t)$$

and using the Fourier transform relation, the complex frequency response is

$$H(z,\omega;z_0) = \sum_{j=1}^{\infty} v_j(z) v_j(z_0) H_j(\omega)$$

where the single degree of freedom unit complex frequency response function is given by

$$H_j(\omega) = \frac{1}{m\left(\omega_j^2 - \omega^2 + 2\nu_j \omega_j \omega i\right)}$$

Inserting in the previous equations, the following expressions for space-time correlation and space-time cross-spectral density are obtained:

$$R_v(z_1,z_2,\tau) = \sum_{j=1}^{\infty}\sum_{k=1}^{\infty} v_j(z_1) v_k(z_2) \int_{-\infty}^{+\infty}\int_{-\infty}^{+\infty} h_j(\theta_1) h_k(\theta_2) d\theta_1 d\theta_2 \times \int_0^L\int_0^L v_j(\xi_1) v_k(\xi_2) R_f[\xi_1,\xi_2,\tau+\theta_1-\theta_2] d\xi_1 d\xi_2 \tag{10}$$

$$S_v(z_1,z_2,\omega) = \sum_{j=1}^{\infty}\sum_{k=1}^{\infty} v_j(z_1) v_k(z_2) H_j(-\omega) H_k(+\omega) \times \int_0^L\int_0^L v_j(\xi_1) v_k(\xi_2) S_f[\xi_1,\xi_2,\omega] d\xi_1 d\xi_2 \tag{11}$$

Application to the Beam Under Seismic Load

The concepts illustrated in the previous sections are applied to the case of the cantilever beam seen previously in the example, subjected to a seismic load. The seismic load is modeled by means of an elastic response spectrum according to the European standard for seismic actions (Eurocode 8 2004). It has been assumed a type 1 elastic response spectrum with a ground type C, with parameters:

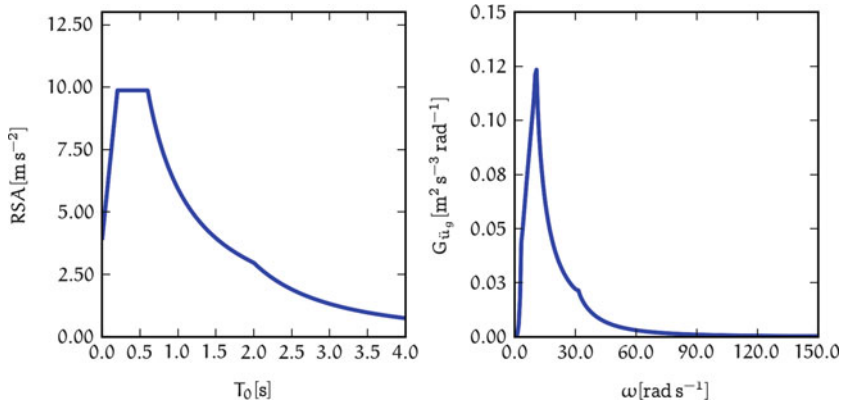

Vibrations of Beams for Seismic Response Estimation, Fig. 4 Elastic response spectrum according to Eurocode 8 and corresponding power spectral density function

$a_g = 0.355\,g$ (Peak ground acceleration), $S = 1.15$ (Soil factor)
$T_B = 0.20\,s$, $T_C = 0.60\,s$, $T_D = 2.00\,s$

A 5 % damping, $\nu = 0.05$, was adopted. The response spectrum in terms of pseudo-accelerations (RSA) is shown in Fig. 4a.

In order to apply what presented in previous sections, the power spectral density function, $G_{\ddot{u}_g}$, corresponding to the assumed response spectrum is needed. The method proposed in (Cacciola et al. 2004) is used. The time observing window (coincident with the strong motion phase) T_S has been set to 10s, while the cut-off frequency is $\omega_u = 150$ rad/s and the frequency step is $\Delta\omega = 2\pi/T_S = 0.63$ rad/s. An iterative scheme has been used as suggested in (Cacciola 2010), and the power spectral density function obtained is shown in Fig. 4b.

The generation of a time history of base acceleration is achieved by means of superposition of N_a harmonics with random phases Φ_i as follows:

$$\ddot{u}_g(t) = \varphi(t)\sum_{i=1}^{N_a}\sqrt{2G_{\ddot{u}_g}(i\Delta\omega)\Delta\omega}\cos(i\Delta\omega + \Phi_i)$$

where $\varphi(t)$ is the modulating function (which changes the total energy but not its distribution among the frequencies; see Fig. 4b) (Cacciola 2010):

$$\varphi(t) = \begin{cases} \left(\frac{t}{t_1}\right)^2 & \text{for } t \le t_1 \\ 1 & \text{for } t_1 < t \le t_2 \\ e^{-\beta(t-t_2)} & \text{for } t > t_2 \end{cases}$$

with $t_2 = t_1 + T_S$. In the present case, it was assumed $t_1 = 10$s and $\beta = 0.3\ s^{-1}$. An example of the generated $\ddot{u}_g(t)$ is shown in Fig. 5.

The problem of the beam subjected to the base acceleration given by $\ddot{u}_g(t)$ can be solved by means of modal analysis, as formulated in Eq. 9.

In the case of seismic action represented by base accelerations $\ddot{u}_g(t)$, the external loads are

$$\begin{cases} q = -\rho A\ddot{u}_g(t) \\ m = 0 \end{cases}$$

and therefore:

$$f_j = -\int_0^L \rho A\ddot{u}_g(t)v_j dz = -\Gamma_j\ddot{u}_g(t), \text{with}$$
$$\Gamma_j = \int_0^L \rho A v_j dz$$

Once the time histories of g_j have been determinated, the solution is given by

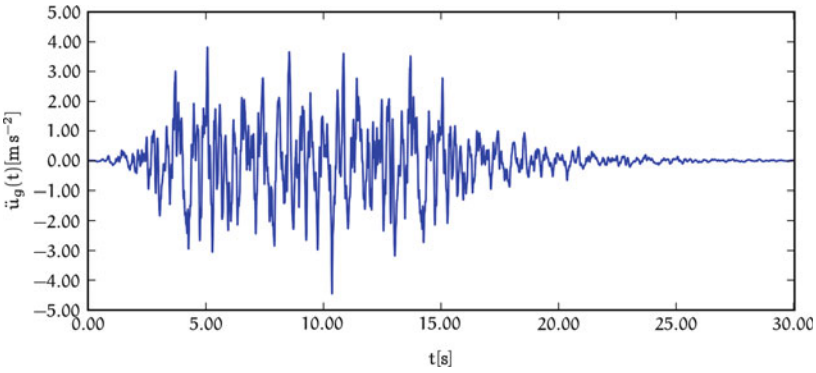

Vibrations of Beams for Seismic Response Estimation, Fig. 5 Example of a time history of acceleration compatible to power spectral density function $G_{\ddot{u}_g}$

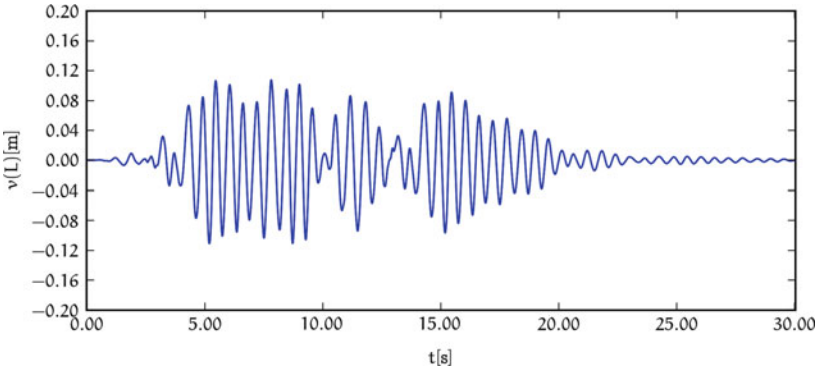

Vibrations of Beams for Seismic Response Estimation, Fig. 6 Displacement at free end for base accelerations of Fig. 5

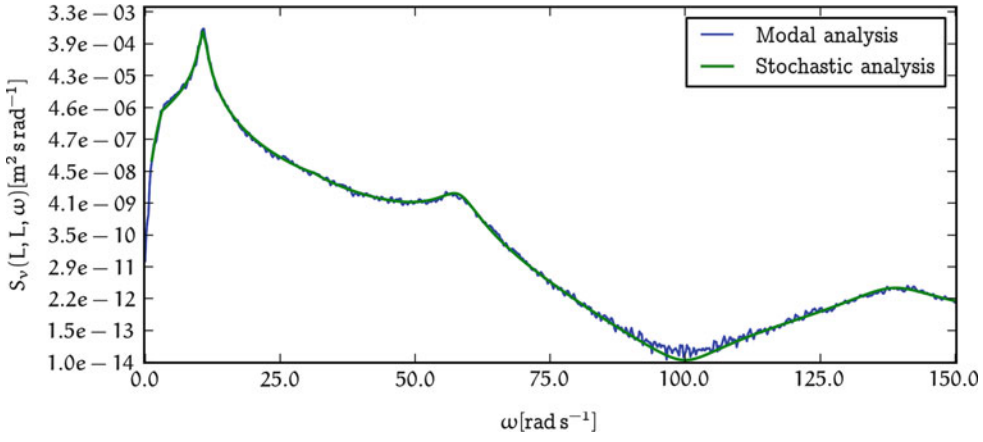

Vibrations of Beams for Seismic Response Estimation, Fig. 7 Power spectral density function of free end displacement by means of modal analysis with generated spectrum compatible accelerograms and by means of stochastic analysis

$$v(z,t) = \sum_{j=1}^{N_p} v_j(z) g_j(t), \quad \theta(z,t) = \sum_{j=1}^{N_p} \theta_j(z) g_j(t)$$

where N_p is the number of modes considered in the solution. For example, the displacement at the free end, $v(L)$, for the base acceleration shown in Fig. 5 and assuming $N_p = 10$ (the modal contribution tends to be negligible quite rapidly) is shown in Fig. 6.

The power spectral density function of the displacement at free end, $S_v(L, L, \omega)$ is shown in Fig. 7, compared to that evaluated by mean of Eq. 11. As can be appreciated, the same results are obtained using both procedures.

Cross-References

- ▶ Random Process as Earthquake Motions
- ▶ Stochastic Analysis of Linear Systems
- ▶ Stochastic Ground Motion Simulation
- ▶ Time History Seismic Analysis

References

Bishop R, Price W (1977) Coupled bending and twisting of a Timoshenko beam. J Sound Vib 50:469–477
Cacciola P (2010) A stochastic approach for generating spectrum compatible fully nonstationary earthquakes. Comput Struct 88:889–901
Cacciola P, Colajanni P, Muscolino G (2004) Combination of modal responses consistent with seismic input representation. J Struct Eng 130:47–55
Crandal SH (1979) Random vibration of one- and two-dimensional structures. In: Krishnaiah PR (ed) Developments in statistics, vol 2. Academic, Waltham
Elishakoff I (1988) Random vibration of discrete and continuous systems. In: Schiehlen W, Wedig W (eds) Analysis and estimation of stochastic mechanical systems, International centre for mechanical sciences – CISM, courses and lectures no. 303. Springer, Berlin
Eurocode 8 (2004) Design of structures for earthquake resistance – part 1: general rules, seismic actions and rules for buildings. European Committee for Standardization (CEN), Bruxelles
Hagedorn P, DasGupta A (2007) Vibrations and waves in continuous mechanical systems. Wiley, Chichester
Lin YK (1967) Probabilistic theory of structural dynamics. McGraw-Hill, New York
Robson DJ, Dodds CJ, Macvean DB, Paling VR (1971) Random vibration, International centre for mechanical sciences – CISM, courses and lectures no. 115. Springer, Berlin
Timoshenko SP (1921) On the correction factor for shear of the differential equation for transverse vibrations of bars of uniform cross-section. Philos Mag 41:744–746
Timoshenko SP (1922) On the transverse vibrations of bars of uniform cross-section. Philos Mag 43:125–131

Volcanic Eruptions, Real-Time Forecasting of

Andrew F. Bell[1], Christopher R. J. Kilburn[2] and Ian G. Main[1]
[1]School of GeoSciences, University of Edinburgh, Edinburgh, UK
[2]Department of Earth Sciences, Aon Benfield UCL Hazard Centre, University College London, London, UK

Synonyms

Eruption precursors; Event-tree eruption forecasts; Probabilistic and deterministic eruption forecasting

Introduction

One of the primary goals of volcanology is to develop methods to forecast future eruptive activity. Good forecasts have the potential to increase the effectiveness of hazard mitigation plans, allowing well-timed evacuations or improved management of a return to exclusion zones. Volcanic earthquakes and seismicity are key datasets that form the basis for eruption forecasts. Seismometers are amongst most widely installed volcano monitoring equipment. Increased seismicity is a primary indicator of volcanic unrest, and eruptions are frequently preceded by changes in the rate, location, magnitude, and type of earthquakes. In combination with geodetic data, they can provide indications as to the volumes and locations of magma.

Earthquakes provide an insight into otherwise hidden processes occurring at volcanoes and that may have a causal link to eruptive activity, such

as edifice deformation, magma migration, and magma failure. Consequently, changes in the seismic activity at a volcano can be expected to provide information on the state of unrest, whether unrest is likely to lead to an eruption, and, if so, when. It may also in future provide information about changes in the nature of eruptive activity and the style, size, and location of impending activity.

A forecast is a probabilistic estimate of future activity based on current observations and past behavior. It needs to include aspects of timing, as well as physical attributes of the activity itself. A forecasting model quantitatively links observations to these probabilistic estimates, by applying empirical statistics or physical and theoretical considerations. But, how well do different forecasting models perform? Many evaluations of forecast performance have been undertaken retrospectively. These types of analyses are important for developing and refining methods and for identifying the action of different processes. However, the true performance of forecasts can only be fully evaluated through real-time forecasting (i.e., with forecasts issued ahead of the eruption) and rigorous testing. This approach eliminates conscious or subconscious biases due to data, model, and parameter selection.

Forecasting Eruptive Activity Using Seismicity Data

What Is a Forecast?

Although the words "forecast" and "prediction" have similar dictionary definitions, the associated connotations are different in different disciplines of geophysics. In some instances, the words are used interchangeably. For example, the US National Weather Service has a "Weather Prediction Center" which issues "Short Range Forecasts" of weather conditions (http://www.hpc.ncep.noaa.gov/). This topic has been heavily debated in the earthquake community. The term "prediction" has come to mean a highly specific statement about the time, location, and magnitude of a future event, generally with very narrow confidence bounds. In contrast, a "forecast" is a more probabilistic statement, with a greater (and, perhaps, better quantified) uncertainty. It is broadly accepted that reliable and accurate earthquake "prediction" is unlikely to be a possibility, except in exceptional circumstances (Jordan et al. 2011).

In volcanology, similar distinctions have been made between more specific, shorter-term predictions and more general, longer-term forecasts (Swanson et al. 1983). In some scenarios, highly confident and precise statements about future volcanic activity may well be justifiable. However, such statements can readily be included as one end-member of a broader, probabilistic framework of eruption "forecasting" that incorporates more common, but less confident, statements (Sparks 2003). Such a probabilistic framework implies that there is an effort to more fully account for uncertainties in data, models, and system behavior, however small or large this may be. It can also accommodate and aggregate information from empirical observations, expert opinion, and physics-based models.

Eruption forecasts can be categorized on the basis of data sources and timescales (Marzocchi and Bebbington 2012). Short-term eruption forecasting is predominantly based on the observation of precursors. A precursor is an observable phenomenon that correlates with an increase in the probability of occurrence of a certain type of eruptive activity. Short-term forecasting is usually associated with timescales of hours to weeks or months before the event and is the type of information associated with evacuations. Forecasts can include aspects of timing but also eruption style, size, and location. Seismic activity is an important eruption precursor and plays a key role in short-term forecasting. Long-term forecasting uses historical and geological data to establish probability distributions for eruption frequencies, magnitudes, and styles. Although seismology may play a role, for example, in characterizing the size and location of the volcanic plumbing system, it is relatively minor compared to other considerations for long-term forecasting purposes.

Short-term forecasts use properties of monitoring data and other physical observations to determine the time-dependent probability of different types of activity. These probabilities may be based on physical models or on empirical statistics derived from observations before previous eruptions. The form in which a forecast is presented has implications for its utility and verifiability, and, as yet, there is no established standard or protocol for how a forecast is formulated. There are important differences between, for example, statements such as "the eruption will occur in x days +/− y days," which assume that current unrest will certainly lead to an eruption, and those such as "there is an x% probability of an eruption within y days," which do not. Probabilities of different phenomena based on certain models are likely to be conditional on other imprecisely known factors, such as the probability that the volcano is currently in "unrest" or that unrest will lead to an eruption. The resulting forecasts will be associated with confidence bounds reflecting the uncertainty in the process, statistics, and underlying model. Consequently, some forecasts will be associated with narrower confidence bounds than others.

Seismic Eruption Precursors

Numerous seismic phenomena have been observed to precede eruptions and changes in eruptive activity (Chouet and Matoza 2013). These include changes in the characteristics of earthquakes and in the seismic properties of the volcanic edifice and surrounding crust (e.g., seismic velocity or anisotropy). Earthquakes can indicate deformation and failure of the volcanic edifice (produced by increased magma pressure or flank instability) and the movement of magma and other fluids in the crust. In addition, earthquakes can be generated by deformation of magma itself, providing warnings, for example, of changes in the growth and failure of lava domes. Consequently, factors including changes in the rate, location, and magnitude of earthquakes, changes in the type of earthquakes, and changes in the focal mechanisms of earthquakes might contain information about changes in probability of eruptive activity, though it can be hard to assign a unique underlying cause.

Earthquake Types

A variety of different earthquakes are observed at volcanoes, characterized by frequency content and duration. The appearance of different types of earthquakes can be sufficient to diagnose the activation of particular physical processes.

Seismic waves from volcano-tectonic (VT) earthquakes have a sharp onset and high-frequency content and indicate brittle failure of the volcanic edifice, underlying crust, or even the magma itself (McNutt 2005). Low-frequency (LF) or long-period earthquakes have frequencies that are generally lower than for VT earthquakes, with an absence of high frequencies, and originate from the movement of magmatic or hydrothermal fluids. Volcanic tremor has frequencies similar to LF events but sustains its amplitude for longer periods of time (from minutes to days). Hybrid events have a high-frequency onset, identical to VT events, but an increased low-frequency coda more like LF events. Hybrid events have been interpreted as fluid movement following an initial brittle failure event or by the scattering of high-frequency signals during wave propagation within the edifice.

Elevated Earthquake Rates

The most common indicator of volcanic unrest is an increase in the rate of earthquakes. Volcano-tectonic earthquakes are generated by stick–slip shear motion on faults within the volcanic edifice. Each event represents an increment of brittle failure and the accumulation of damage. Increased rates of these events indicate increased rates of deformation and can result from combinations of factors including (1) an increase in the stresses driving deformation, such as increasing magma pressure or flank deformation; (2) progressive material weakening (damage) of the volcanic edifice such that deformation rates increase at a constant driving stress; (3) an increased proportion of the brittle component of deformation (i.e., the seismic to aseismic ratio); or (4) thermal activation of the hydrothermal system. Although some eruptions are preceded by years of elevated rates of seismicity, other eruptions can occur with

little or no change in seismicity. Extended periods of seismic unrest are expected in situations where there is prolonged magma accumulation, the progressive formation of a fracture pathway, or slow evolution of edificial stresses. In contrast, little seismicity is expected where a magma pathway has been preserved from a previous eruption, where magma rapidly rises from depth to the surface, or where temperature and stress conditions promote aseismic deformation. The total strain inferred from earthquakes typically represents only a very small proportion of the total deformation observed at the surface and is biased toward large, more dynamic events occurring at shallow depth. Accordingly inferences made from the earthquake seismograms or population dynamics may preserve this bias.

The simplest model for the temporal occurrence of earthquakes is a Poisson process. In this model, the average rate of earthquakes is λ, and occurrence times are random and independent. If λ is constant with time, the model is called a "homogenous Poisson process." In the more general case that $\lambda(t)$ varies with time, the model is called a "non-homogenous Poisson process"; increases in $\lambda(t)$ for volcanic earthquakes are potential precursors to eruptive activity. For a Poisson process, the times between successive earthquakes are described by an exponential distribution, and earthquake rates (the numbers of earthquake occurring within a given time window) are described by a Poisson distribution. Aside from perhaps the very largest events, tectonic earthquake occurrence has been shown to be non-Poissonian (i.e., the variations in earthquake rate are greater than would be expected by from a Poisson process), and this is also the case for volcanic earthquakes. More realistic point process earthquake occurrence models, such as the ETAS (epidemic-type aftershock sequence) model, incorporate earthquake interaction and triggering processes on top of an underlying Poisson process. However, even outside periods of eruptive activity, volcanic seismicity is characterized by swarms and other nonstationary phenomena, resulting in variations in earthquake rate that are greater than those that can be expected from a simple earthquake triggering model. These variations mean that it can be difficult to identify anomalous increases in the underlying earthquake rate $\lambda(t)$ especially when the background behavior is poorly characterized.

Preeruptive changes in earthquake rate can take different forms. At a volcano that has been quiescent for many years, simply the occurrence of detectable earthquakes may be indicative of the resupply of magma and the approach to eruption. At volcanoes where there is ongoing seismicity, a change in the system (e.g., a switch from deformation being primarily driven by tectonic process to deformation being driven by magma pressure) may be indicated by step changes in earthquake rate. Systematic increases in earthquake rate with time are frequently reported before eruptions. Such sequences can evolve over a wide range of timescales, from hours to years, and it has been argued that they may potentially allow more direct forecasts of the timing of an eruption.

Increases in the rate of earthquakes originating within a magma body are likely to be indicative of processes including magma pressurization, increased rates of magma movement, increased flow of non-magmatic fluids or gases, or changes in the rheology of the magma. Consequently, such changes are likely to correlate with changes in the probability of an eruption or a change in eruptive behavior.

Completeness Magnitude

Identifying and quantifying changes in earthquake rates relies on accurate determination of the earthquake catalogue completeness magnitude. The completeness magnitude is a lower magnitude threshold above which all earthquakes are recorded. As the frequency-magnitude relation is exponential for small magnitudes, small changes in the completeness magnitude can lead to apparently significant changes in rate if they are unaccounted for. Changes in completeness magnitude can arise from improvements in monitoring networks, seasonal noise changes, or hypocenter migration. Completeness magnitude is also correlated with earthquake rate; at times of high earthquake rate, a greater proportion of

small magnitude earthquakes will be undetected. Correct determination of the completeness magnitude is also important before any analysis of the frequency (F) versus magnitude (m) distribution. As in the case of tectonic earthquakes, this takes the form of a Gutenberg–Richter distribution, $\log(F) = a - bm$, where a and b are model parameters related, respectively, to total event rate and the relative proportion of large and small events.

There are a range of different quantitative methods to determine the completeness magnitude for an earthquake catalogue. The three most frequently used methods are the maximum-curvature method, the goodness-of-fit test, and the *b*-value stability method (Mignan and Woessner 2012). These methods are all based on the assumption that the earthquake magnitudes follow a Gutenberg–Richter distribution. In scenarios where the rate (and completeness magnitude) increases with time, it is likely that these methods systematically underestimate the completeness magnitude. This results in an underestimate of the total number of events above the apparent threshold, because several small events are not detected.

Earthquake Magnitudes

Earthquake magnitude is a measure of the size of the earthquake. Magnitude is proportional to the logarithm of the amount of energy released and depends on the amount of slip and the area of the source. Larger magnitude earthquakes reflect larger amounts of energy release, greater deformation and slip, and a greater increment of brittle damage. Events of magnitude 5–6 have been recorded in volcanic areas. However, volcanic earthquake catalogues are commonly dominated by events of magnitudes 1–3. An earthquake of magnitude 2 is associated with movements of about 10 mm over a distance of 100 m (McNutt 1999). If the b-value of the frequency–magnitude distribution remains constant, increases in the maximum magnitude in a given time window reflect an increase in earthquake rate and so are a proxy measure for rate, albeit with a much greater uncertainty in mmax than N. A decrease in the b-value of the frequency–magnitude distribution can also result in proportionally more large events.

The frequency–magnitude distribution of earthquakes, and in particular the seismic b-value, describes the relative proportions of large and small events. Changes in b-value have been linked to changes in stress and to changes in the populations of faults and fractures in the volcanic edifice. These observations are supported by those from laboratory experiments and the predictions of theoretical models.

Large tectonic earthquakes have also been reported as precursors to eruptions. Global studies suggest a correlation between large events and the onset of eruptions or changes in eruptive style (Schmid and Grasso 2012). Earthquakes occurring within a few fault lengths of the volcano may influence the magmatic system by a static stress transfer mechanism, directly dilating or compressing the plumbing system. These effects are also observed for "silent" earthquakes in the flanks of volcanoes such as Kilauea, Hawaii, where slip occurs too slowly to generate seismic waves but does result in a considerable static stress change. However, triggering effects have been identified over much larger distances of hundreds of kilometers. At these distances, static stress changes are small, and so any interaction is likely to be due to dynamic effects as the earthquake waves pass through the volcano. Potential mechanisms for this effect include the perturbation of the magma chamber and diffusion of pore fluids in the surrounding crust.

Hypocenter Migration

Earthquakes occur where the local deviatoric stress overcomes rock strength and friction. The stress field in a volcano is a function of tectonic and edificial stresses and magmatic and fluid-driven stresses. Consequently, earthquakes are expected to occur either where magmatic and fluid stresses are the greatest or where background stresses have already brought the edifice close to failure. In some instances, earthquake locations may be expected to indicate magma migration. There are many good examples where the location of earthquake hypocenters closely correlates with independent observations

of the location of magma, such as surface deformation signals and eruptive vents. This evidence is particularly strong at volcanoes where there is lateral migration of magma, including Krafla in Iceland and Kilauea in Hawaii. At Kilauea, the lateral migration of epicenters has been observed into one or both of the rift zones that emanate from the volcano's summit region. The most accurate locations indicate that events occur along a narrow range of depths, suggesting the unzipping of crust along a preferred stress horizon above a deeper rift-zone reservoir. In general, however, it remains unclear as to what extent earthquake hypocenters can be used to map magma migration.

Upward migration of earthquake sources might be expected to be a commonly observed precursor, mapping the movement of magma from depth to the surface. However, it is rarely reported. The absence of clear upward migrating signals may partly be explained by large uncertainties in estimates of the hypocentral location estimation, but, even in the case of well-located data, such patterns are rare. Alternatively, the breaking of the crust that occurs in the vicinity of a propagating magmatic fracture may involve fault movements that are too small to be detected at the surface; in this case, the detected volcanotectonic seismicity may reflect how stress changes across the deforming crust and volcanic edifice induce movements of existing, larger faults. Distributed deformation is also observed on a smaller scale in laboratory tests on natural rock samples in compression, where localization on or near the final macroscopic crack that controls bulk failure or fault often occurs only at the very last minute. In the case of a volcanic eruption, the final upward migration of magma through this cloud of seismicity is often rapid and accompanied by high levels of tremor and other seismic noise. These attributes place strong constraints on the reliability, accuracy, and timeliness of any eruption forecast based on inferences of physical processes from the seismicity.

Before many eruptions, elevated rates of earthquakes occur in several discrete clusters, kilometers across, located in different parts of the edifice. This behavior has been observed at a variety of different types of volcano including Mt Pinatubo, Mount St Helens, and Kilauea, with clusters separated by several kilometers horizontally or vertically. These different clusters may indicate distinct magma bodies, magma movement, or non-magmatic deformation processes. At volcanoes with flank instability, such as Kilauea and Mt Etna, elevated rates of earthquakes in the flank are indicative of increased rates of flank movement. These swarms can occur concurrently with seismicity associated with the magma plumbing system and have been observed to directly precede changes in eruptive activity.

Earthquake Focal Mechanisms

Earthquake focal mechanisms describe the nature of deformation at the earthquake source. Most VT earthquakes are double-couple, indicative of shear motion on a fault plane. The orientation of focal mechanism describes the stress field at the source. Rotations of the focal mechanism with time from, for example, strike-slip to reverse, have been reported before some eruptions and interpreted in terms of magma pressurization changing the orientations of the principal stresses in the vicinity of the magma body (Roman and Cashman 2006). Non-double-couple earthquakes indicate a more complex source, including tensile failure and events associated with finite volume changes, such as explosions or collapses. In Iceland, for example, such sources have been associated with tensile failure during the opening of subsurface cracks.

Factors Influencing the Characteristics of Precursory Seismicity

For magma to reach the surface along a new pathway, the magma pressure must be sufficient (1) to raise the magma to the surface against gravity, (2) to drive magma flow against the magma viscosity, and (3) to open the conduit against the crustal stress and rock strength sufficiently wide for magma flow. Patterns of precursory seismicity before any given eruption will reflect the details of the physical processes that result in that specific volcanic system satisfying these conditions. The volcanic system may

already be close to the eruptive conditions at the start of unrest, either because the system has not relaxed since the preceding eruption or because non-magmatic processes (e.g., flank movement or regional earthquakes) bring the system to this state. In this scenario, only a small amount of preeruptive magma-driven deformation may be required, with short-lived VT seismicity. After long repose times or large eruptions, or in tectonic settings that inhibit upward magma movement, greater amounts of magma-driven deformation are likely to be required before the necessary eruptive stress conditions are reached. Consequently, prolonged VT seismicity may be expected. These may be combined with changes in the statistical properties of seismicity such as changes with time in the clustering of events and their frequency–magnitude distribution.

Presence of a Preexisting Magma Pathway

Magma requires a physical through-going pathway in order to migrate from depth to the surface. The formation and opening of a pathway are generally associated with VT seismicity and so the state of any preexisting pathway influences the nature of precursory seismicity. At volcanoes where a pathway already exists, the onset of eruption, or a change in style of an ongoing eruption, may be associated with little additional deformation of the edifice. In this scenario, the deformation and seismicity that occur result from pressure changes within the magma body, leading to earthquakes in the surrounding edifice and, potentially, within the magma body itself. Depending on the rheology of the magma, these processes may be associated with seismicity resulting from brittle failure of the magma or tremor-like seismicity associated with fluid movement. Where a magma pathway does not exist before the start of unrest, the formation of a new magma pathway is expected to be associated with increased rates of VT seismicity, owing to faulting in the crust around a pressurized magma body. However, the general lack of a close correlation between the location of dikes and earthquake hypocenters suggests that the earthquakes themselves are unlikely be directly related to the formation of a magmatic pathway.

Volcanic Stress Conditions

Magma requires a sufficiently wide pathway through which to flow. For a pathway to open, magma pressure must exceed the minimum principle compressive stress. This can be achieved by an increase in magma pressure or by a reduction in the stress. Increases in magma pressure can be caused by the supply of additional magma from depth or by the vesiculation of magma, as a result of processes such as crystallization or stimulation by dynamic stress changes produced by the passage of seismic waves. Reduction in edificial stress conditions can occur by processes including flank instability, regional tectonic earthquakes, and time-dependent deformation of the edifice.

Magma Rheology

Magma composition, crystallinity, and temperature are primary factors controlling magma rheology. Magma rheology determines how readily it will flow through a pathway and how flow might generate earthquakes. Basic magma is generally hotter and less viscous than silicic magma, meaning it can flow through narrower pathways and with a lower driving pressure.

Forecasting Eruptions Using Precursory Seismic Phenomena

The previous sections have set out different types of precursory seismic phenomena and the different broad factors that influence their occurrence. However, many of these factors are poorly known at the start of unrest, and the complexity of volcanic systems mean that precursory patterns may vary considerably between eruptions. It is therefore a challenge to quantitatively link precursory behavior to probabilities of eruptive activity. Three different approaches are (1) using empirical statistics based on previous data, (2) using physics-based models, and (3) using the opinion of a group of experts. The boundaries between these approaches are indistinct, and the application of one almost certainly requires elements of the others.

Empirical Data

Probabilistic forecasts of future activity can be constructed using the empirical statistics of datasets associated with past preeruptive behavior. This methodology relies on the robust characterization and classification of precursory phenomena (both in archive datasets and in real-time monitoring data). The probability of different types of activity, within different time windows, can be determined on the basis of past correlation with one or more metrics, such as the rate of local VT earthquakes, the amplitude of tremor, or the occurrence of large magnitude regional earthquakes. The probability of an eruption can then be estimated, for example, from the number of times previous eruptions have been observed to occur when the given metrics have exceeded particular values. The confidence in the forecasts depends heavily on the quality and quantity of past data. At frequently active volcanoes with long-running monitoring programs (such as Kilauea and Mt Etna), the data are sufficient to build volcano-specific statistical models for precursory seismicity. At less frequently active volcanoes, those with less well-established monitoring programs, or those where the style of activity is changing, it is necessary to combine data with those from analogous volcanoes. This process involves a degree of subjectivity – just what are the most likely analogues, and how can the statistics be relatively weighted? Even when datasets are combined, current data archives are small and inconsistent. Regional and global initiatives to integrate monitoring datasets, and to collate historical data, will improve the basis for empirical forecasts.

Physics-Based Models

Physics-based models use an understanding of the physical process controlling the approach to eruption to quantitatively link aspects of seismic or other precursory phenomena to the properties of future eruptive activity. The biggest appeal of physics-based models is that they have the potential to be applied to eruptions at volcanoes where there is little or no archive data on which to base empirical models. The most widely applied model of this type is the material failure model, which links rates of seismicity and deformation to the timing of eruption onset through theoretical and experimental understanding of rock mechanics, fracturing, and faulting. Additional models related to seismicity, such as earthquake focal mechanisms and the evolution and transfer of stress, also have the potential to be formulated to produce probabilistic eruption forecasts.

Expert Elicitation and Event Trees

Many monitoring datasets are too limited, and the understanding of physical processes is too incomplete, to produce completely objective eruption forecasts. In practice, the gap is bridged by expert opinion, where one or many individuals assess the likelihood of different scenarios given the empirical and physical information available. Expert elicitation can also be used to define thresholds for seismic precursor metrics that indicate likely changes in behavior (e.g., the rate of magnitude 2 and greater VT earthquakes exceeding 10 per day). Formal methodologies, such as the Delphi method, can assimilate opinions from groups of experts. These approaches may include weighting for individuals on the basis of past performance or performance on benchmark questions.

Several strategies have been developed to integrate information based on different precursory phenomena, including event trees (Sobradelo and Martí 2010; Marzocchi et al. 2008; Newhall and Hoblitt 2002) and Bayesian belief networks (Aspinall et al. 2003). Event trees provide a quantitative method to combine different forecasting approaches, including empirical statistics, the outputs of physics-based models, and expert opinion to provide probabilities of future volcanic activity. Event trees follow a hierarchical structure, with a series of increasingly specific levels mapping out all possible outcomes of unrest (Fig. 1). The probabilities at each node may be independent or may be conditional on those of preceding nodes. The probability of any given outcome can then be calculated by combining the probabilities associated with all the nodes along the path. These probabilities can be calculated using Bayesian statistics in a Bayesian framework that

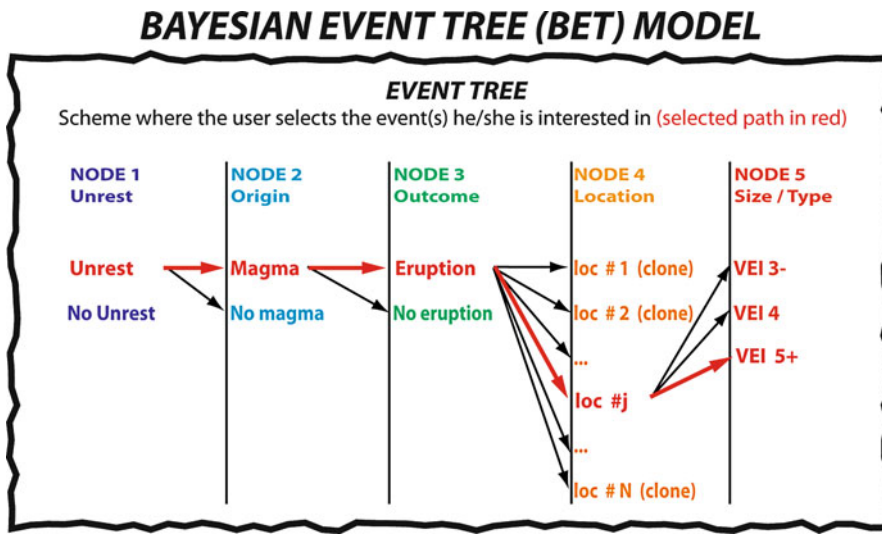

Volcanic Eruptions, Real-Time Forecasting of, Fig. 1 Bayesian event-tree scheme for forecasting volcanic eruptions (Marzocchi et al. 2008). The tree follows a hierarchical structure, with the probability of each path being computed using the conditional probabilities of each node and, in this instance, Bayesian statistics

can account for both epistemic and aleatoric uncertainties. The event-tree approach allows many different sources of information to be combined and uncertainty to be formally quantified. It also provides a structured framework in which to consider the range of potential future activity, different eruptive scenarios, and the evidence required to distinguish between possible outcomes.

Seismic monitoring data are a primary input to event-tree forecasts. A key challenge is how to develop appropriate metrics to describe seismic characteristics and to establish the thresholds, and relative weightings, for different metrics. The record of monitoring data from volcanoes is currently too small and short to do this empirically, and instead, these values are usually be provided by expert opinion.

Material Failure Models

Material failure models are physics-based forecasting methodologies that utilize the rates of preeruptive seismicity and deformation. Increasing rates of local earthquakes have been widely reported before a range of volcanic eruptions and changes in volcanic activity. In some instances, the rate appears to increase systematically with time, leading to the development of models to describe preeruptive changes in earthquake rate and aiming to provide quantitative forecasts of the timing of eruption. In scenarios where baseline monitoring data is unavailable, or where empirical data from analogue volcanoes may not be reliable, physics-based forecasting models have the potential to provide quantitative forecasts of future activity.

The History of Material Failure Models

Several pioneering studies observed increases in rates of earthquakes and their energy release before eruptions and used these parameters to propose simple, empirical methods for forecasting the timing of eruptions. Thus, Omori (1920) and Minakami (1960) used examples from Japanese volcanoes to investigate the forecasting potential of increasing rates of occurrence of local earthquakes, or volcano-tectonic events, whereas Tokarev (1963, 1971) argued that the cumulative Benioff strain (which is proportional to the square root of the seismic energy released) followed a hyperbolic increase with time before selected andesitic eruptions in Russia and Japan.

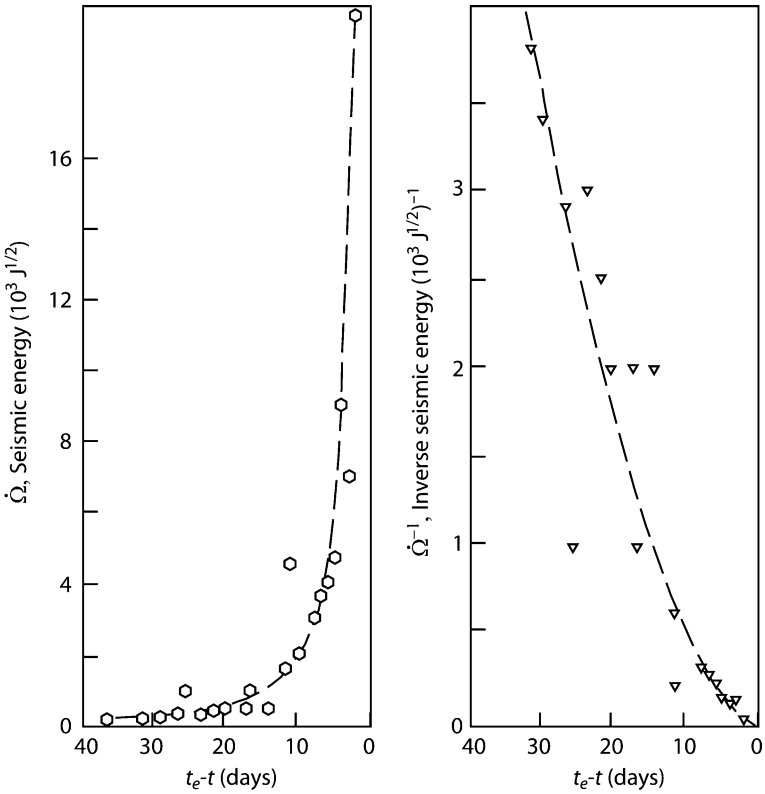

Volcanic Eruptions, Real-Time Forecasting of, Fig. 2 Cumulative seismic strain release rate $\dot{\Omega}$ and inverse rate $\dot{\Omega}^{-1}$ before the 12 April 1960 eruption at Bezymianny (After Voight 1988)

Voight (1988) recognized a similarity in the behavior of field precursors to eruptions and the rates of cracking monitored before the bulk failure of samples undergoing creep in the laboratory. He implicitly inferred that the similarity indicated the control of scale-independent deformation processes before larger-scale failure (from failure of a laboratory sample to breaking of the crust before an eruption) and proposed a "fundamental law for failing materials," for which the acceleration ($\ddot{\Omega}$) and rate of change ($\dot{\Omega}$) of a precursor (Ω) are related by

$$\ddot{\Omega} = A\dot{\Omega}^{\alpha}$$

which describes a self-accelerating trend, such that as the rate increases, the acceleration becomes larger, increasing the rate still further; A is an empirical constant, and α, which usually lies between 1 and 2, describes the strength of the feedback relation that drives self-acceleration (Fig. 2). The limit $\alpha = 1$ corresponds to an exponential increase in rate with time, whereas $\alpha > 1$ describes power-law increases that are faster than exponential and include a hyperbolic increase with time when $\alpha = 2$.

The power-law forms of Voight's relation inherently define a singularity, associated with an infinite rate of occurrence of local earthquakes (and of their release of seismic energy). This singularity corresponds to an inverse-rate approaching zero and is inferred to indicate the formation of a magmatic pathway immediately before eruption. Forecasting the time of eruption therefore equates to extrapolating the precursory trend to the time at which the inverse rate becomes zero (or when the rate tends to an infinite value). In contrast, the exponential form of Voight's relation $\propto = 1$ does not contain a singularity and will yield the theoretical infinite rate only after an infinitely long time. In such cases, the end of the precursory sequence must be defined by an alternative threshold, such as a finite maximum rate or a maximum cumulative value for the precursor (e.g., a maximum rate or a maximum total number of local earthquakes).

Cornelius and Voight (1995) describe methods for preparing forecasts from trends with different values of $\propto$.

When first proposed, the Voight relation was presumed to apply to a range of precursors related to deformation and seismicity. The term Ω has thus been identified with ground deformation, numbers of seismic events, seismic energy release, and the amplitude of seismic signals, notably RSAM or real-time seismic amplitude measurements (Voight and Cornelius 1991). It was also assumed that accelerations in precursors followed a single trend, associated with a single value of α. However, field observations and data from rock-fracture experiments in which the applied stress increases with time (instead of the creep experiments, under constant stress, that were used to develop the original relation) show that seismic-related precursors can accelerate while the bulk deformation rate remains constant. In such cases, the Voight relation may be applicable to the seismic precursors, but not to bulk deformation. They also show that accelerations can evolve with time from exponential to faster-than-exponential trends. The selection of suitable precursors and their behavior with time may thus change according to time-dependent variations in the conditions of loading during the approach to bulk failure (Kilburn 2012).

Theoretical Underpinning of the Voight Relation: Rock Mechanics, Fracture Growth, Damage, and Lava Dome Growth/Failure

The Voight equation describes the type of self-accelerating behavior that is consistent with observations of precursors to eruptions. It also emphasizes the key role played by the rate of change a precursor, rather than the value of the precursor above a background amount. Given the strong connection of precursors to brittle failure, models to explain the Voight relation have focused on fracture or fault growth and linkage through a volcanic edifice and underlying crust. The models have adopted a broadly damage-mechanics approach and related the seismic precursors, in particular, to the behavior of a population of faults within a volume of deforming crust that is much larger than the typical fault length (Kilburn 2003; Lengliné et al. 2008; Main 1999). Accelerating rates of earthquakes can also be interpreted in terms of rate-and-state friction acting on a population of faults (Segall 2013), and in addition, they can emerge under specific regimes within the Epidemic-Type Aftershock Sequence (ETAS) model (Amitrano and Helmstetter 2006).

All the models require the action of a time-dependent process to control rates of self-acceleration. For creep deformation under a constant applied stress, continued fracturing is associated with the weakening of rock around fracture tips. A preferred weakening mechanism is stress-enhanced chemical corrosion, in which fluids in the rock, notably water, chemically attack the silicon–oxygen bonds in the zones of high strain at the tips of fractures. For deformation under increasing stress, time dependence is provided by the bulk stress rate itself. For both loading conditions, the rate of redistribution of stress in the vicinity of growing fractures may appear as another controlling time-dependent process.

Accelerating rates of local seismicity have also been reported before changes in eruptive style at volcanoes that have already established a connection between a magma body and the surface. They are especially evident during the effusion of andesitic–dacitic lava domes, including those from Mount St Helens in the USA and Soufriere Hills on Montserrat, and appear to precede major increases in effusion rate or the sector collapse of domes. Current models suggest that the fracturing in these cases may occur as stresses increase within a feeding conduit or dike and cause cooler magma in contact with the wall rock to ascend by fracture, rather than by flow (Hammer and Neuberg 2009).

Model Application and Statistics

An important aspect of the development of forecasts on the basis of physical models is how to optimize models given observed data. Most physics-based forecasting models (including those underpinned by Voight's relation) take the

form of differential equations. Forecasts rely on estimating equation parameters and their uncertainty given some observed data and, perhaps, some prior belief. Consequently, the reliability of forecasts using this approach relies on the robustness of the methods used to estimate parameter values, as well as on the quality and quantity of the data.

Best-fit values for parameters have conventionally been estimated using least-squares regression. However, the most appropriate method for estimating parameters depends on the nature of the data and whether the data is aggregated into finite size bins. Continuous data (such as strain or tilt measurements) require different error distributions to discrete data (such as number of earthquakes per day). As a result, least-squares regression may not be a suitable method for estimating parameters. More robust estimates may instead be obtained using alternative fitting techniques, such as the generalized linear model and the maximum-likelihood method. Thus, the generalized linear model allows different error distributions to be accounted for on aggregated data and can be formulated for different simple forms of Voight's relation. In contrast, for the occurrence of discrete events (e.g., earthquake occurrence), the best model parameters can be estimated using the maximum-likelihood function (Bell et al. 2013).

Real-Time Forecasting and Testing

Neils Bohr is often quoted as saying that "prediction is difficult, especially about the future." In this context, fitting past data, i.e., with the benefit of hindsight, is always going to be much easier than fitting "future" data or indeed any data not used to formulate a hypothesis. Fitting past data is sometimes called "history matching." It is useful for developing insight into the processes at work and developing appropriate hypotheses to test, but cannot be used to assess predictability. After developing models on one dataset, the next step may be to fit a different set of past data and see if the model still works or to break up a new dataset into two components, use the older data to forecast the younger using the same model, and then test the outcome. This is sometimes called "hind-casting" by the meteorological community. It is a step up from history matching, but it is still plagued by the fact that it is not possible to avoid biases creeping in from knowing the actual outcome, for example, retrospectively selecting a dataset containing events with a disproportional number of eventual eruptions or even in deciding what and when to publish. However hard humans try to be unbiased, it is an established fact that they cannot avoid unconscious biases of data, model, and parameter selection creeping in unconsciously. This is why medical trials are run as "double blind" tests, for which neither doctors nor patients know who is on the drug being tested and who is on the placebo. History matching and hind-casting are necessary, but not sufficient, steps in developing a forecasting model. Such testing may help rule out some models but cannot really be used to prove that a particular one will really work in true forecasting mode. The only way to test this properly is to make and test a forecast in real time, in true prospective mode, in a way that can be verified by the community. Moreover, to test a probabilistic forecast, it is also necessary to make many real-time forecasts and assess the accuracy of the outcomes for a representative statistical sample.

The Importance of Real-Time Testing: Lessons from the Earthquake and Meteorological Communities

Forecasting is used in two ways. In scientific terms, it is the "gold standard" hypothesis test and can be used to test multiple hypotheses in a manner that is as objective and unbiased a manner as possible. In practical terms, forecasting is an operational matter – when do we have enough evidence that activity is sufficient to justify some preparatory action, for example, a heightened alert or the evacuation of a vulnerable district? In the introduction, we distinguished between "forecasting" – a statement of probability – and "prediction," which has connotations with

determinism that is difficult to reconcile with what we know about the complexity, nonlinearity, and our incomplete and uncertain sampling of potential precursors to an eruption. This semantic distinction is old but important. Recently, Ken Mylne of the UK Met Office has written that "u*ncertainty* is an inherent part of weather forecasting – the very word *forecast*, coined by Admiral Fitzroy, who founded the Met Office over 150 years ago, differentiates it from a *prediction* by implication of uncertainty" (our italics). This distinction has been taken up by the seismological community in the wake of the debate on earthquake predictability and was influenced by the failure of the Parkfield, California earthquake prediction experiment. Bakun et al. (2005) concluded "The 2004 Parkfield earthquake, with its lack of obvious precursors, demonstrates that reliable short-term earthquake prediction still is not achievable."

Discussion in the earthquake seismology community has now moved on to the prospective forecasting of space, time, and magnitude-dependent probabilities for earthquake recurrence, informed by the experience in meteorology. To verify forecasting power, the forecasts are lodged in advance with, and made public by, the co-laboratory for the study of earthquake predictability (CSEP) and then tested by the community after a sufficient time has elapsed to distinguish between competing models. Models may be updated, but then they need to be re-tested by the same method. At present, this activity has concentrated on forecasting over a few months or years, where predictability is largely determined by the properties of a mixture of (spatially smoothed) random and triggered seismicity. Several hundreds of years may be needed to gauge the power of longer-term forecasts based on possible nonrandom recurrence, owing to a residual memory of past events and stress renewal. The predictability based on statistical forecasts for a potentially destructive tectonic earthquake is high in relative terms over a time-independent background rate. However, the absolute probabilities remain low at 1 % per day or less (Jordan et al. 2011). Given the much clearer precursory signals prior to volcanic eruptions, we may expect a significantly larger predictability than this, though still well short of 100 %. At the time of writing, no similar globally coordinated forecasting experiment for testing predictability of volcanic eruptions (CSVP) has yet been constituted.

Testing Eruption Forecasting Models

The development of eruption forecasting models has usually involved retrospective application to example datasets. In many cases, these datasets have been specifically chosen to illustrate the potential viability of the model in question. However, a more systematic approach is recommended to establish the forecasting performance of a model, involving three stages of model testing and evaluation. Firstly, models are benchmarked against synthetic data. With modern computational methods, it is relatively simple to produce large numbers of realizations of synthetic earthquake or surface deformation data with some of properties that might be expected for real preeruptive sequences. For example, synthetic precursory data can be generated using the assumptions underlying the failure forecast model. The FFM can then be applied to the data as if they were real, with forecasts compared against the known input parameters. The performance of the model against these data will show a "best-case" outcome that will not be beaten in real applications. Secondly, models are validated against archive data. Datasets from past eruptions at the volcano of interest, or from analogue volcanoes, can be used for "retrospective testing." Models are then applied as if the data were being collected in real-time, forecasts issued, and the results compared against the real observations. These tests can begin to establish true forecast uncertainty, and the extent to which the model is truly consistent with the observed data and trends. Finally, models are tested in real time on volcanic monitoring data and with forecasts issued ahead of eruptions. Such "prospective testing" establishes the true forecasting performance of different models, their relative performance, and their

performance compared to simpler null hypotheses: In this way there is no possibility for unfair selection of data or model parameters.

This approach requires formulating models to run automatically and independently, meaning that the forecasting model must be formalized and otherwise hidden sources of uncertainty are accounted for. For example, it must be determined when it is appropriate to apply any given model to data, what the model inputs and outputs are, and what are the values and uncertainties of any model constants. This approach also brings attention to questions such as: what constitutes a good forecasting performance?; and what are the most appropriate forecast metrics for both testability and utility for different potential end-users?

The Future of Eruption Forecasting

There is much that is still unknown about preeruptive processes, and so plenty of scope for improvement in eruption forecasting models. When does the inclusion of physics improve forecasting performance above simply empirical models? How can we best combine multi-parameter datasets, especially seismicity and deformation data? And can we develop reliable physical models for forecasting the style, size, and location of eruption as well as the timing? Key to answering these questions work is the establishment of consistent and well-integrated multi-parameter monitoring datasets from a wide range of volcanoes. These datasets should include information from apparently quiescent systems to establish baseline behavior; a continuous record from a single seismometer and GPS station at an otherwise unmonitored volcano would potentially provide valuable information when unrest was detected. International databases, data standards, and data sharing agreements, supported by new Informatics and computational facilities, should allow the most to be made of available data.

Forecast testing and evaluation will provide some answers to questions regarding forecast performance and the physical processes controlling volcanic eruptions. However, these developments will also bring further challenges regarding forecast operation and outputs. It will be necessary to develop ensemble forecasting methodologies for integrating the outputs of different models and Bayesian methods for updating forecasts in real time as new data arrives. Ultimately, the aim of eruption forecasting is to help efforts to increase resilience to volcanic hazards. This will require the inclusion of potential end-users at early stages in the model development process to establish the best approach for formulating, communicating, and visualizing forecasts and their uncertainty.

Summary

Eruption forecasts are probabilistic assessments of future eruptive activity, and are important for effective mitigation of volcanic hazards. Changes in patterns of volcanic earthquakes are a key indicator of unrest, and seismic signals are one of the primary datasets used for short-term forecasting of volcanic activity. Forecasting models take information from seismic data and converts it into quantitative estimates of future activity and their uncertainty. These models can be purely empirical, based on statistics of precursory signals before previous events, or physical, based on theoretical concepts of preeruptive processes. A critical step to future improvements of forecasting methods is the development of independent real-time testing of forecasting models (i.e., before the eruption has happened).

Cross-References

- ▶ Earthquake Swarms
- ▶ Frequency-Magnitude Distribution of Seismicity in Volcanic Regions
- ▶ Rockfall Seismicity Accompanying Dome-Building Eruptions
- ▶ Volcano-Tectonic Seismicity of Soufriere Hills Volcano, Montserrat

References

Amitrano D, Helmstetter A (2006) Brittle creep, damage, and time to failure in rocks. J Geophys Res 111:1–17

Aspinall WP, Woo G, Voight B, Baxter PJ (2003) Evidence-based volcanology: application to eruption crises. J Volcanol Geotherm Res 128(1–3):273–285. doi:10.1016/S0377-0273(03)00260-9

Bakun WH, Aagaard B, Dost B, Ellsworth WL, Hardebeck JL, Harris RA et al (2005) Implications for prediction and hazard assessment from the 2004 Parkfield earthquake. Nature 437(7061):969–974. doi:10.1038/nature04067

Bell AF, Naylor M, Main IG (2013) The limits of predictability of volcanic eruptions from accelerating rates of earthquakes. Geophys J Int. doi:10.1093/gji/ggt191

Chouet BA, Matoza RS (2013) A multi-decadal view of seismic methods for detecting precursors of magma movement and eruption. J Volcanol Geotherm Res 252:108–175. doi:10.1016/j.jvolgeores.2012.11.013

Cornelius R, Voight B (1995) Graphical and PC-software analysis of volcano eruption precursors according to the Materials Failure Forecast Method (FFM). J Volcanol Geotherm Res 64(3–4):295–320. doi:10.1016/0377-0273(94)00078-U

Hammer C, Neuberg J (2009) On the dynamical behaviour of low-frequency earthquake swarms prior to a dome collapse of Soufrière Hill volcano, Montserrat. Geophys Res Lett 36:1–3

Jordan T, Chen Y, Gasparini P, Madariaga R, Main I, Marzocchi W et al (2011) Operational earthquake forecasting: state of knowledge and guidelines for implementation. Ann Geophys 1–77. doi:10.4401/ag-5350

Kilburn C (2003) Multiscale fracturing as a key to forecasting volcanic eruptions. J Volcanol Geotherm Res 125(3–4):271–289. doi:10.1016/S0377-0273(03)00117-3

Kilburn C (2012) Precursory deformation and fracture before brittle rock failure and potential application to volcanic unrest. J Geophys Res 117(B2). doi:10.1029/2011JB008703

Lengliné O, Marsan D, Got J, Pinel V, Ferrazzini V, Okubo P (2008) Seismicity and deformation induced by magma accumulation at three basaltic volcanoes. J Geophys Res Solid Earth (1978–2012) 113(B12305). doi:10.1029/2008JB005937

Main I (1999) Applicability of time-to-failure analysis to accelerated strain before earthquakes and volcanic eruptions. Geophys J Int 139(3):F1–F6. doi:10.1046/j.1365-246x.1999.00004.x

Marzocchi W, Bebbington M (2012) Probabilistic eruption forecasting at short and long time scales. Bull Volcanol 74(8):1777–1805. doi:10.1007/s00445-012-0633-x

Marzocchi W, Sandri L, Selva J (2008) BET_EF: a probabilistic tool for long-and short-term eruption forecasting. Bull Volcanol 70(5):623–632

McNutt SR (1999) Volcano seismicity. In: Sigurdsson H (ed) Encylopedia of volcanoes. Academic, San Diego, pp 1015–1033

McNutt SR (2005) Volcanic seismology. Annu Rev Earth Planet Sci 33(1):461–491. doi:10.1146/annurev.earth.33.092203.122459

Mignan A, Woessner J (2012), Estimating the magnitude of completeness for earthquake catalogs. Community Online Resource for Statistical Seismicity Analysis, doi:10.5078/corssa-00180805. Available at http://www.corssa.org

Minakami T (1960) 31. Fundamental research for predicting volcanic eruptions (Part 1): earthquakes and crustal deformations originating from volcanic activities. Bull Earthq Res Inst 38:497–544

Newhall C, Hoblitt R (2002) Constructing event trees for volcanic crises. Bull Volcanol 64(1):3–20. doi:10.1007/s004450100173

Omori F (1920) The Sakura-Jima eruptions and earthquakes. V. Bull Imperial Earthq Investig Committee 8(5):353–466

Roman D, Cashman K (2006) The origin of volcano-tectonic earthquake swarms. Geology 34(6):457. doi:10.1130/G22269.1

Schmid A, Grasso J (2012) Omori law for eruption foreshocks and aftershocks. J Geophys Res Solid Earth 117(B7):1–19. doi:10.1029/2011JB008975

Segall P (2013) Volcano deformation and eruption forecasting. Geological Society, London, Special Publications. doi:10.1144/SP380.4

Sobradelo R Martí J (2010) Bayesian event tree for long-term volcanic hazard assessment: application to Teide – Pico Viejo stratovolcanoes, Tenerife, Canary Islands. J Geophys Res 115. doi:10.1029/2009JB006566

Sparks RS (2003) Forecasting volcanic eruptions. Earth Planet Sci Lett 210(1–2):1–15. doi:10.1016/S0012-821X(03)00124-9

Swanson DA, Casadevall T, Dzurisin D, Malone S, Newhall C, Weaver C (1983) Predicting eruptions at Mount St. Helens, June 1980 through December 1982. Science 221(4618):1369–1376

Tokarev P (1963) On a possibility of forecasting of bezymianny volcano eruptions according to seismic data. Bull Volcanol 26(1):379–386. doi:10.1007/BF02597299

Tokarev P (1971) Forecasting volcanic eruptions from seismic data. Bull Volcanol 35(1):243–250. doi:10.1007/BF02596821

Voight B (1988) A method for prediction of volcanic eruptions. Nature 332(6160):125–130. doi:10.1038/332125a0

Voight B, Cornelius R (1991) Prospects for eruption prediction in near real-time. Nature 350(6320):695–698. doi:10.1038/350695a0

Volcano-Tectonic Seismicity of Soufriere Hills Volcano, Montserrat

Patrick Smith
Montserrat Volcano Observatory, Flemmings, Montserrat
Seismic Research Centre, University of the West Indies, Trinidad and Tobago, West Indies

Synonyms

A-type volcanic earthquakes; HF earthquakes; High-frequency volcanic earthquakes; The eruption of Soufrière Hills Volcano; Volcano-tectonic earthquakes; VT earthquakes; Montserrat

Introduction

Introduction and Definitions

Volcano-tectonic (hereafter VT) earthquakes, sometimes also termed high-frequency (HF) earthquakes, are a category of volcanic seismic signal. They are local earthquakes that occur in a volcanic setting and possess clear impulsive *P*- and *S*-phases with energy between 1 and 20 Hz, an example of which is shown in Fig. 1.

VT earthquakes are interpreted as resulting from brittle failure or shear fracturing along a fault plane and are therefore indistinguishable from ordinary double-couple tectonic earthquakes. Since VT earthquakes possess the same characteristics as tectonic earthquakes, if they are recorded at sufficient stations, standard seismological methods and tools can be used to determine their hypocenters, magnitudes, and focal mechanisms.

The local stress field in volcanic environments is a combination of the regional tectonic stress and that produced by magmatic and hydrothermal processes. The interaction of these two components leads to the generation of VT earthquakes, which are produced by stress changes, linked to the movement of magma or other fluids. Therefore, VT earthquakes are often linked to magmatic intrusion and are generally regarded as one of the earliest precursors to increased volcanic activity or unrest (Roman and Cashman 2006). VT earthquakes rarely follow the typical mainshock-aftershock sequence seen for tectonic earthquakes, but instead often exhibit different patterns of swarm behavior, with events clustering in time and space without a single mainshock (McNutt 2005). An increase or acceleration in the rate of VT seismicity is often associated with volcanic eruptions, and theoretical models and concepts, such as material failure, have been used to explain these trends and even to produce short-term eruption forecasts.

Magnitudes of VT earthquakes are typically small, $0 < m_b < 3$, and are rarely higher than $m_b 4.5$ (Zobin 2012), but their generally shallow depth can produce locally high intensities close to the source. The relationship between earthquake magnitude and frequency of occurrence is described by the Gutenberg-Richter frequency-magnitude relation, generally expressed by the *b*-value, where *b* is the slope of linear relationship between magnitude and number when written as $\log_{10} N = a - bM$. In tectonically active areas the *b*-value is generally close to 1.0, but in volcanic areas swarms of VT earthquakes can have much higher *b*-values, with many smaller events and fewer larger ones.

Examples

VT earthquakes can occur before and during volcanic eruptions in a variety of tectonic settings. In basaltic systems such as Piton de La Fournaise volcano, La Reunion, VT earthquakes have been used to track the migration and propagation of magma in an intruding dyke (Battaglia et al. 2005). This behavior is uncommon, however, especially at more silicic volcanoes, and VT seismicity does not usually reveal the path of magma migrating towards the surface prior to eruption. A common precursory feature appears to be the presence of distinct distal clusters of VT earthquakes away from the main volcanic vent, which often disappear with the onset of magmatic activity.

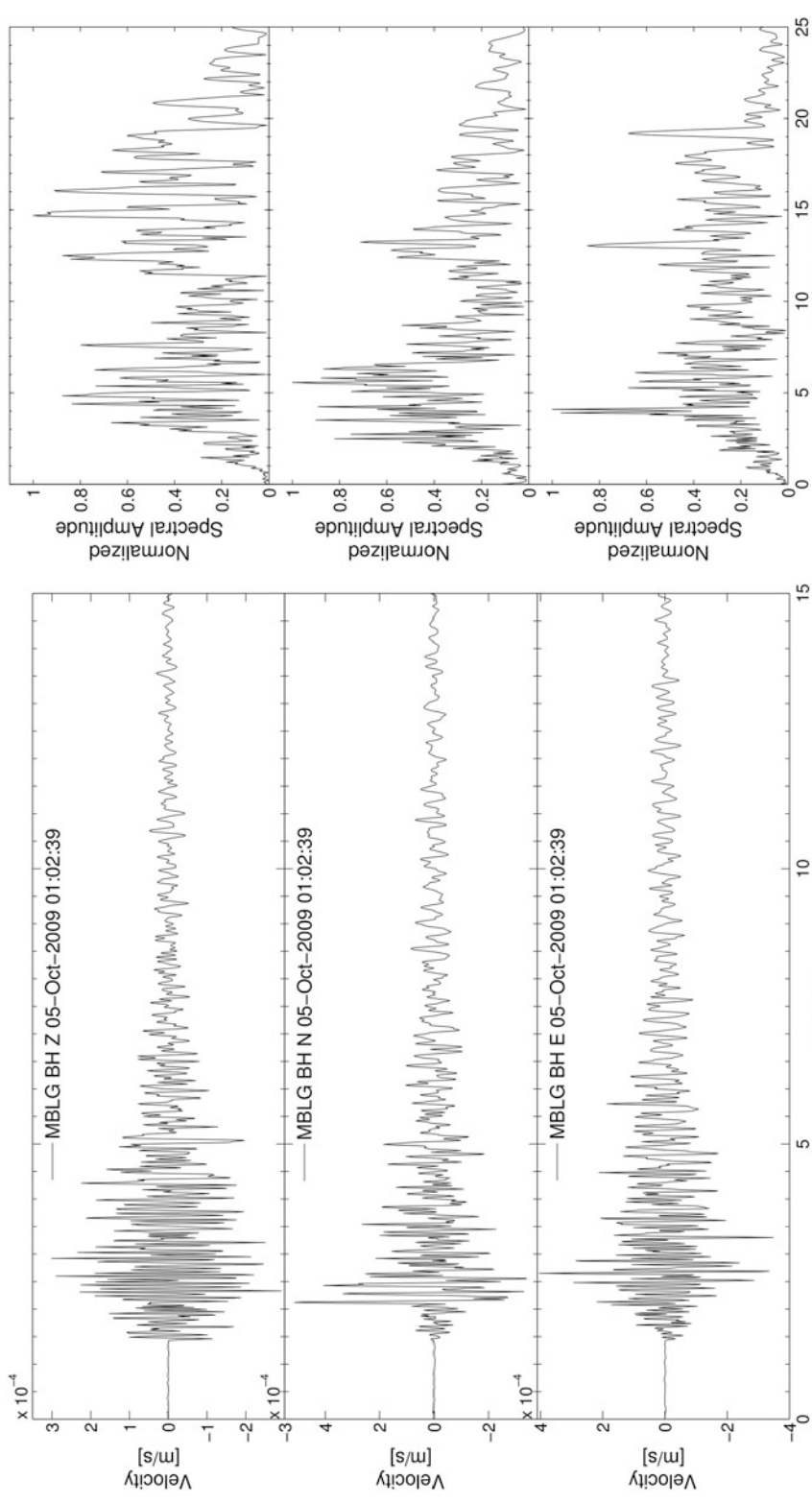

Volcano-Tectonic Seismicity of Soufriere Hills Volcano, Montserrat, Fig. 1 VT earthquake waveform showing *P*- and *S*-phases and broad amplitude spectrum. This example shows 15 s long three-component velocity seismograms from a $M_L 2.8$ VT earthquake recorded at station MBLG, approximately 3 km NE of Soufrière Hills volcano, Montserrat, on 5 October 2009

Several examples of this phenomenon have been seen preceding volcanic eruptions in recent years. Each of the last major eruptions at Augustine volcano, Alaska, was preceded by several months of increased and escalating VT seismicity. In the 8 months preceding the explosive eruption in 2006, a cluster of distal VT earthquakes occurred approximately 25 km northeast of Augustine volcano (Fisher et al. 2010). The 1990 eruption of Unzen volcano in southwest Japan was preceded by several years of VT seismicity distributed mainly more than 4 km to the west of the summit (Umakoshi et al. 2001). Two months of VT seismicity also preceded the 1991 eruption of Mount Pinatubo, Philippines. Again, the seismicity occurred in distinct clusters, at shallow depths below the summit and slightly deeper around 5 km to the northwest, with the rate of seismicity accelerating in the days before 7 June eruption. During the early stages of the eruption of Soufrière Hills volcano, Montserrat, in 1995, two main distal clusters of VT earthquakes several km northeast and northwest of the vent were also observed (Aspinall et al. 1998). These are discussed in more detail in the section "Pre-1995 and Phase 1 VT Seismicity."

Outline

This contribution comprises of a roughly chronological review of VT seismicity at Soufrière Hills volcano (hereafter SHV), Montserrat, chosen because the well-monitored and well-studied ongoing eruption of SHV offers an unparalleled example of the evolution of VT earthquakes during a long-lived multiphase dome-building volcanic eruption.

Section "Soufrière Hills Volcano" provides some background to the current eruption of SHV, before the VT seismicity is discussed in detail in the following sections. Section "Pre-1995 and Phase 1 VT Seismicity" discusses the preeruption and early-eruption seismicity, while the relationship between VT seismicity, stress changes, and magmatic intrusion throughout the eruption is examined in the section "VT Earthquakes and Stress." Some of the more recent VT seismicity at SHV is described in the section "Recent VT Seismicity at SHV," primarily the short spasmodic bursts or swarms of VT seismicity that have been termed VT "strings."

Soufrière Hills Volcano

Geological Background and Eruptive History

Soufrière Hills volcano is an andesitic volcano occupying the southern portion of the island of Montserrat. The 16 × 10 km island is located in the northern part of the 800 km long Lesser Antilles volcanic arc, a result of the subduction of the North American plate beneath the Caribbean plate at a convergence rate of around 2 cm/year.

Montserrat is made up of three main volcanic complexes, Silver Hills (c.2.6-1.2 Ma), Centre Hills (950–550 ka), and South Soufrière Hills-Soufrière Hills (c.170 ka – present) (Fig. 2), which get progressively younger from north to south. SHV is the youngest and only currently active volcanic center and comprises of a core of several andesitic domes, surrounded by pyroclastic aprons and other volcanic sedimentary deposits. South Soufrière Hills is the result of a short-lived period of basaltic to basaltic-andesite volcanism that occurred approximately 120 ka.

The current eruption of SHV has consisted of five phases (Fig. 3) of lava extrusion which have erupted a total of more than 1 km^3 of andesite in the 18 years since 1995. These extrusive dome-building phases have alternated with distinct pauses, during which no lava was extruded but geophysical monitoring data continued to indicate unrest.

Following a period of 3 years of elevated seismic activity (see the section "Pre-1995 and Phase 1 VT Seismicity"), the eruption of SHV began on 18 July 1995, with several months of phreatic activity followed by the first dome growth in November 1995 (Young et al. 1998). The first magmatic explosion occurred in September 1996 and activity escalated through 1996 and mid- to late 1997, culminating in the destructive lateral sector collapse event on 26 December (Boxing Day) 1997 with associated blast and debris avalanche. The only known

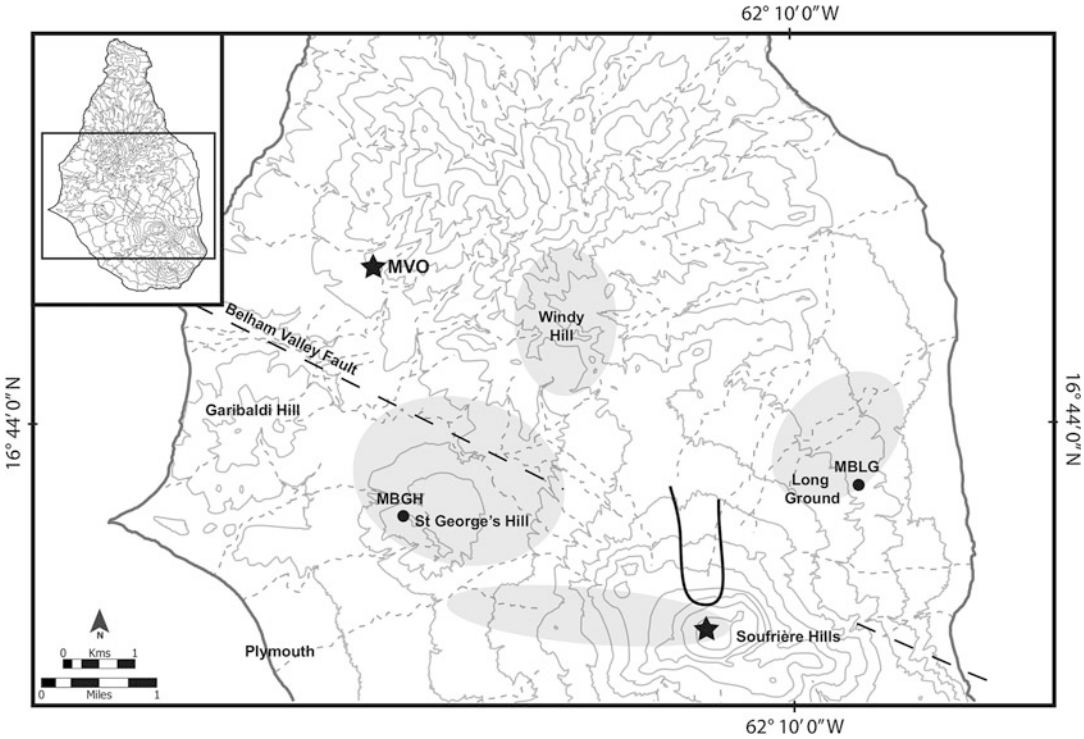

Volcano-Tectonic Seismicity of Soufriere Hills Volcano, Montserrat, Fig. 2 Map of southern Montserrat showing SHV and other key features. The location of MVO along with two seismic stations, MBGH and MBLG, are shown. The *black star* indicates the explosion crater formed during the 11 February 2010 partial dome collapse, close to the dome summit. The topography shown is pre-collapse, with the approximate location of the 11 February 2010 collapse scar shown in *black* to the north of the dome. The regions of the four distal clusters of VT seismicity in 1995 are shown by the *shaded ellipses*: north of St. George's Hill (Aspinall et al. 1998; Gardner and White 2002; Miller et al. 2010), beneath Windy Hill (Gardner and White 2002; Miller et al. 2010), to the NE (Gardner and White 2002), and to the WNW (Miller et al. 2010). The approximate location of the Belham Valley fault (Feuillet et al. 2010) is also marked

fatalities of the eruption occurred during this first phase of extrusion following a significant dome collapse event on 25 June 1997, whose associated pyroclastic flows and surges led to 19 deaths. Since Phase 1, several other whole or partial dome collapses have occurred throughout the eruption, notably in March 2000, July 2003 (the largest recorded collapse of 200×10^6 m^3), and May 2006. The fifth, and most recent, phase of lava extrusion ended on 11 February 2010, with a partial collapse of the lava dome that involved 50×10^6 m^3 of material.

The eruption has caused major social and economic disruption to the island. The former capital Plymouth and much of the island's major infrastructure were destroyed, with the southern two-thirds of the island now a permanent exclusion zone. Many residents were forced to leave the island during the early part of the crisis, although the population has since stabilized. A 2011 census estimated the population at just below 5,000 people, slightly less than half of the preeruption population.

Seismic Crises

Prior to the activity of SHV in July 1995, unpublished evidence from radiocarbon dates of possible volcanic charcoal deposits suggests that the last eruption of SHV occurred during or just before the first European settlement of Montserrat in the early seventeenth century. In later historical times, in the century or so before the onset

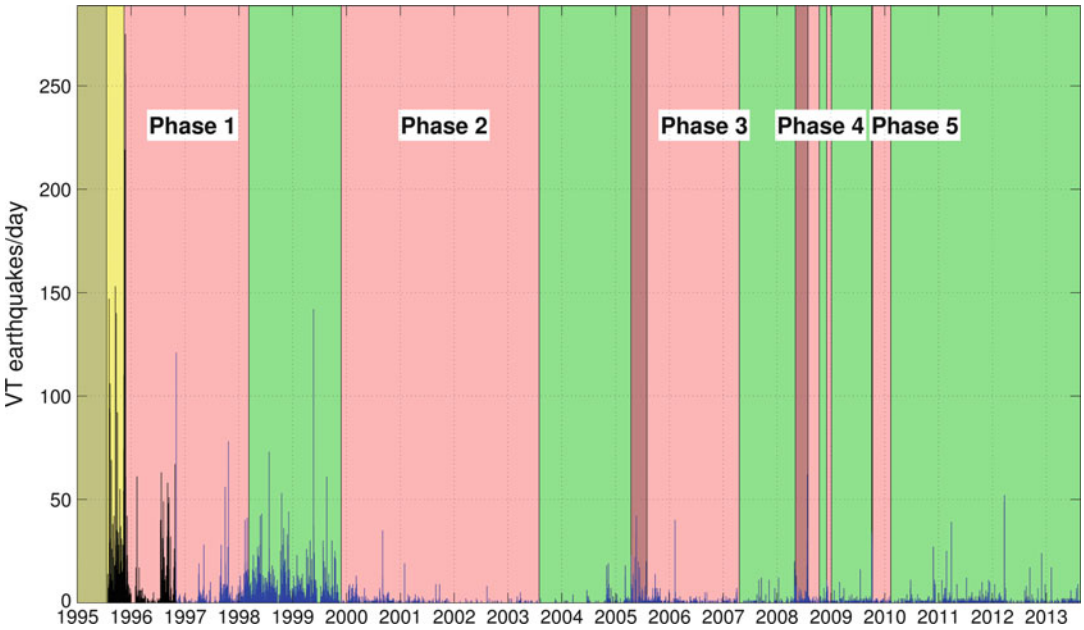

Volcano-Tectonic Seismicity of Soufriere Hills Volcano, Montserrat, Fig. 3 Daily numbers of VT earthquakes recorded at SHV, Montserrat, from 1995 to present. Earthquake counts from the analogue network are shown in *black* and those from the MVO digital broadband network in *blue*. The five extrusive phases are shown in *pink*, with pauses in extrusion in *green*. *Yellow* indicates the initial phreatic phase in 1995, and the *dark-pink* periods are subsequent transitional, precursory, or phreatic phases

of the current eruption, there were several volcanic seismic crises on Montserrat, recurring at approximately 30-year intervals. There is very little record of the first in 1897–1898, but more is known of the second, which occurred between 1933 and 1937. Several thousand felt earthquakes were reported, including a large tectonic (i.e., nonvolcanic) earthquake on 10 November 1935, followed by many aftershocks (Perret 1939). As a result of the Royal Society of London expedition to Montserrat to investigate the activity, Powell (1938) established a seismic network of up to eight stations, which operated until 1951. The locations of around 200 local volcanic earthquakes were reported between May 1937 and May 1938, showing several spatial clusters, notably at shallow depths below Soufrière Hills and St. George's Hill to the northwest (Fig. 2). The seismic crisis in 1966–1967 is also well documented. Following felt earthquake reports in early 1966, four seismic stations were installed by the Seismic Research Unit (SRU), Trinidad, and recorded over 700 local earthquakes between May 1966 and the end of 1967. Hypocenters of VT-type earthquakes were located across the south of the island and beneath Soufrière Hills at depths of less than 15 km (Shepherd et al. 1971).

Increased hydrothermal or fumarolic activity at soufrières surrounding the volcano was observed in association with each of these seismic crises, which have been interpreted as magmatic intrusions that failed to reach the surface.

Pre-1995 and Phase 1 VT Seismicity

VT Seismicity Prior to the 1995 Eruption

After volcanic seismicity on Montserrat waned in late 1967, seismic monitoring on the island was reduced to a single short-period vertical station until 1980, when a real-time telemetered station was installed at St. George's Hill. Between 1967 and 1980 data were recorded locally, and Shepherd et al. (2002) report an average of 3–4 volcanic earthquakes per month, with occasional bursts of

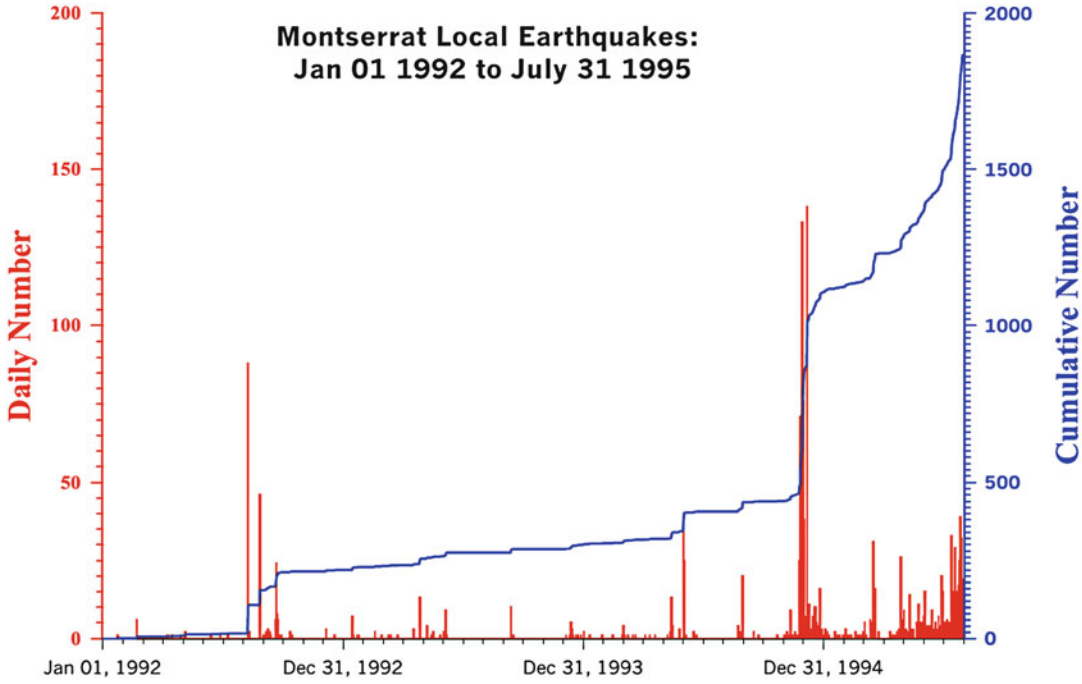

Volcano-Tectonic Seismicity of Soufriere Hills Volcano, Montserrat, Fig. 4 Daily and cumulative numbers of local volcanic earthquakes recorded on Montserrat between 1992 and July 1995 (Taken from Shepherd et al. 2002)

greater numbers. A M6.2 tectonic earthquake occurred on 6 March 1985 approximately 20 km N of Montserrat, near the island of Redonda, followed by a large number of aftershocks in 1985–1986. During this time possible local earthquakes were recorded on Montserrat, and in order to distinguish them from tectonic aftershocks, two new seismic stations were established on Montserrat in 1989 (Shepherd et al. 2002).

Following the pattern of the earlier seismic crises of the twentieth century, seismic activity at SHV increased prior to the 1995 eruption. There is perhaps surprisingly little published literature describing this period, but there is consensus that elevated levels of seismicity on Montserrat were observed from January 1992 (Ambeh and Lynch 1996). However, the earlier seismic network was badly damaged by Hurricane Hugo which impacted the island in 1989, and the network was not restored until 1992 (Shepherd et al. 2002). Therefore, it is difficult to assert with certainty that the period of elevated seismicity began in 1992.

Figure 4 shows the volcanic seismicity on Montserrat from 1992 to the beginning of the eruption in mid-1995, with the average daily rate throughout this period higher than at any time since 1938. Little detail of the waveforms is recorded in the literature, but these events are assumed to be mostly high-frequency VT-type earthquakes, located below southern Montserrat at depths of less than 20 km. A total of 18 steadily increasing episodic swarms, lasting from hours to days, were recorded between January 1992 and 17 July 1995 (Ambeh and Lynch 1996). The sharp increase in mid- to late 1994, including many felt events, prompted the installation of four new seismic stations on the island. The rate began to increase further during 1995, and more than 300 events preceded the first phreatic activity in mid-July. The tenfold increase in the daily rate of seismicity before the first magma extrusion in November 1995 has been attributed to slow-rock fracturing as magma approached the surface (Kilburn and Voight 1998).

Distal VT Swarms

In 1995 seismic monitoring consisted of the short-period (analogue) network, comprising of the existing SRU stations supplemented by a network installed by the USGS Volcano Disaster Assistance Program (VDAP) (Aspinall et al. 1998; Gardner and White 2002). These were mostly 1Hz vertical component instruments, with a total of nine stations, although not all were concurrently active. From October 1996 onwards, a network of telemetered digital seismic stations was installed, eventually superseding the short-period network. This initially comprised of five three-component broadband stations and three short-period vertical stations, but has been incrementally upgraded, evolving into the current MVO seismic network of ten broadband and two short-period stations.

VT earthquakes were the dominant type of volcanic seismicity in both the lead up to the eruption and during the initial phreatic phase (Miller et al. 1998), but were replaced by low-frequency seismicity and rockfalls once dome growth began. They were also more abundant during the early part of the eruption (Fig. 3) and continued in high numbers during the first pause in lava extrusion between 1998 and 2000.

As discussed in the section "Examples," distal clusters of VT earthquakes, away from the main volcanic vent, appear to be a relatively common precursory phenomenon, particularly in silicic systems. This was also the case during the eruption of SHV, Montserrat, in 1995. In terms of hypocentral locations, the vast majority of VT earthquakes at SHV have occurred in a main proximal cluster, occupying a relatively small seismogenic volume beneath the volcanic vent, at depths typically 1–3 km bsl. However, during the early phreatic stages of the eruption in 1995, there is consensus that at least two other short-lived spatial clusters of VT earthquakes occurred (Aspinall et al. 1998; Gardner and White 2002; Roman et al. 2008).

The first cluster occurred approximately 3 km to the northeast of the volcano, over a 2-day period between 5 and 6 August 1995, prior to the onset of lava extrusion. A second distal cluster, 4 km to the northwest of the volcano and centered almost directly beneath St. George's Hill (SGH), occurred between 12 and 14 August 1995, although occasional further events continued until early 1996. Earlier studies (Aspinall et al. 1998; Gardner and White 2002) found depth ranges of 1–6 km, but more recent work suggests a narrower depth range of 3–4 km bsl (Roman et al. 2008). Gardner and White (2002) also identify a third cluster of distal earthquakes, to the north of SHV below Windy Hill, and in more recent analysis Miller et al. (2010) identify a fourth, extending WNW from SHV (Fig. 2).

This spatial pattern of hypocenters, particularly the cluster beneath SGH to the NW, is qualitatively similar to that observed in the earlier seismic crises at SHV (Powell 1938; Shepherd et al. 1971). Recent work (Roman et al. 2008; Miller et al. 2010) has interpreted these distal clusters, particularly the cluster below SGH, as resulting from stress changes produced by an ascending magmatic dyke, with an NE or NNE trend. The explanation of the distal VT seismicity is that the intruding dyke altered the stress distribution in a weakened tectonic zone and oriented ESE across Montserrat, promoting localized fault movements and changes in pore fluid pressure. Geological evidence suggests that SGH is a result of tectonic uplift, rather than a parasitic cone, and the stress transfer hypothesis is preferred to a secondary magmatic intrusion below SGH, where the distal VT earthquakes would have been proximal to the secondary intrusion.

VT Earthquakes and Stress

VT Source Characteristics

Since VT earthquakes are produced by brittle failure or shear fracturing along a fault plane in the same way as tectonic earthquakes, analysis of their source characteristics – their focal mechanisms and moment tensors – can be used to infer information about the local stress conditions.

Full moment tensors describing the inelastic deformation in the source region can be obtained by waveform inversion, but data from VT earthquakes are often too sparse for such methods, so

they are often assumed to be a result of a pure double-couple source mechanism. The geometry of the faulting that occurs during an earthquake can be studied by determining the earthquake focal mechanism (or fault-plane solution), since it is the fault geometry that controls the seismic radiation pattern.

Focal mechanisms are usually determined from the polarity of *P*-wave first motions at various distances and azimuths but can also be further constrained by the amplitude ratio between *P*- and *S*-wave arrivals. Sets of focal mechanisms can be combined together in order to invert for a common stress tensor that completely describes the local stress regime. Alternatively, the orientation of the principal axes of the focal mechanism can be used as a proxy for the orientation of the stress field. These are the so-called pressure (P) and tension (T) axes, which represent the maximum and minimum compressive stress, respectively, and are determined by bisecting the dilatational and compressional quadrants.

Studies at several volcanoes have shown that the orientation of the axes of VT fault-plane solutions can undergo systematic changes in response to volcanic activity (e.g., Umakoshi et al. 2001; Roman et al. 2006) and, in particular, in association with changes in the pressurization of magmatic intrusions.

Regional Stress Conditions on Montserrat

Roman et al. (2008) cite evidence from the fault-plane solutions of nearby regional earthquakes and the orientation of dykes mapped on neighboring islands to suggest that the regional stress field around Montserrat is characterized by maximum compressive stress in an arc-normal, approximately NE-SW direction. Recent studies of the local tectonics, arising from offshore seismic reflection profiles, have suggested that, at a local level, the stress regime may in fact be more complex (Kenedi et al. 2010).

Montserrat is located in the northern part of the Lesser Antilles and is a result of oblique subduction of the North American plate beneath the Caribbean plate, which is accommodated by a combination of large-scale sinistral strike-slip faulting and smaller local normal faults perpendicular to the arc. The dominant structural feature on the island is the extensional Montserrat-Havers fault system (MHFS) (Feuillet et al. 2010), along which the andesitic domes of the SHV complex and other uplifted features such as SGH and Garibaldi Hill are aligned. The MHFS includes an ESE-trending lineament that passes south of the Centre Hills and is interpreted as the Belham Valley fault (BVF). The MHFS also extends to the southeast towards Guadeloupe, where Montserrat lies at the northern end of the offshore Bouillante-Montserrat graben structure (BMF). This could imply a roughly E-W orientation of minimum compressive stress, approximately normal to the N-S regional extensional trend of the MHFS and BMF structures.

VTs and Stress at SHV

The source mechanisms of VT earthquakes at SHV have been analyzed in several studies in order to improve understanding of the local stress field and the nature and orientation of the magmatic intrusions supplying the eruption.

Roman et al. (2006) analyzed the focal mechanisms from a subset of 551 VT earthquakes at SHV with well-constrained double-couple fault-plane solutions, spanning October 1996 to July 2005, and observed temporal changes in the orientation of the *p*-axes. Several periods of a few months were identified where the dominant orientation of the *p*-axes switched from the predominant NE-SW to a NW-SE trend. This represents a 90° rotation from the assumed arc-normal regional maximum compressive stress. Analysis of seismic anisotropy through study of shear-wave splitting of regional earthquakes recorded on the MVO network has provided further evidence to support the presence of short-term variations in the local stress field at SHV.

Models of the interaction between regional and magma-induced stresses (Vargas-Bracamontes and Neuberg 2012) have shown that VT earthquakes on regionally aligned faults are more easily triggered by lower internal pressures of the intruding magma body. By contrast, pressures much higher than the regional stress field are needed to promote rotated VT

earthquakes, supporting observations of their short-lived episodic nature. The presence of such rotated events could therefore indicate significant pressurization of the volcanic system, and hence, the occurrence of these rotated VT events has been interpreted as evidence of stresses induced by the inflation of a NE-SW-oriented dyke beneath SHV. This is broadly supported by the analysis of distal VT focal mechanisms during the early phase of the eruption (see the section "Distal VT Swarms").

This NE to NNE orientation is somewhat in disagreement with the NW- to NNW-oriented dyke proposed for SHV derived from geodetic or borehole strain data. Kenedi et al. (2010) propose an approximately N-S-oriented feeder dyke as a possible way to reconcile these competing models.

Recent VT Seismicity at SHV

Patterns of VT Occurrence at SHV

VT earthquakes were most numerous at SHV in the buildup to the eruption and during the initial phreatic phase before dome growth began. They also continued in relatively high numbers during the first pause in extrusion, occurring at a rate of around 5 per day between March 1998 and November 1999. Since this period the daily rate has been much lower and has remained roughly constant at an average rate of less than one per day from 2000 to present.

However, short-term increases in VT activity have been associated with the restarts in extrusion during the course of the eruption at SHV, often increasing notably during the short transitional or phreatic phases which preceded renewed lava extrusion. Diffuse episodes of VT earthquakes associated with ash venting and minor explosive activity preceded the onset of extrusion of both Phase 3 in mid-2005 and Phase 4 in mid-2008. A more intense swarm of 24 VT earthquakes on 5 October 2009 heralded the onset of several days of ash venting before the start of Phase 5 extrusion.

Since around the end of Phase 3 in 2007, the character of VT seismicity seen at SHV appears to have changed. Fewer intense swarms have been observed, and instead the dominant feature has been the sporadic occurrence of short bursts of high-frequency VT events termed VT "strings." A sequence of repeating VT earthquakes with similar waveforms was also observed in late 2008 and early 2009. The timing of this change in behavior roughly coincides with a departure from the longer extrusive periods of Phases 1–3 to the shorter more rapid extrusion of Phases 4 and 5.

Repeating VTs

An unusual quasiperiodic sequence of seven large ($2.6 < M_L < 3.2$) repeating VT earthquakes was observed at SHV between October 2008 and May 2009, straddling the two brief periods of extrusion that comprised Phase 4. Analysis of arrival times, waveforms, and focal mechanisms suggests a common location and source process for six of the seven events, with inter-event cross-correlation coefficients of 0.75 and above. A composite focal mechanism revealed mostly strike-slip-style faulting, with a *p*-axis orientation of approximately 75°, which does not correspond to either the regional stress aligned or the 90° rotated solutions of Roman et al. (2006).

VT Strings

Description and Characteristics

VT strings, defined as a short, intense swarms of VT earthquakes, a phenomenon occasionally referred to elsewhere as "spasmodic bursts" (e.g., Hill et al. 2002), have become a feature of the eruption of SHV since late 2007. To date, 52 such earthquake sequences have been identified in the 69 months since the first in November 2007, continuing across Phases 4 and 5 of lava extrusion (Fig. 5).

The details of individual strings have varied, but certain common characteristics have been identified. The duration of these sequences has typically been less than an hour, with a mean of roughly 10 events occurring in 30 min, when averaged across all strings. The first event in the swarm is generally not the largest, and thus, VT

Volcano-Tectonic Seismicity of Soufriere Hills Volcano, Montserrat, Fig. 5 Duration of all VT strings recorded at SHV, first seen in November 2007. The white circles represent VT strings that were associated with observable activity at the surface. Extrusive phases are shown in *pink* and pauses in extrusion in *green*, and *dark-pink* periods represent the transitional, precursory, or phreatic phases

strings do not represent a mainshock-aftershock sequence, instead exhibiting swarm-like behavior, with events tightly clustered in time and space (see, e.g., Fig. 7). In terms of their waveforms, hypocenters, and focal mechanisms, analysis of individual earthquakes has revealed no clear differences between those occurring as part of strings and ordinary or background VT events.

Approximately a quarter of VT strings have been linked to observed surficial activity such as ash venting or visibly increasing degassing and fumarolic activity. This has led to some speculation as to their predictive capability in forecasting such activity or perhaps even renewed lava extrusion. This relationship is supported by SO_2 flux data from SHV, which show some degree of correlation with the seismicity, with often, though not in all cases, a spike in gas output several hours to days after the earthquakes occur (Fig. 6). This has led to tentative proposals that the seismicity is perhaps driven by gas release and/or hydrothermal processes, although it is clear that this phenomenon is not well understood and that more work is needed to refine the generation mechanism. Similar models have been suggested elsewhere, such as Nishi et al. (1996), who propose a hydrothermal source for spasmodic bursts observed at White Island, New Zealand, based on a mechanism of brittle failure induced by rapid fluid pressure fluctuations in the shallow hydrothermal system.

March 2012

Some of the most significant VT seismicity at SHV occurred on 22 and 23 March 2012, with two swarms of around 50 VT earthquakes each. The second swarm on 23 March was more energetic than the first, with local magnitudes of up to M_L3.9: some of the largest VT earthquakes to have been recorded at SHV. The most intense phase of the VT swarm lasted only 15 min (Fig. 7) and was followed by three large hybrid earthquakes. A very-long-period (VLP) seismic signal (below 0.1Hz or 10s period) was also

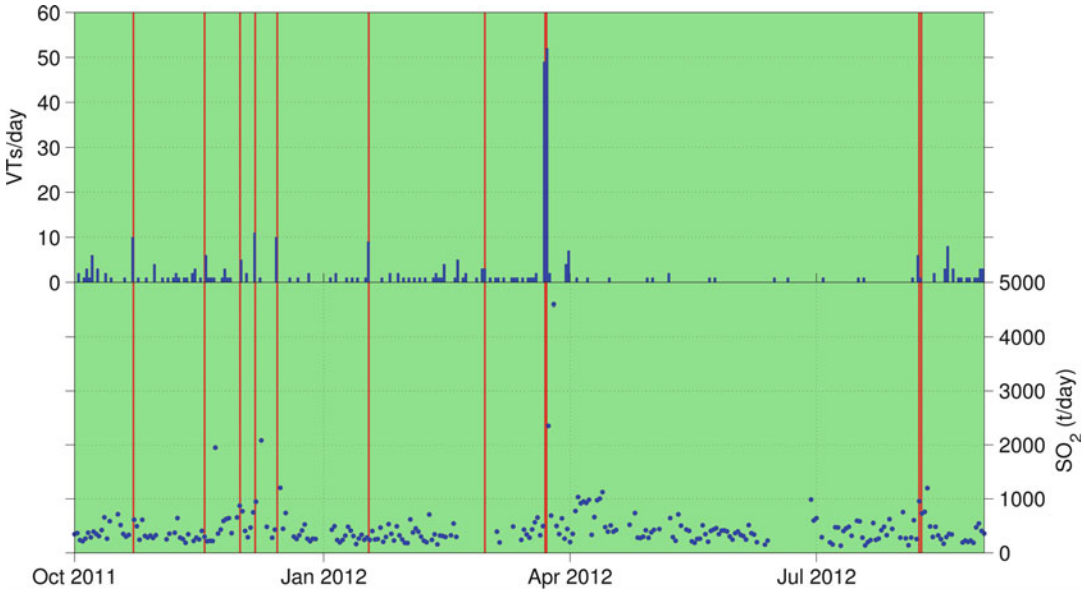

Volcano-Tectonic Seismicity of Soufriere Hills Volcano, Montserrat, Fig. 6 Correlation between VT strings and SO_2 output at SHV for the period October 2011 to September 2012. The top panel shows daily VT earthquake counts and the bottom the recorded SO_2 flux in tonnes per day. VT strings are indicated by the *red vertical lines*

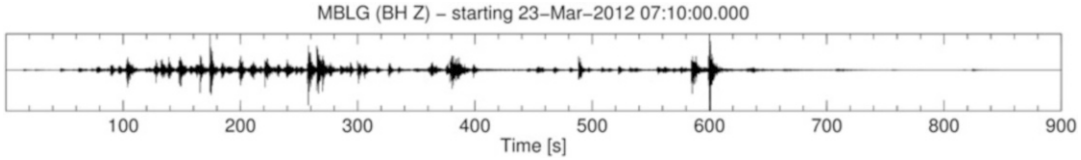

Volcano-Tectonic Seismicity of Soufriere Hills Volcano, Montserrat, Fig. 7 Normalized waveform showing the most intense phase of the VT swarm that occurred at SHV on 23 March 2012. Shown is a 15-min-long vertical component velocity seismogram recorded at station MBLG. The start time is given in UTC

observed across the MVO seismic network during this swarm, coincident with a large amplitude (≈250 nanostrain) strain signal recorded by several borehole strainmeters. The seismicity was followed by mild ash venting several hours later.

As with the explosion and accompanying strain signal on 3 March 2004 (Linde et al. 2010), preliminary analysis of the strain data has suggested the involvement of a shallow dyke or fracture, although in this case there was no emission of magmatic material. The events of 22–23 March 2012 have some broad similarities with the VT strings that have occurred since at SHV since 2007, perhaps hinting at a common driving process. These include the relatively short duration of the VT seismicity and its correlation with ash venting and increased degassing. There was a time lag between the occurrence of the seismicity and the SO_2 output which responded on 24 March (2,400 T) followed by the third highest value ever measured by the spectrometer network of 4,600 T on 26 March. The strong pulse in gas associated with this event is similar to the increase in emissions associated with several other VT strings. However, similar strain signals have not been identified with any other VT strings, although the magnitude of this event was clearly much larger.

Summary

Volcano-tectonic earthquakes are brittle failure events that occur in volcanic environments, sharing many of the properties of tectonic earthquakes. Understanding their characteristics and behavior is of critical importance in monitoring and forecasting efforts, particularly as volcano-tectonic earthquakes are often one of the first signs of volcanic unrest and potential future eruptions. The ongoing eruption of Soufrière Hills volcano, Montserrat, has offered an unparalleled opportunity to observe the evolution of volcano-tectonic seismicity throughout a long-term dome-building eruption.

Several volcano-seismic crises, of presumably mostly VT events, occurred on Montserrat at approximately 30-year intervals throughout the twentieth century, in 1933–1937 and 1966–1967. Volcano-tectonic seismicity was also the most prevalent precursor to the start of the current eruption, with increasing numbers seen in escalating episodic swarms in the 3 years preceding the onset of phreatic activity in 1995. During these initial phreatic stages of the eruption, distal swarms of VT earthquakes several kilometers away from the main summit vent were observed, particularly below St. George's Hill to the northwest of the volcano. This distal cluster is proposed to have resulted from stress transfer through a weakened tectonic zone, rather than a secondary magmatic intrusion. A rapid acceleration in the rate of VT earthquakes, linked to subcritical rock fracturing, also preceded the first magmatic activity and the onset of lava extrusion.

The source mechanisms of VT events can be used to infer the local stress conditions under which they are generated. Analysis of the orientation of the *p*-axes of focal mechanisms of VT earthquakes at SHV has shown systematic temporal changes in response to volcanically induced stresses, in particular the occurrence of events with a 90° rotation from the dominant trend. The presence of these "rotated" events has been interpreted as the result of pressure changes in an NNE- to NE-oriented shallow dyke beneath SHV overprinting the regional stress regime and promoting failure on optimally aligned faults.

A different character of VT seismicity was seen at SHV after the end of the third phase of lava extrusion. VT earthquakes were the dominant seismicity during the short transitional phases that preceded restarts in lava extrusion which were associated with minor explosive activity and ash-venting episodes. The emergence of short spasmodic bursts of VT earthquakes termed VT "strings" since 2007 has also been linked to ash venting, increased fumarolic activity, and SO_2 output. An intense VT swarm on 23 March 2012 occurred coincident with a very-long-period (VLP) seismic signal and a large step in strain. This seismicity preceded mild ash venting and a large spike in SO_2 release, suggesting the processes driving this event and VT strings may be similar.

Cross-References

- ▶ Earthquake Location
- ▶ Earthquake Magnitude Estimation
- ▶ Earthquake Mechanisms and Stress Field
- ▶ Frequency-Magnitude Distribution of Seismicity in Volcanic Regions
- ▶ Seismic Anisotropy in Volcanic Regions
- ▶ Seismic Monitoring of Volcanoes
- ▶ Volcanic Eruptions, Real-time Forecasting of

References

Ambeh W, Lynch L (1996) Seismicity preceding the current eruption of the Soufrière Hills volcano, Montserrat, West Indies. In: Ahmad R (ed) Science, hazards and hazard management – the second Caribbean conference on natural hazards and disasters, vol 1. Unit for Disaster Studies, The University of the West Indies, Kingston, p 30

Aspinall W, Miller A, Lynch L, Latchman J, Stewart R, White R, Power J (1998) Soufrière Hills eruption, Montserrat, 1995–1997: volcanic earthquake locations and fault plane solutions. Geophys Res Lett 25:3397–3400

Battaglia J, Ferrazzini V, Staudacher T, Aki K, Chemin J-L (2005) Pre- eruptive migration of earthquakes at the Piton de la Fournaise volcano (Réunion Island). Geophys J Int 161(2):549–558

Feuillet N, Leclerc F, Tapponnier P, Beauducel F, Boudon G, Le Friant A, Deplus C, Lebrun J-F, Nercessian A, Saurel J-M, Clment V (2010) Active faulting induced by slip partitioning in Montserrat and link with volcanic activity: new insights from the 2009 GWADASEIS marine cruise data. Geophys Res Lett 37(19), L00E15, doi:10.1029/2010GL042556

Fisher MA, Ruppert NA, White RA, Sliter RW, Wong FL (2010) Distal volcano-tectonic seismicity near Augustine Volcano. In: Power J, Coombs M, Freymueller J (eds) The 2006 eruption of Augustine Volcano, Alaska. U.S. Geological Survey, Reston, Virginia, professional paper 1769. pp 119–126

Gardner CA, White RA (2002) Seismicity, gas emission and deformation from 18 July to 25 September 1995 during the initial phreatic phase of the eruption of Soufrière Hills Volcano, Montserrat. In: Druitt TH, Kokelaar BP (eds) The eruption of Soufrière Hills Volcano, Montserrat from 1995 to 1999, vol 21. Geological Society Memoirs, London, pp 567–581

Hill DP, Dawson P, Johnston MJS, Pitt AM, Biasi G, Smith K (2002) Very-long-period volcanic earthquakes beneath Mammoth Mountain, California. Geophys Res Lett 29(10):8-1–8-4

Kenedi CL, Sparks RSJ, Malin P, Voight B, Dean S, Minshull T, Paulatto M, Peirce C, Shalev E (2010) Contrasts in morphology and deformation offshore Montserrat: New insights from the SEA-CALIPSO marine cruise data. Geophys Res Lett 37(19), L00E25, doi:10.1029/2010GL043925

Kilburn CRJ, Voight B (1998) Slow rock fracture as eruption precursor at Soufrière Hills volcano, Montserrat. Geophys Res Lett 25(19):3665–3668

Linde AT, Sacks S, Hidayat D, Voight B, Clarke A, Elsworth D, Mattioli G, Malin P, Shalev E, Sparks S, Widiwijayanti C (2010) Vulcanian explosion at Soufrière Hills Volcano, Montserrat on March 2004 as revealed by strain data. Geophys Res Lett 37(19), L00E07, doi:10.1029/2009GL041988

McNutt SR (2005) Volcanic seismology. Ann Rev Earth Planet Sci 33(1):461–491

Miller A, Stewart R, White R, Luckett R, Baptie B, Aspinall W, Latchman J, Lynch L, Voight B (1998) Seismicity associated with dome growth and collapse at the Soufrière Hills Volcano, Montserrat. Geophys Res Lett 25:3401–3404

Miller V, Voight B, Ammon CJ, Shalev E, Thompson G (2010) Seismic expression of magma-induced crustal strains and localized fluid pressures during initial eruptive stages, Soufrière Hills Volcano, Montserrat. Geophys Res Lett 37(19)

Nishi Y, Sherburn S, Scott BJ, Sugihara M (1996) High-frequency earthquakes at White Island volcano, New Zealand: insights into the shallow structure of a volcano-hydrothermal system. J Volcanol Geotherm Res 72(34):183–197

Perret FA (1939) The volcano-seismic crisis at Montserrat, 1933–1937. Carnegie Institution of Washington, Washington, DC

Powell CF (1938) The Royal Society expedition to Montserrat, BWI. Final report. Philos Trans R Soc A 237:1–34

Roman DC, Cashman KV (2006) The origin of volcano-tectonic earthquake swarms. Geology 34(6):457–460

Roman D, Neuberg J, Luckett R (2006) Assessing the likelihood of volcanic eruption through analysis of volcanotectonic earthquake fault-plane solutions. Earth Planet Sci Lett 248:244–252

Roman D, De Angelis S, Latchman J, White R (2008) Patterns of volcanotectonic seismicity and stress during the ongoing eruption of the Soufrière Hills Volcano Montserrat (1995–2007). J Volcanol Geotherm Res 173:230–244

Shepherd JB, Tomblin JF, Woo DA (1971) Volcano-seismic crisis in Montserrat, West Indies, 1966–67. Bull Volcanol 35:143–163

Shepherd JB, Robertson R, Latchman J, Lynch L (2002) Precursory activity to the 1995 eruption of the Soufrière Hills Volcano, Montserrat, Technical report. Seismic Research Unit, University of the West Indies

Umakoshi K, Shimizu H, Matsuwo N (2001) Volcano-tectonic seismicity at Unzen Volcano, Japan, 1985–1999. J Volcanol Geotherm Res 112(1–4): 117–131

Vargas-Bracamontes D, Neuberg J (2012) Interaction between regional and magma-induced stresses and their impact on volcano-tectonic seismicity. J Volcanol Geotherm Res 243–244:91–96

Young SR, Sparks RSJ, Aspinall W, Lynch L, Miller A, Robertson T, Shepherd J (1998) Overview of the eruption of Soufrière Hills Volcano, Montserrat, 18 July 1995 to December 1997. Geophys Res Lett 25:3389–3392

Zobin VM (2012) Introduction to volcanic seismology. Elsevier, London